Coherent Structures in Land-Atmosphere Interaction

by

Jing Huang

Department of Civil and Environmental Engineering
Duke University

Date:_____

Approved:

_____
John D. Albertson, Supervisor

_____
Amilcare Porporato

_____
Gabriel G. Katul

_____
John E. Dolbow

_____
Jonathan C. Mattingly

Dissertation submitted in partial fulfillment of
the requirements for the degree of Doctor of Philosophy in the Department of
Civil and Environmental Engineering in the Graduate School
of Duke University

2010

ABSTRACT

Coherent Structures in Land-Atmosphere Interaction

by

Jing Huang

Department of Civil and Environmental Engineering
Duke University

Date:_____

Approved:

_____
John D. Albertson, Supervisor

_____
Amilcare Porporato

_____
Gabriel G. Katul

_____
John E. Dolbow

_____
Jonathan C. Mattingly

An abstract of a dissertation submitted in partial
fulfillment of the requirements for the degree
of Doctor of Philosophy in the Department of
Civil and Environmental Engineering in the Graduate School
of Duke University

2010

Abstract

Large-scale coherent structures are systematically investigated in terms of their geometric attributes, importance toward describing turbulent exchange of energy, momentum and mass as well as their relationship to landscape features in the context of land-atmosphere interaction. In the first chapter, we present the motivation of this work as well as a background review of large-scale coherent structures in land-atmosphere interaction. In the second chapter, the methodology of large-eddy simulation (LES) and the proper orthogonal decomposition (POD) is introduced. LES was used to serve as a virtual laboratory to simulate typical scenarios in land-atmosphere interaction and the POD was used as the major technique to educe the coherent structures from turbulent flows in land-atmosphere interaction. In the third chapter, we justify the use of the LES to simulate the realistic coherent structures in the atmospheric boundary layer (ABL) by comparing results obtained from LES of the ABL and direct numerical simulation (DNS) of channel flow. In the fourth chapter, we investigate the effects of a wide range of vegetation density on the coherent structures within the air space within and just above the canopy (the so-called canopy sublayer, CSL). The fifth chapter presents an analysis of the coherent structures across a periodic forest-clearing-forest transition in the steamwise direction. The sixth chapter focuses on the role of coherent structures in explaining scalar dissimilarity in the CSL. The seventh chapter summarizes this dissertation and provides suggestions for future study.

Contents

List of Tables

List of Figures

Acknowledgements

I cannot praise enough my advisor Professor John Albertson, who has contributed immeasurably both to this dissertation and to my overall happiness at Duke in the last five years. I also thank Dr. Massimo Cassiani and Professor Gabriel Katul for their aid and many helpful comments, and Professor Amilcare Porporato, Professor Jonathan Mattingly and Professor John Dolbow for serving on my Ph.D. committee. The many other friends and colleagues who have helped me out are too numerous to mention, but I should especially thank Giulia Vico, Stefano Manzoni, JR Rigby, David Kahler, Michael Rizk, Jenny Law, Scott Hawkins, Billyde Brown, Candong Cheng and Jong-Shin Liau.

This dissertation is dedicated to my wife Mingzhu Cai for her constant love and my parents Zhongcheng Huang and Hanxiu Zhu for their consistently teaching me to be a good man.

1 Introduction

1.1 *Motivation*

Understanding turbulent dynamics in the lower atmosphere is of intrinsic importance to predictions of energy, momentum, heat and mass (e.g., water vapor, CO_2) transport between the land and the atmosphere. It has been demonstrated that large-scale turbulent coherent structures are responsible for the majority of the transport generally in the atmospheric boundary layer (ABL) (e.g., Etling and Brown 1993; Sadani and Kulkarni 2001; Katul et al. 2006a) and particularly in the canopy sublayer (CSL) (e.g., Bergstrom and Hogstrom 1989; Katul et al. 1997b; Thomas and Foken 2007). Turbulent transport models tied more directly to these organized motions, such as Lagrangian stochastic (LS) models (e.g., Raupach 1989a, b; Katul et al. 1997c; Cassiani et al. 2005; Cassiani et al. 2007) and higher-order closure (HOC) models (e.g., Lappen and Randall 2001a, b, c, 2005), which utilize the information of the probability density function (PDF) and the characteristic time scales of coherent structures, have been shown to improve the ability of predicting turbulent dispersion. However, it requires focused study of the three-dimensional features of the coherent structures to reach the level of understanding required for further improvement of the modeling ability (e.g., Moin and Moser 1989; Robinson 1991; Finnigan and Shaw 2000).

Given this necessity, the broad goal of this work is to systematically investigate the coherent structures arising from land-atmosphere interaction with a strong focus on:

(1) the geometrical characteristics of these structures; (2) the internal processes of the formation and evolution of the coherent structures; (3) their role in transporting the turbulent kinetic energy (TKE), momentum and scalar fluxes; and, (4) how the above three aspects change as a function of landscape features. Toward this end, we seek to first numerically simulate turbulent flows in land-atmosphere interaction. Then, the coherent structures will be quantitatively educed in three-dimensional space using proper detection techniques.

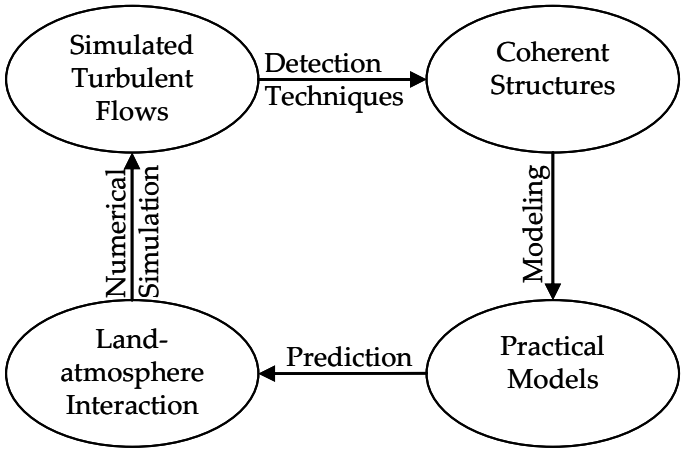

Figure 1.1. Schematic diagram illustrating the relationships among the land-atmosphere interaction, numerical simulations, coherent structures and practical models

The overall picture can be approximately illustrated by the conceptual chain diagram in Figure 1.1, which demonstrates the manifold interactions among (1) land-atmosphere interaction; (2) numerical simulations of turbulent flows; (3) coherent structures; (4) practical models which can assist the prediction and control of turbulent dynamics in the regime of land-atmosphere interaction. This work mainly focuses on

the phase of extracting the coherent structures from databases of turbulent fields generated through numerical simulations although preliminary efforts have been made to develop practical models through the approach of the coherent structures.

1.2 *Historical Perspective*

Originally, the term 'coherent structure' was used in a phenomenological sense, to refer to large and organized eddies in turbulent flows (see e.g., Holmes et al. 1996). The general recognition of the coherent structures in the turbulent boundary-layer can be traced back to the work of Corrsin (1943) and Townsend (1956) (see review by Robinson 1991). In the study of land-atmosphere interaction, this topic has received intense attention in the recent several decades, particularly in the ABL and the CSL. The ABL (or planetary boundary layer, PBL) covers the lowest 1 to 2 km of the atmosphere, the region most directly influenced by the exchange of energy and mass at the earth's surface. The CSL is normally referred to as the region within and just above plant canopies, which vertically ranges from the ground up to approximately twice of the canopy height. These two flow regimes represent typical scenarios in land-atmosphere interaction.

1.2.1 Coherent Structures in the ABL

Large-scale coherent structures, such as longitudinal roll vortices, have been frequently observed in both convective and near-neutral ABL for decades (e.g., Brown 1980; Walter and Overland 1984; Etling and Brown 1993). These structures are often

visualized by so-called cloud streets from high resolution satellite pictures. This type of cloud pattern can be interpreted by the conceptual model of counter-rotating vortex rolls with axes oriented in the downwind direction: cloud bands are formed above the updraft parts of the vortex rolls while cloud free areas are produced by downward motions. It was concluded that these roll vortices contribute considerable vertical transport of momentum, heat and mass between the land and the atmosphere (Etling and Brown 1993). In fact, similar vortical structures, termed 'hairpin' or 'horseshoe' vortices, have been observed through flow visualization techniques in engineering flows (e.g., Bakewell and Lumley 1967; Head and Bandyopadhyay 1981). Moin and Moser (1989) studied the features of the roller structures by performing POD analysis on a direct numerical simulation (DNS) database of a channel flow with Re = 3200, and concluded that the vortices curve up in the streamwise direction. The life cycle of a hairpin vortex is generally described as (Davidson 2004): first, the mean flow interacts with the roughness elements to create a cross-stream (span-wise) vortex; then, the cross-stream vortex is stretched and intensified by some streamwise gust, leading to the shape of a hairpin; finally, the hairpin is destructed through interaction with other vortices. Interestingly, the hairpins rarely appear as symmetric structures, but rather one leg is typically more pronounced than the other (Davidson 2004).

In addition to the longitudinal vortical structures, the sweep-ejection cycle has been investigated as the major contributor to momentum transport, which has been

defined through quadrant analysis (see e.g., Wallace et al. 1972; Willmart and Lu 1972; Antonia 1981). Sweeps generally correspond to fast and downward fluids (i.e. $u' > 0$; $w' > 0$) while ejections are referred to as slow and upward fluids (i.e. $u' < 0$; $w' < 0$) (u' and w' represent turbulent velocities in the streamwise and vertical directions, respectively, see Chapter 2.2). The interest in the sweep and ejection motions can be traced back to the work of Kline et al. (1967), who demonstrated the presence of surprisingly organized motions in the region near the wall. It was shown in an experimental study of channel flow at $Re = 7150$ that in the region less than approximately 15 wall units from the wall, the sweep motion dominates over the ejection motion; however, the ejection motion dominants farther from the wall (Wallace et al. 1972). This result is consistent with what was found from analysis of numerical simulations of channel flow at $Re = 3300$ (Kim et al. 1987). Katul et al. (2006a) studied the relative importance of sweeps and ejections to momentum transfer and concluded that in the outer layer ejections dominate momentum transfer while in neutral surface layer sweeps and ejections are approximately of equivalent importance to momentum transfer.

1.2.2 Coherent Structures in the CSL

A consensus has been reached for decades that canopy turbulence is dominated by large-scale coherent structures of the whole canopy scale, opposing the earlier paradigm, where the CSL is considered to be a superposition of plant wakes and the surface layer (SL) (Raupach and Thom 1981; Finnigan 2000). The results of quadrant

analysis applied on canopy studies show that sweeps are the major contributor to momentum transfer for dense canopies, and, ejections are the next most important contributor (see e.g., Finnigan 2000). The contribution of sweeps to momentum transfer is individually large and intermittent: typically half the total contribution from sweeps comes from events greater than ten times of its ensemble average, and half the momentum is transferred in less than ten percent of the total time (Finnigan 1979b; Shaw et al. 1983). Poggi et al. (2004b) studied the effects of vegetation density on the dominance of sweep/ejection motions, and concluded that the dominance tends to switch from ejections to sweeps as the canopy vegetation density increases. Within the CSL, large-scale structures are demonstrated as weak ejections followed by strong sweeps in the streamwise-vertical plane; in the spanwise-vertical plane these structures consist of a pair of counter-rotating streamwise vortices centered above the canopy and capture large fraction of the total TKE (Finnigan and Shaw 2000).

Raupach et al. (1996) systematically compared turbulent flows within the CSL and the plane mixing layer (PML) based on flow statistics and turbulent length scales, and concluded that canopy turbulence can be patterned on the PML. One of the compelling evidences is that the ratio of the streamwise separation between adjacent coherent eddies Λ_x over the shear length L_s, which basically determines the spatial arrangement of turbulent structures along the streamwise direction, matches well with the value computed from experiments and numerical simulations in full-developed

mixing layer (Raupach et al. 1996). However, canopy turbulence resembles the PML only in the presence of a homogeneous and 'sufficiently dense' canopy, and this resemblance gradually disappears as the canopy vegetation density decreases. In the extreme case, i.e., in the absence of a canopy, atmospheric flows can be modeled as a rough-wall boundary layer. Based on this fact, Poggi et al. (2004b) proposed a phenomenological model for canopy flows of intermediate vegetation densities, which assumes that near the canopy top the flow field is a superposition of a boundary layer over rough surface and a PML.

1.2.3 Detection Techniques

The specific details of the definition of coherent structures tend to vary across the different identification techniques. Robinson (1991), for example, split the history of coherent structures research within turbulent boundary layer into four eras: the discovery era (1932-59), the flow-visualization era (1960-71), the conditional-sampling era (1972-79) and the computer-simulation era (1980-present). The flow visualization technique is the most straightforward way to detect coherent structures. However, it suffers from the following limitations: (i) it employs dye, particles, bubbles and/or smoke to visualize large structures, and therefore is susceptible to artifacts introduced by the tracers (Robinson 1991); (ii) digitizing of images results in possible information loss and corruption; (iii) visualization methods are more applicable to low-Reynolds-number (lo-Re) flows (Robinson 1991); and, (iv) it is expensive in nature to build up the

required experimental facilities. The conditional sampling methods collect data on ensembles of turbulent events using some predefined triggering condition. However, since each sampling method uses a different triggering condition, turbulent structures identified by different sampling methods may vary significantly. The availability of three-dimensional turbulence data, provided by numerical simulation techniques, has allowed more sophisticated statistical techniques, such as the proper orthogonal decomposition (POD), to be used for the detection of coherent structures. The POD technique solves an eigen-problem for the two-point correlation tensor of a turbulent velocity field. The geometrical information of coherent structures is then contained in eigenvectors, with the associated eigenvalues indicating the relative importance of these eigenvectors in contributing to the total TKE. Unlike conditional sampling methods, the POD is objective in the sense that the extracted structure retains the TKE optimally (Holmes et al. 1996). Although this method can apply to experimental data as well, its use with simulation data is more popular than with experimental data because of the inherent difficulty in collecting the experimental data needed to construct a two-point correlation tensor in the three-dimensional space (Finnigan and Shaw 2000).

1.3 *Overview of Contributions*

The main contributions of this work are as follows:

- Justification of the ability of the LES in producing large-scale coherent turbulent structures.

- Investigation of the effects of vegetation density on coherent turbulent structures and their length scales within the CSL.
- Investigation of coherent turbulent structures across a strong vegetation discontinuity.
- Investigation of the role of the coherent structures on scalar dissimilarity within the CSL.

In Chapter 2, we introduce the LES, which is the major tool used to simulate land-atmosphere interaction in this work, as well as the POD, which is the primary technique used to educe the coherent structures.

In Chapter 3, the ability of LES in simulating large-scale coherent structures is justified by comparing the coherent structures obtained from LES of ABL and from DNS of channel flow. This is important because LES does not simulate small-scale turbulent motions, which do interact with the large-scale coherent structures to some extent, thereby raising the question if LES is able to simulate realistic coherent structures.

Chapter 4 investigates the effects of vegetation density on the coherent structures within the CSL, which is motivated by the fact that variation in vegetation density is one of the major characteristics of the terrestrial ecosystem and turbulent transport is governed by intrinsically different mechanisms between a rough-wall boundary-layer and the CSL.

Chapter 5 studies how the coherent structures change across a strong vegetation discontinuity (i.e. the forest-to-clearing transition and the clearing-to-forest transition). The organization of turbulence, represented as the percentage contribution of the coherent structures to the total TKE, is presented as a function of fetch downstream of the discontinuity point.

Chapter 6 examines the role of the coherent structures on scalar dissimilarity in the CSL. This is important because scalar similarity is widely assumed in models and interpretation of experiments and because coherent structures carry the information of

source/sink dissimilarity of scalars, which is considered to be the major reason responsible for scalar dissimilarity.

2 Methodology

2.1 *Large-Eddy Simulation*

Currently, LES is the state-of-the-art computational tool for investigating the structure of hi-Re turbulence in a wide variety of settings. Its use for modeling the ABL goes back to the pioneering work of Deardorff (1970) and since then, developments in LES have been proliferating. Unlike DNS, LES does not resolve all the scales but models small-scales from an arbitrary grid-linked cut-off point down to the Kolmogorov dissipation scale. Consequently, it enjoys a computational economy that allows LES to simulate hi-Re flows that remain beyond the reach of the DNS techniques. Comparing with the traditional Reynolds-averaged models (e.g. Wilson and Shaw 1977; Raupach 1988; Katul and Albertson 1998), where all turbulent quantities are averaged out and represented in total with a closure model, the LES technique simulates the dominant flow instabilities and formation of 3D turbulent eddies, thereby supporting a richer analysis of the dynamics of turbulent transport.

In Chapter 2.1.1, the general governing equations of LES are introduced; Chapter 2.1.2 describes the strategy to represent vegetation canopies in LES; Chapter 2.1.3 lists the major parameters of LES experiments performed in this work.

2.1.1 Governing Equations

Modified versions of the LES code described in Albertson (1996) and Albertson and Parlange (1999b, a) were used throughout this work. This code solves the filtered equations based on conservation of momentum and mass without the consideration of the Coriolis force for turbulent flows as,

$$\frac{\partial u_i}{\partial x_i} = 0, \tag{2.1}$$

$$\frac{\partial u_i}{\partial t} + u_j\left(\frac{\partial u_i}{\partial x_j} - \frac{\partial u_j}{\partial x_i}\right) = -\frac{\partial p}{\partial x_i} - \frac{\partial \tau_{ij}}{\partial x_j} + \beta\delta_{i3} + f_i, \tag{2.2}$$

$$\frac{\partial \theta}{\partial t} + u_j\frac{\partial \theta}{\partial x_j} = -\frac{\partial \pi_j^{\theta}}{\partial x_j} + h, \tag{2.3}$$

$$\frac{\partial q}{\partial t} + u_j\frac{\partial q}{\partial x_j} = -\frac{\partial \pi_j^{q}}{\partial x_j} + e, \tag{2.4}$$

$$\frac{\partial c}{\partial t} + u_j\frac{\partial c}{\partial x_j} = -\frac{\partial \pi_j^{c}}{\partial x_j} + \eta, \tag{2.5}$$

where t is time, u_i is the filtered velocity in direction x_i. x_1, x_2 and x_3, or x, y and z denote the streamwise, spanwise and vertical directions, respectively. And u_1, u_2 and u_3, or u, v and w are the velocity components in the corresponding directions. p is the pressure normalized by the density, τ_{ij} is the subgrid stress tensor, β is the buoyancy term accounting for the influence of temperature field on the vertical momentum equation, δ_{ij} is the Kronecker delta, θ is the potential air temperature, q is the humidity, c is the CO_2 concentration. π_j^{θ}, π_j^{q} and π_j^{c} are the subgrid flux of temperature, humidity and CO_2 concentration in the *j* direction, respectively. f_i, h, e, η are the source/sink terms of momentum in the *i* direction, temperature, humidity and CO_2, respectively, which are associated with the representation of vegetation canopy.

2.1.2 Representation of Vegetation Canopies

Vegetation canopies are represented as a combined effect of sources/sinks of momentum, temperature, humidity and CO_2 in our LES. The spatial structure of canopy is quantified by local leaf area density $a(x, y, z)$ (LAD, area of plant surface per unit volume). An integration of $a(x, y, z)$ over the vertical range of the canopy results in the leaf area index (LAI), given by,

$$\mathrm{LAI}(x, y) = \int_0^h a(x, y, z) dz \,, \tag{2.6}$$

where h is the canopy height. Figure 2.1 presents the two canopy structures used in this work: an idealized one where the lower portion is uniform and the upper portion gradually decreases to zero, and a realistic one measured at the Duke Forest (Ellsworth et al. 1995), which is characterized by a primary peak around $z/h = 0.6$ and a secondary peak around $z/h = 0.45$. The drag force term is then modeled as linear in LAD and quadratic with velocity,

$$f_i = -C_d a \tilde{u} u_i \,, \tag{2.7}$$

where $\tilde{u} = \left(u_1^2 + u_2^2 + u_3^2\right)^{1/2}$ is the modulus of the wind speed and C_d is an empirical drag coefficient.

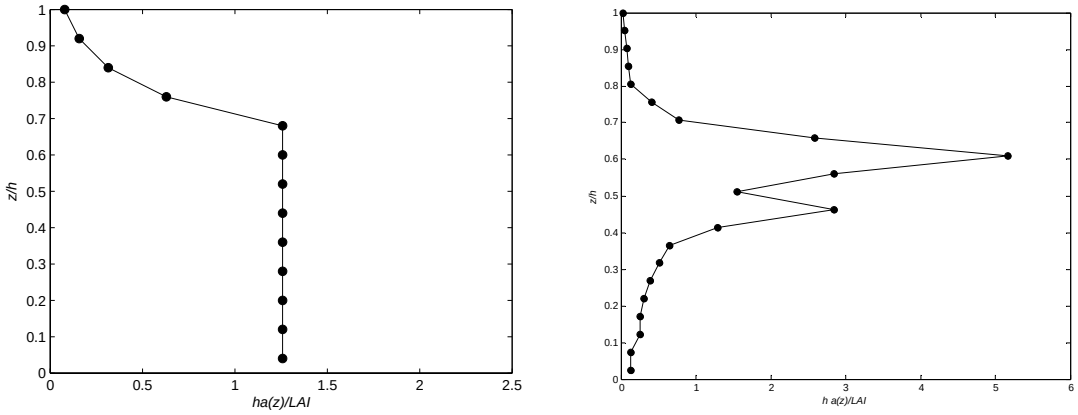

Figure 2.1. Vertical distributions of leaf area density normalized by canopy height and LAI. The left panel represents an idealized profile while the right panel represents a realistic profile measured at the Duke Forest

Since the focus in Chapter 6 is on scalar transport coupled to canopy turbulence, the source/sink distribution of scalars is simulated as well. h, e and η are estimated following biophysical considerations described in Albertson et al. (2001), which act to maximize carbon assimilation while minimizing water loss. LES is performed under a single mid-day period with high sun angle and a net all-wave radiation of $R_n = 500\ \mathrm{W\ m^{-2}}$. R_n and the photosynthetically active radiation (PAR), which is a major constraint for the local carbon assimilation rate, are distributed vertically through the canopy using a simple radiative algorithm (Campbell and Norman 1998; Albertson et al. 2001). The latent heat flux Q_E and the sensible heat flux Q_H at the soil surface are estimated with the Priestley-Taylor formulation under the assumption of saturated soil moisture:

$$Q_E = \frac{\Delta\alpha\left(R_n^s - Q_G\right)}{\Delta + \gamma}, \tag{2.8}$$

$$Q_H = R_n^s - Q_G - Q_E, \tag{2.9}$$

where R_n^s is the net radiation at the soil surface, Q_G is the soil heat flux estimated as $Q_G = 0.15R_n^s$ (Stull 1988), $\alpha\left(=1.26\right)$ accounts for large-scale advection and entrainment, $\gamma\left(=0.67 \text{ mbar } {}^{o}\text{C}^{-1}\right)$ is the psychrometric constant and $\Delta\left(\text{mbar } {}^{o}\text{C}^{-1}\right)$ is the slope of the saturation vapor pressure curve (Campbell and Norman 1998).

2.1.3 Experiments Performed

Twelve LES experiments are performed for the specific topics involved in Chapter 3-6. For Chapter 3, an LES experiment is performed to simulate the ABL. For Chapter 4, to study the effects of vegetation density on the coherent structures within the CSL, five LES experiments are performed to simulate the CSL covering a range of LAI, viz., 0.0625, 0.25, 1, 4, 16 ($m^2\ m^{-2}$) to simulate extremely sparse canopy (ESC), very sparse canopy (VSC), slightly sparse canopy (SSC), slightly dense canopy (SDC), and extremely dense canopy (EDC), respectively. Chapter 5 simulates turbulent flows across a forest-clearing-forest transition with the ratio between the streamwise extent of the forest part and that of the clearing part r varying from 1/3 to 3. All the experiments mentioned above do not simulate the dynamics of scalar transport. However, the LES experiments performed for Chapter 6 simulate the CSL including the exchanges of CO_2, water vapor and heat between the canopy and the atmosphere. Also, the simulations of Chapter 3-5 will be performed on two nested computational staggered grids. Following

the method discussed in Khanna and Brasseur (1997) and Sullivan et al. (1996), an approach of one-way coupling between the two grids will be adopted, implying that the nested grid receives boundary conditions through interpolation of coarse mesh grids, without feedback from the nested grid to the coarse one. This procedure allows for a higher resolution both vertically and horizontally. The parameters of the twelve numerical experiments are tabulated in Table 2-1. z_0 represents the roughness length.

Table 2-1. List of parameter settings for experiments performed in Chapter 3-6

Chapter #		3	4	5	6
Flow		ABL	CSL	Vegetation Discontinuity	CSL
z_0 **(m)**		0.1	0.05	0.05	0.1
Node (#)	**Coarse**	64×64×64	64×32×41	64×32×41	256×128×56
	Nested	128×128×31	256×128×41	256×128×41	
Domain (m^3)	**Coarse**	3142×3142×500	1257×628×400	1257×628×400	500×250×500
	Nested	3142×3142×120	1257×628×80	1257×628×80	
C_d		N/A	0.2	0.2	0.13
Scalar		Off	Off	Off	On
Note			LAI=0.0625, 0.25, 1, 4, 16	LAI=4/0; r=1/3, 1, 3	LAI=1, 5, 9

2.2 *Quadrant Analysis*

In quadrant analysis, four quadrants are identified through the combination of the signs of u' and w' with each quadrant standing for one type of coherent event, viz., Quadrant I ($u' > 0$ and $w' > 0$) for outward interaction, Quadrant II ($u' < 0$ and $w' > 0$) for ejection, Quadrant III ($u' < 0$ and $w' < 0$) for inward interaction and Quadrant IV ($u' > 0$ and $w' < 0$) for sweep (e.g. Lu and Willmart 1973; Finnigan 1979b), where the prime represents departures from the corresponding mean quantities. ΔS_0 is a measure

commonly used to quantify the relative importance of sweeps to ejections (Raupach 1981), defined as

$$\Delta S_0 = \frac{\overline{u'w'}|_{\text{sweeps}} - \overline{u'w'}|_{\text{ejections}}}{\overline{u'w'}}. \tag{2.10}$$

Although ΔS_0 is originally defined for stress, we extend the definitions of sweep and ejection to scalar transport as well in Chapter 6 with the quadrants of sweep and ejection being dependent on the sign of the local flux. For positive local fluxes (e.g. latent heat flux and sensible heat flux in the entire CSL and CO_2 flux near the ground) the sweeps are in quadrant III and ejections in quadrant I. The opposite is true for negative local fluxes (e.g. CO_2 flux in upper canopy and above).

2.3 *Proper Orthogonal Decomposition*

The POD technique is used in this work to educe the 3D coherent structures. Originally, it was introduced to the study of turbulence by Lumley (1967, 1970, 1981). In comparison with other detection techniques of the coherent structures, such as conditional sampling and wavelet transform, one merit of the POD lies in that it gives the coherent structures a clear physical interpretation in the sense that the coherent structure shapes identified by the POD optimally and objectively capture the ensemble-averaged variance of turbulent quantities, the TKE in the case of velocity components, while the criterion of the others are more or less arbitrary. This technique is outlined

here for completeness while comprehensive reviews can be found in Sirovich (1987a, b, c), Berkooz et al. (1993) and Holmes et al. (1996).

Let us first introduce the objects which will be analyzed using the POD before getting into the detailed analysis. Throughout this work, three possible state vectors $\boldsymbol{\beta} = \beta_i$ (where i denotes the index of the variables) are generally considered. In Chapter 3-6 we consider the state vector containing only the velocity components (and hence is sensitive only to the TKE), $\boldsymbol{\beta_1} = [u', v', w']$, and in Chapter 6 we additionally consider the other two: one is an augmented vector that includes the scalars of interest (and hence is partially sensitive to the coupling between the scalar source strength and the flow), $\boldsymbol{\beta_2} = [\tilde{u}', \tilde{v}', \tilde{w}', \tilde{c}', \tilde{q}', \tilde{\theta}']$ where $\tilde{u}_i' = u_i'/u*$,

$u* = \left(1/(3H)\int_H \left(\overline{u'^2 + v'^2 + w'^2}\right)dz\right)^{1/2}$, and for each scalar (e.g. s) $\tilde{s}' = s'/s*$,

$s* = \left(1/H \int_H \overline{s'^2}\, dz\right)^{1/2}$ and H is the vertical region of interest. This scaling strategy for $\boldsymbol{\beta_2}$ forces the velocity components contribute equally as the scalar components to the target of optimization in the POD, i.e., $\int_H \left(\overline{\tilde{u}'^2 + \tilde{v}'^2 + \tilde{w}'^2}\right)dz = \int_H \left(\overline{\tilde{c}'^2 + \tilde{q}'^2 + \tilde{\theta}'^2}\right)dz$. The third one contains only the three normalized scalars, i.e., $\boldsymbol{\beta_3} = [\tilde{c}', \tilde{q}', \tilde{\theta}']$.

2.3.1 One-Dimensional Analysis

Consider an ensemble of $\beta_i(z)$ realizations, each denoting a vertical profile of a variable of interest β_i at an arbitrary (x, y, t) on a finite vertical domain H. The central objective of POD analysis is to decompose an ensemble of realizations $\beta_i(z)$ into a

sequence of orthogonal functions, which is optimal in the sense of capturing as much of the total variance as possible in a finite number of functions. This constraint is equivalent to solving an eigen-problem based on the two-point correlation tensor,

$$\int_H R_{ij}(z,\tilde{z})\phi_j(\tilde{z})d\tilde{z} = \lambda\phi_i(z), \tag{2.11}$$

where the correlation tensor $R_{ij}(z,\tilde{z}) = \langle \beta_i(z)\beta_j(\tilde{z}) \rangle$, the ~ over z represents a second position, and $\langle\ \rangle$ represents an ensemble average for one-dimensional analysis. For discrete implementations, the number of the solutions is proportional to the size of $R_{ij}(z,\tilde{z})$, i.e., the number of computational nodes in the vertical profile. In order to mark individual solutions of this eigen-problem, an index m is added such that an eigenfunction can be represented as $\phi_i^{(m)}(z)$ and the associated eigenvalue as $\lambda^{(m)}$, which indicates the relative importance of the corresponding eigenfunction $\phi_i^{(m)}(z)$ to the total variance. Following Finnigan and Shaw (2000), we define eigenmode as an eigenfunction scaled by the square root of the corresponding eigenvalue, i.e., $\psi_i^{(m)}(z) = \left(\lambda^{(m)}\right)^{1/2}\phi_i^{(m)}(z)$, such that $\psi_i^{(m)}(z)$ contains the information of both the spatial structure and its importance toward the variance. The eigenfunctions are orthogonal and a normalization condition can be imposed so that,

$$\int_H \phi_i^{(m)}(z)\phi_i^{(n)*}(z)dz = \delta_{mn}, \tag{2.12}$$

where * denotes the complex conjugate. Note that * can be dropped for the current application of one-dimensional analysis because $\beta_i(z)$ are real-valued quantities; however, operations of complex numbers will be involved in multi-dimensional analysis. Each realization of $\beta_i(z)$ can be reconstructed by superposing the eigenfunctions,

$$\beta_i(z) = \sum_m a_m \phi_i^{(m)}(z), \tag{2.13}$$

where the coefficients a_m are defined for each realization as,

$$a_m = \int_H \beta_i(z) \phi_i^{(m)*}(z) dz \,. \tag{2.14}$$

The coefficients of different order are uncorrelated:

$$\left\langle a_m a_n^* \right\rangle = \delta_{mn} \lambda^{(m)}. \tag{2.15}$$

Consequently, the variance and covariance are determined from the eigenvalues and eigenvectors,

$$\left\langle \beta_i \beta_j \right\rangle = \sum_m \lambda^{(m)} \phi_i^{(m)}(z) \phi_j^{(m)*}(z). \tag{2.16}$$

Letting $i = j$ and integrating both sides of (2.16) over z, we get an expression relating the integrated variance to the eigenvalues $\lambda^{(m)}$,

$$E = \int_H \left\langle \beta_i \beta_i \right\rangle dz = \sum_m \lambda^{(m)} \,. \tag{2.17}$$

With $\lambda^{(1)} \geq \lambda^{(2)} \ldots \geq \lambda^{(m)}$, the mode associated with the first eigenvalue contributes the most to the variance, and then the second, and so on. In this wrok, the first eigenmode will be generally referred to as the large-scale coherent structure in both the one- and multi-dimensional analysis. Details for the discretization of the eigen-problem (2.11) are specified in Moin and Moser (1989), Finnigan and Shaw (2000) and Smith et al. (2005), and will not be repeated here.

2.3.2 Multi-Dimensional Analysis

The one-dimensional analysis depicts the vertical profile of the turbulent structures. However, it provides no direct horizontal description of these structures. To reveal richer spatial features it is necessary to conduct multi-dimensional POD analysis.

The most straightforward way to implement multi-dimensional analysis in discrete space is to convert the multi-dimensional problem into a one-dimensional problem by unraveling all the grid points into one dimension. However, this approach is hindered by at least two factors. First, the associated eigenvalue problem may be unachievable with the current computation capability due to its large size; Second, POD is not well suited to detect coherent structures in homogenous directions. However, homogeneity is broadly assumed for one- or multi-dimensions in turbulence simulations (Holmes et al. 1996). Mathematically homogeneity implies translational invariance. The averaged two-point correlation function $R(x,\tilde{x})$ is said to be homogeneous if $R(x,\tilde{x}) = R(x-\tilde{x})$. Thus (2.11) can be solved by substituting Fourier representations of $R(x,\tilde{x})$,

$$R(x,\tilde{x}) = \sum_k c_k e^{2\pi i k(x-\tilde{x})}, \tag{2.18}$$

which implies that $e^{2\pi i k x}$ are exactly the eigenfunctions associated with eigenvalues c_k. However, Fourier modes are not suitable to be treated as coherent structures since they are not spatially localized (Holmes et al. 1996).

Lumley (1981) suggested the use of the shot-effect expansion to remedy the difficulty with the POD in homogenous directions. This technique assumes that the field of turbulent quantities in a homogeneous direction is the convolution of coherent structure and a random function. Assuming that we have a three-dimensional turbulence simulation and that x and y are the homogeneous directions and z is the inhomogeneous direction, the shot-effect expansion can be written as:

$$\beta_i(x, y, z, t) = \iint_D \psi_i^{(1)}(x - \tilde{x}, y - \tilde{y}, z) g(\tilde{x}, \tilde{y}, t) d\tilde{x} d\tilde{y}\,, \tag{2.19}$$

where ψ_i^c is the three-dimensional coherent structure, g is a stochastic function and D is the horizontal plane of the simulation domain. To force $\psi_i^{(1)}$ to retain as much of the second-order moment of β_i as possible, we require that g is 'white', implying the second-order moment of the process g is a δ function in the sense of:

$$\langle g(x, y, t) g(\tilde{x}, \tilde{y}, t) \rangle_t = \delta(x - \tilde{x}, y - \tilde{y}), \tag{2.20}$$

Then by Campbell's theorem we obtain the two-point correlation tensor as:

$$R_{ij}(r_x, r_y, z, \tilde{z}) = \iint_D \psi_i^{(1)}(x, y, z) \psi_j^{(1)}(x + r_x, y + r_y, \tilde{z}) dx dy\,. \tag{2.21}$$

Taking Fourier transforms of (2.21) with respect to r_x and r_y, we get

$$\Phi_{ij}(k_x, k_y, z, \tilde{z}) = \hat{\psi}_i^{(1)}(k_x, k_y, z) \hat{\psi}_j^{(1)*}(k_x, k_y, \tilde{z}). \tag{2.22}$$

It is clear that from (2.22) we can obtain the amplitude of $\hat{\psi}_i^{(1)}$ but not its phase angle:

$$\left|\hat{\psi}_i^{(1)}(k_x, k_y, z)\right| = \left|\Phi_{ii}(k_x, k_y, z, z)\right|^{1/2}. \tag{2.23}$$

On the other hand, following the one-dimensional procedure, a POD analysis on each wavenumber of the spectral-density tensor Φ_{ij} presents the optimal decomposition:

$$\hat{\beta}_i(k_x, k_y, z, t) = \sum_m \hat{a}_m(k_x, k_y, t) \hat{\phi}_i^{(m)}(k_x, k_y, z). \tag{2.24}$$

and

$$\left\langle \hat{a}_m\left(k_x, k_y, t\right)\hat{a}_n^*\left(k_x, k_y, t\right)\right\rangle_t = \lambda^{(n)}\left(k_x, k_y\right)\delta\left(m, n\right). \tag{2.25}$$

It is the first component in (2.24) that bridges the shot-effect expansion and the instantaneous velocity data together:

$$\hat{\beta}_i^{(1)}\left(k_x, k_y, z, t\right) = \hat{a}_1\left(k_x, k_y, t\right)\hat{\phi}_i^{(1)}\left(k_x, k_y, z\right), \tag{2.26}$$

where $\hat{\beta}_i^{(1)}$ represents the first mode component of $\hat{\beta}_i$.

The two-point spectral density tensor of $\hat{\beta}_i^{(1)}$ can be computed as:

$$\Phi_{ij}^{(1)}\left(k_x, k_y, z, \tilde{z}\right) = \lambda^{(1)}\left(k_x, k_y\right)\hat{\phi}_i^{(1)}\left(k_x, k_y, z\right)\hat{\phi}_j^{(1)^*}\left(k_x, k_y, \tilde{z}\right). \tag{2.27}$$

Similar as the derivation from (2.22) to (2.23), the amplitude of $\Phi_{ii}^{(1)}$ is obtained from (2.27) as:

$$\left|\Phi_{ii}^{(1)}\left(k_x, k_y, z, z\right)\right|^{1/2} = \left(\lambda^{(1)}\left(k_x, k_y\right)\right)^{1/2}\left|\hat{\phi}_i^{(1)}\left(k_x, k_y, z\right)\right|. \tag{2.28}$$

Comparing (2.26) with the Fourier transform of (2.19):

$$\hat{\beta}_i\left(k_x, k_y, z, t\right) = \hat{g}\left(k_x, k_y, t\right)\hat{\psi}_i^{(1)}\left(k_x, k_y, z\right), \tag{2.29}$$

we may let $\hat{\beta}_i^{(1)}$ approximate $\hat{\beta}_i$ and consequently, $\left|\Phi_{ii}^{(1)}\right|$ approximate $\left|\Phi_{ii}\right|$. However, even with the assistance of the shot-effect expansion, the POD still leaves the phase angles undetermined, which are essential to the geometrical interpretation of coherent structures.

Currently, three methods have been proposed to retrieve the phase information, all of which impose certain physical properties on the derived coherent structures. The first method is the bispectrum or three-point correlation criterion (Lumley 1981), which states that coherent structures should conserve as much as possible the three-point correlation of the original velocity field. The method is the only one which is theoretically able to determine the direction or the sense of the rotation of coherent structures. The second method, termed the 'compactness criterion', was originally proposed by Herzog (1986). It assumes that coherent structures should be spatially compact. The third method is called the 'wavenumber continuity' or the 'spectral smoothness' criterion, which implies that the phase angles of coherent structures should be continuous in wavenumber space (e.g. Moin and Moser 1989; Delville et al. 1999).

In this study, the 'compactness criterion' is chosen based on several considerations: 1) unlike the bispectrum criterion, it does not involve any assumption of stochastic process for the function g to bridge the three-point correlation functions of the original velocity field and the coherent structure., 2) the bispectrum criterion is mathematically converted to an over-determined problem of solving an $O\left(N^{2n}\right)$ equation group, where N denotes the grid number in the homogeneous directions and n is the number of the homogeneous directions (the solution of this problem is largely influenced by numerical instability), 3) given that the geometry of coherent structures is very sensitive to the phase angles, it is difficult to obtain consistent results with the

bispectrum criterion, and 4) compared to the spectral smoothness criterion, the compactness criterion focuses separately on each wavenumber component rather than the connection between neighbouring wavenumbers, which makes sense because coherent structures have most of their energy in the lower wavenumber parts.

In order to apply the compactness criterion, let us consider the vertical integration of the horizontal center of the coherent structure expressed in the streamwise velocity $\int_H \psi_1^{(1)}(0,0,z)dz$ (assume the index 1 represent *u*). The compactness criterion requires the occurrence of the maximum of $\int_H \psi_1^{(1)}(0,0,z)dz$, which then leads to the phase angle expressed as (Herzog 1986; Moin and Moser 1989; Finnigan and Shaw 2000),

$$\xi(k_x,k_y) = -\text{angle}\left(\int_H \hat{\phi}_1^{(1)}(k_x,k_y,z)dz\right). \tag{2.30}$$

With the phase angle of $\hat{\psi}_i^{(1)}$ determined, $\hat{\psi}_i^{(1)}$ can now be expressed as:

$$\hat{\psi}_i^{(1)}(k_x,k_y,z) = \left(\lambda^{(1)}(k_x,k_y)\right)^{1/2} \hat{\phi}_i^{(1)}(k_x,k_y,z)e^{i\xi(k_x,k_y)}. \tag{2.31}$$

And

$$\hat{g}(k_x,k_y,t) = \left(\lambda^{(1)}(k_x,k_y)\right)^{-1/2} \hat{a}_1(k_x,k_y,t)e^{-i\xi(k_x,k_y)}. \tag{2.32}$$

2.3.3 Coherent Structures and Truncated Reconstruction

Because the first POD mode $\psi_i^{(1)}$ statistically carries the greatest percentage of the overall variance of turbulent quantities, it has been treated as a 'coherent structure' or 'characteristic eddy' in a number of applications, such as channel flow (Moin and Moser 1989), PML (Delville et al. 1999), CSL (Finnigan and Shaw 2000) and ABL (Huang

et al. 2009a). In this work, we generally refer to the coherent structures as $\psi_i^{(1)}$ (in 1D, 2D or 3D) while in a similar way referring to the secondary coherent structures as $\psi_i^{(2)}$.

It is possible to obtain a truncated, low-dimensional reconstruction of β_i using only the first several (say *p*) modes. For one-dimensional analysis, the *p*-mode truncated reconstruction can be written as (c.f. equation (2.13)),

$$\beta_i^{(p)}(z) = \sum_{m=1}^{p} a_m \phi_i^{(m)}(z), \tag{2.33}$$

Its contribution to the covariance is described as (c.f. equation (2.16)),

$$\left\langle \beta_i^{(p)} \beta_j^{(p)} \right\rangle = \sum_{m=1}^{p} \lambda^{(m)} \phi_i^{(m)}(z) \phi_j^{(m)*}(z). \tag{2.34}$$

And to the integrated variance (c.f. equation (2.17)),

$$\int_H \left\langle \beta_i^{(p)} \beta_i^{(p)} \right\rangle dz = \sum_{m=1}^{p} \lambda^{(m)}. \tag{2.35}$$

For the case of multi-dimensional analysis, it is similar but a little more complex due to the conversion between physical space and wavenumber space. The *p*-mode truncated reconstruction can be expressed as (c.f. equation (2.24)),

$$\beta_i^{(p)}(x, y, z, t) = \frac{1}{4\pi^2} \sum_{m=1}^{p} \iint \hat{a}_m(k_x, k_y, t) \hat{\phi}_i^{(m)}(k_x, k_y, z) dk_x dk_y. \tag{2.36}$$

And the contribution of $\beta_i^p(x, y, z, t)$ to the total temporal and horizontal averaged covariance is,

$$\left\langle \beta_i^p \beta_j^p \right\rangle = \frac{1}{4\pi^2} \sum_{m=1}^{p} \iint \lambda^{(m)}(k_x, k_y) \hat{\phi}_i^{(m)}(k_x, k_y, z) \hat{\phi}_j^{(m)*}(k_x, k_y, z) dk_x dk_y. \tag{2.37}$$

It follows for the integrated (over z) variance,

$$\int_H \left\langle \beta_i^{(p)} \beta_j^{(p)} \right\rangle dz = \frac{1}{4\pi^2} \sum_{m=1}^{p} \iint \lambda^{(m)}\left(k_x, k_y\right) dk_x dk_y = \sum_{m=1}^{p} \Lambda^{(m)} , \tag{2.38}$$

where

$$\Lambda^{(m)} = \frac{1}{4\pi^2} \iint \lambda^{(m)}\left(k_x, k_y\right) dk_x dk_y , \tag{2.39}$$

and

$$E = \sum_{m=1}^{\infty} \Lambda^{(m)} . \tag{2.40}$$

3 The Atmospheric Boundary-Layer

3.1 *Introduction*

Since DNS is unattainable at typical hi-Re values of the ABL, LES is typically used for the ABL. However, it does not explicitly resolve the viscous sublayer. In fact, the study of land-atmosphere interaction in the ABL makes extensive use of wall stress models, thereby avoiding the need to resolve the viscous sublayer (e.g., Moeng 1984; Mason and Thomson 1992; Sullivan et al. 1996; Kosovic 1997; Albertson and Parlange 1999b, a; Porte-Agel et al. 2000; Piomelli and Balaras 2002; Stoll and Porte-Agel 2006; Cassiani et al. 2008). However, since large-scale coherent structures arise from the interaction of the flow with the wall surface, and small scales, which do interact to some degree with the large-scale dynamics, are modeled as well in LES, there is the need to investigate the ability of LES to produce realistic large-scale coherent structures.

In this chapter, the POD method is applied to extract large-scale coherent structures from a LES database of a hi-Re neutral ABL, with the twofold objectives of investigating the large-scale turbulent structures as well as validating the ability of the LES in producing these structures. The structures are systematically compared to those obtained from a set of freely available DNS data of a lo-Re channel flow to explore similarity and difference of the structures, thereby assessing to which degree LES is able to produce the same turbulent structures as those in DNS. Despite the differences in the two flow types it is expected that the LES should exhibit somewhat similar structures,

since these large-scale coherent structures arise from the same type of primary instability generated by the interaction of the mean flow with the surface, and that the potential differences of the coherent structures in the two simulations should be explainable in terms of the difference of the Reynolds number. In the near-wall region, a nested grid simulation is performed to investigate the effect of grid resolution and grid coupling on the simulated coherent structures. The expectation is to discover the same turbulent structures but with more detail in small scales at the finer spatial resolution. This is also of importance in view of the increasing use and investigation of local grid refinement methods (e.g., Sullivan et al. 1996; Sagaut et al. 2006; Moeng et al. 2007), in order to investigate in more detail the region close to the surface and/or in specific environments (e.g. urban, forest) while maintaining the turbulent forcing of larger scale.

This chapter is structured as follows. The results of one-dimensional POD analysis are presented in Chapter 3.2 and the results of multi-dimensional POD analysis are demonstrated in Chapter 3.3. Chapter 3.4 performs truncated reconstructions of the POD through linear superimposition of varied numbers of eigenfunctions and discusses the potential applications of this technique.

The vertical profiles of the streamwise mean velocity $\langle u \rangle_{xyt}$, the velocity standard deviations $\sigma_u = \langle u'^2 \rangle_{xyt}^{1/2}$, $\sigma_v = \langle v'^2 \rangle_{xyt}^{1/2}$, $\sigma_w = \langle w'^2 \rangle_{xyt}^{1/2}$ and the total (i.e., the sum of the resolved stress and the SGS stress) Reynolds shear stress τ of both grids are shown in

Figure 3.1, where $\langle\ \rangle_{xyt}$ represents averaging over x,y and t and the turbulent velocities are defined as $u_i' = u_i - \langle u_i \rangle_{xyt}$. These profiles are normalized by the friction velocity u_* = 0.3 m s^{-1}, defined as $u_*^2 = \langle u'w' \rangle_{xyt}\,|_{z=\Delta z/2}$. The vertical direction is scaled with the boundary layer depth L_z. It can be seen that the higher resolution allows for a higher fraction of the total TKE to be resolved (Sullivan et al. 1996). Note that σ_u, σ_v and σ_w of the refined grid all peak closer to the wall than in the coarse grid simulation, which is probably attributed to the fact that the scale of dominant structures decreases as the wall is approached. For a full discussion of the limitation and capability of the one-way grid nesting methods in reproducing turbulent statistics we refer to the works of Sullivan et al. (1996) and Khanna and Brasseur (1997).

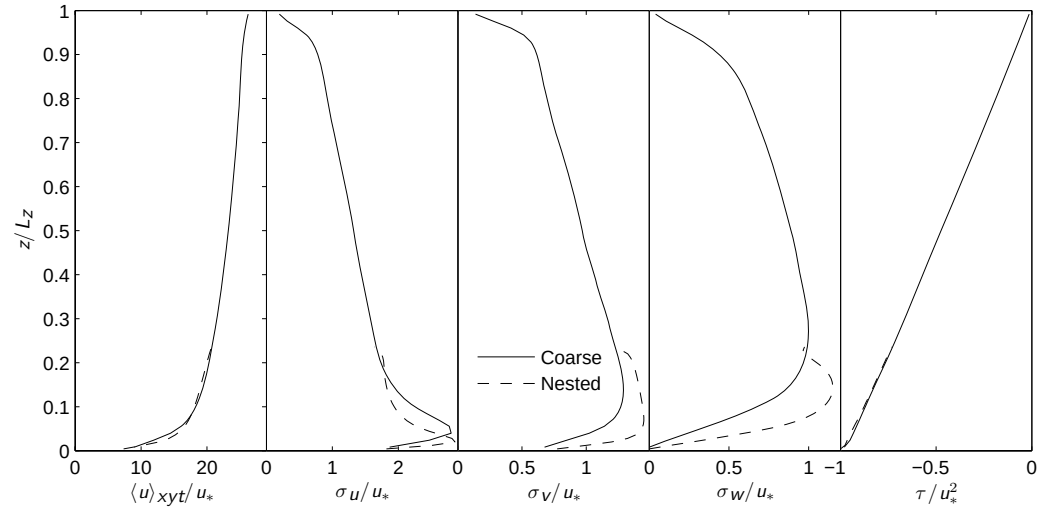

Figure 3.1. Vertical profiles of resolved $\langle u \rangle_{xyt}/u_*$, σ_u/u_*, σ_v/u_*, σ_w/u_* and the total (i.e., the sum of the resolved stress and the SGS stress) stress τ/u_*^2. The solid and dashed lines represent the coarse grid and the nested grid, respectively

A realization of channel flow produced by DNS (DNS channel flow) (http://turbulence.ices.utexas.edu/) is analyzed in comparison with the ABL obtained from our LES (LES ABL) in order to explain possible effects of the SGS model and the wall model on the derived coherent structures. Relevant parameter settings of the DNS are listed here although the detailed methodology can be found in Del Alamo and Jimenez (2001, 2003). The friction Reynolds number is $\mathrm{Re}_\tau = 182$ at Re = 3250 and the normalizing velocity scale is the friction velocity $u_\tau = 0.059$ m s^{-1}. The horizontal resolutions in the x and y directions are $\Delta x^+ \approx 8.9$ and $\Delta y^+ \approx 4.5$ in wall units, respectively. The simulation was carried out with a grid of 768×510×97 nodes in the x, y and z directions, respectively. The Chebyshev polynomial representation was adopted in the z direction.

3.2 *One-Dimensional Analysis*

The first three eigenfunctions of our LES ABL and the DNS channel flow are compared in Figure 3.2. Note that L_z represents the half channel width δ for the DNS channel flow. The features where the LES and DNS are in general agreement include: (1) the number of zero-crossings increase with the eigenmode index except for v of the LES; (2) the signs of the u and w eigenfunctions are opposite over most of z; (3) the general patterns of the u and w eigenfunctions for the two types of simulations are similar. However, there are also significant differences emerging from this comparison: (1) the v eigenmodes $\psi_2^{(1-3)}$ have a noticeable vertical shift between our LES ABL and

the DNS. For example, the zero-corssing of $\psi_2^{(1)}$ occurs approximately at $z/L_z = 0.23$ for the DNS and at $z/L_z = 0.13$ for ABL.

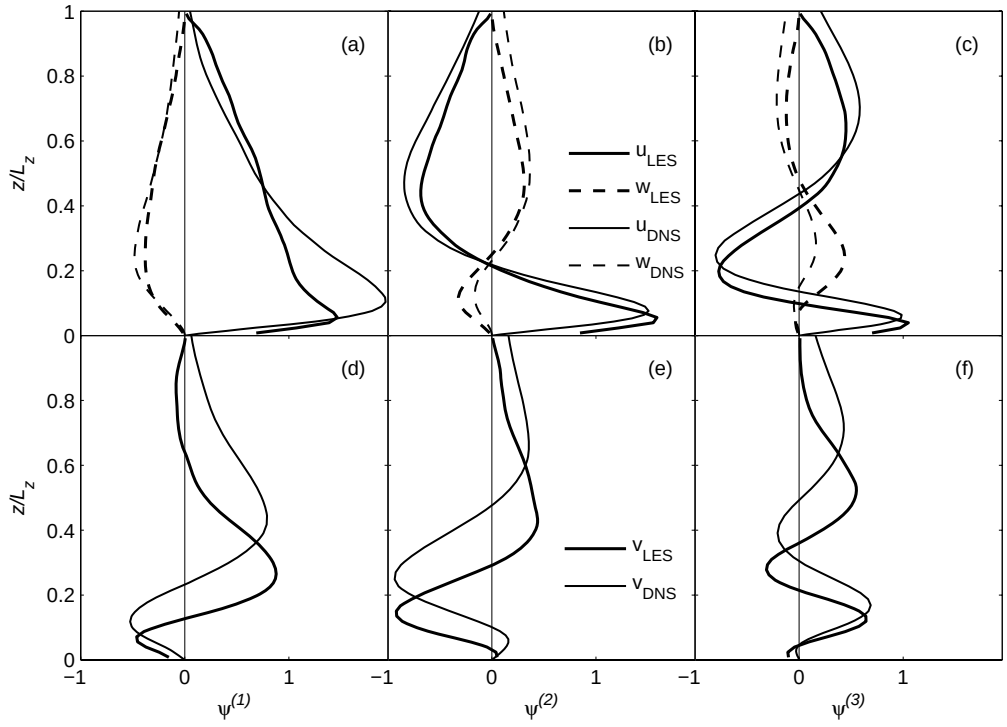

Figure 3.2. Comparison of the first three eigenmodes $\psi^{(1-3)}$ of the entire domain of the LES ABL (thick lines) and the DNS channel flow (thin lines) with (a, b, c) and (d, e, f) representing the (1st, 2nd, 3rd) eigenfunctions, respectively. In (a, b, c), the solid lines and the dashed lines stand for the eigenmodes of u and w, respectively; in (d, e, f), the lines stand for the eigenmodes of v.

As pointed out in Moin and Moser (1989), the sign change of $\psi_2^{(1)}$ is likely to indicate the existence of a streamwise vortex in the vicinity of the wall, and the zero-crossing should be associated with the elevation of the center of this vortex.; (2) interestingly, the first u eigenmode $\psi_1^{(1)}$ also peaks at a higher elevation for the DNS

($z/L_z = 0.10$) than for the LES ($z/L_z = 0.06$). This consistency can be connected back to the hairpin structures in the near wall region and their life cycle mentioned in Chapter 1.2.1: it is the peak of $\psi_1^{(1)}$, which serves as a streamwise gust, that intensifies and curves some pre-existing spanwise vortices, forming the hairpin structures. This issue will be revisited in multi-dimensional analysis. The difference of the elevations of the zero-crossings of $\psi_2^{(1)}$ between the LES and the DNS is not surprising in consideration of the different nature of the two simulated flows. The LES ABL has a much higher Re than the DNS channel flow and at the elevation of $z/L_z = 0.13$ it is fully turbulent presenting very energetic structures. In our simulations the viscous sublayer is not simulated but would be anyway very thin compared to the ABL depth (a few centimeters, see e.g., Stull 1988). On the contrary, in the DNS the effective Re is low and the viscous layer plays a significant role moving the turbulent energetic structure relatively far from the bottom boundary.

In addition to the comparison between the LES and the DNS, we are also interested in the comparison between the coarse grid and the nested grid of the LES because it examines the utility of the nesting technique in revealing additional spatial detail of the same turbulent dynamics as the coarse grid, while maintaining the same boundary conditions. This comparison is performed for the near wall region $z \subset [0, L_n]$ of the ABL, with the similar L_n/L_z ratio as in MM89, i.e., $L_n/L_z \approx 0.22$. The first three

eigenmodes of the coarse grid and the nested grid of the near wall region are shown in Figure 3.3.

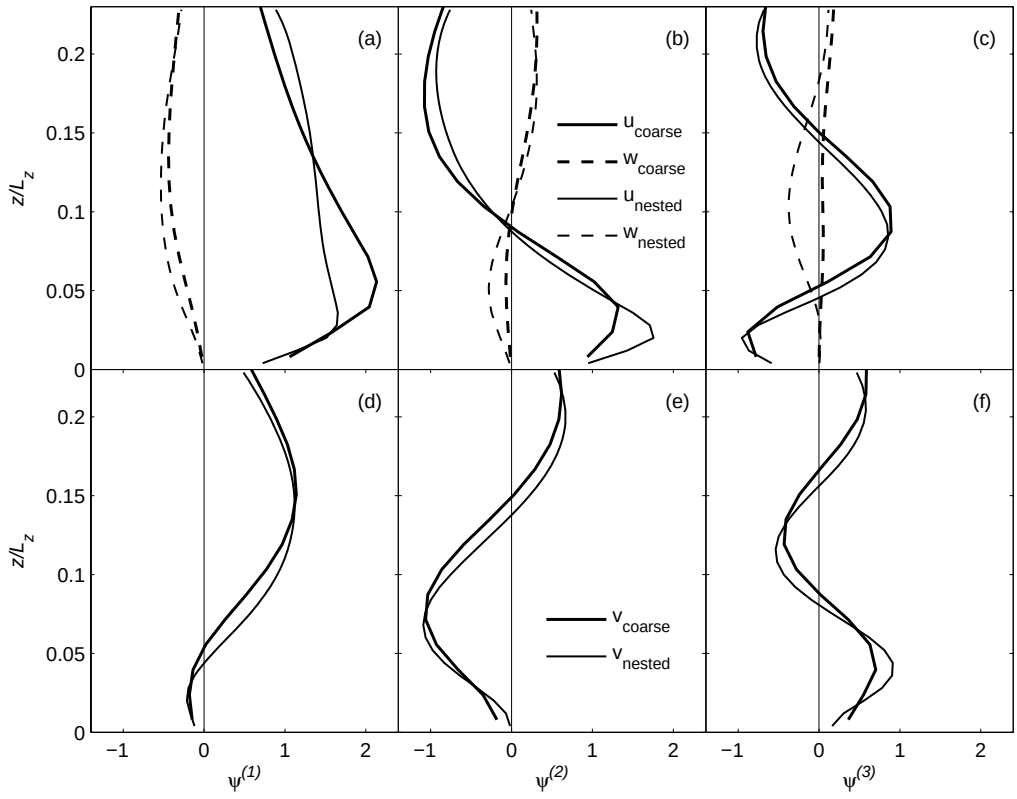

Figure 3.3. Comparison of the first three velocity eigenmodes $\psi^{(1-3)}$ of the coarse grid (thick lines) and the nested grid (thin lines) of the near-wall domain. The line types share the same meanings as in Figure 3.2

We note that the three eigenmodes of the two different resolutions are in a good agreement in terms of the zero-crossing numbers, the relative u and w signs, and the general patterns. However, there are also noticeable differences: (1) the magnitude of $\psi_1^{(1)}$ of the nested grid is considerably smaller than the coarse grid in the region close to

wall. This is likely to arise because the greater number of grid points in the z direction produces more modes in the expansion. Consequently, the first mode represents a smaller percentage of the total TKE; (2) $\psi_1^{(1)}$ and $\psi_1^{(2)}$ of the nested grid peak at a lower z than with the coarse grid. As stated before, this is consistent with the finer resolution being able to simulate smaller eddies as found closer to the wall; (3) the zero-crossing elevation of $\psi_2^{(1)}$ is slightly higher for the coarse grid than for the nested grid.

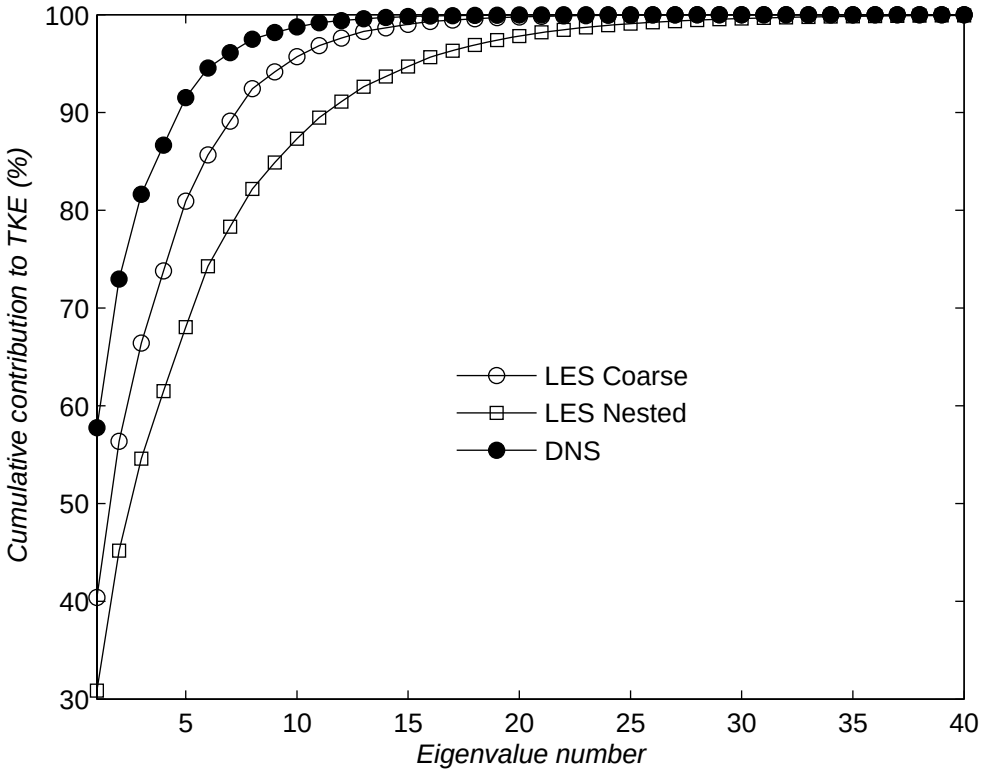

Figure 3.4. Cumulative contribution of eigenvalues to the total TKE in the near-wall domain versus eigenvalue number. The empty circles denote the results computed for the coarse grid of the LES, the empty squares for the nested grid of the LES and the solid circles for the DNS

Figure 3.2 and Figure 3.3 demonstrate the shapes of one-dimensional turbulent structures in the entire vertical domain and the near wall region, respectively. In order to investigate the relative importance of these structures quantitatively and systematically, we turn to Figure 3.4, in which the statistics of the eigenvalues $\lambda^{(m)}$ of the two different LES resolutions and the DNS for the near wall region are showed. As mentioned earlier, the eigenvalues presented here are computed from the ensembles of all three turbulent velocity components. Two features can be clearly observed on the basis of the LES-DNS comparison and the coarse-nested grid comparison: the eigenvalues of the DNS converge faster than those of the LES while the eigenvalues of the nested grid converge slower than those of the coarse grid. The first mode of the DNS represents approximately 58 percent, while this value is 40 and 31 for the coarse grid and nested grid of the LES, respectively. Many factors could affect the convergence rate of the eigenvalues such as, Re, wall roughness, and the number of grid points. Higher Re, smoother wall surface and greater number of grid points are considered to decrease the organization of the simulated flow and hence reduce the convergence rate of the eigenvalues. As stated in interpreting Figure 3.3, it is likely the greater number of grid points in the nested grid gives rise to the slower convergence than the coarse grid. As for the result of the LES-DNS comparison, it is suspected that the much higher Re of LES is the main factor responsible for the low convergence rate of the LES. It is also expected

that eigenvalues will converge faster when z_0 increases in the LES but this has not been tested here.

3.3 *Multi-Dimensional Analysis*

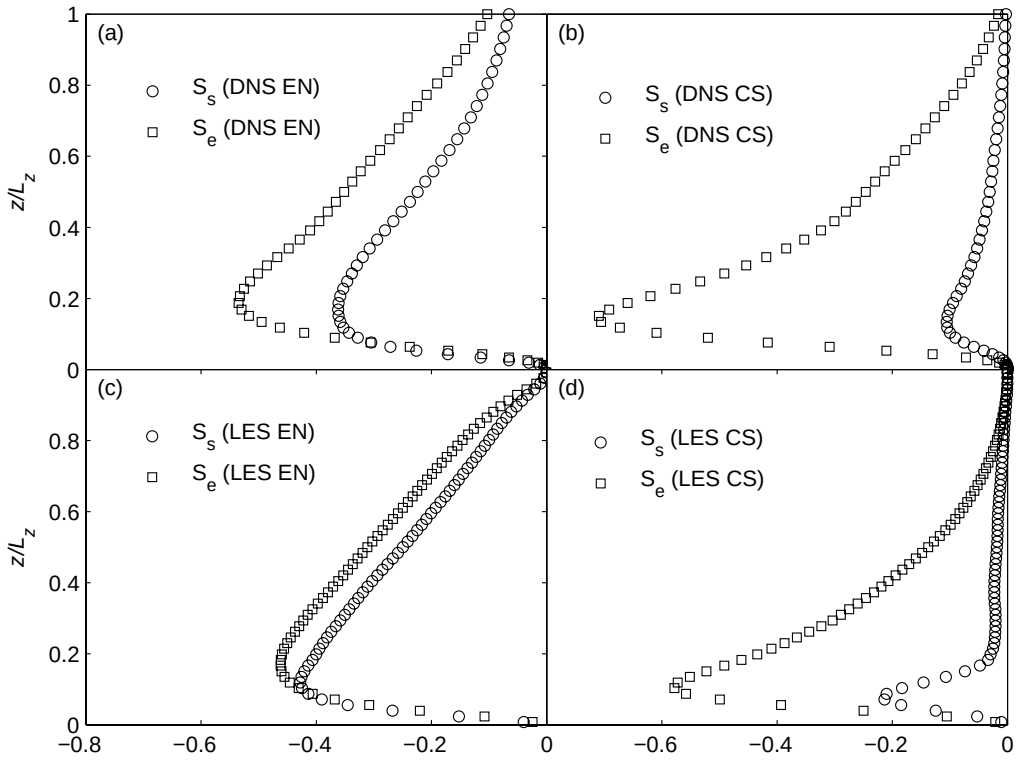

Figure 3.5. Comparison of the vertical profiles of S_s (circle) and S_e (square) for (a) the ensembles of the DNS (DNS EN); (b) $\psi^{(1)}(r_y, z)$ of the DNS (DNS CS); (c) the ensembles of the LES (LES EN) (d) $\psi^{(1)}(r_y, z)$ of the LES (LES CS)

In order to illustrate the determination of the direction of coherent structures, the sweep/ejection profiles $S_s(z)$ and $S_e(z)$ computed from the ensembles (EN) and the two-dimensional coherent structure $\psi^{(1)}(r_y, z)$ (CS) are depicted in Figure 3.5. Note that

$S_s(z)$ and $S_e(z)$ are scaled by u_*^2 for the LES and by u_τ^2 for the DNS, respectively. Figure 3.5a shows that for the DNS sweep dominates over ejection below 14 wall units, or $z = 0.08L_z$; however, the dominance switches above. This result is consistent with what has been discovered for channel flow under experiments (Wallace et al. 1972) and simulations (Kim et al. 1987). For the LES, it can be seen from Figure 3.5c $z = 0.1L_z$ is the critical point for the dominance to switch. It is obvious that the velocity fields of both the LES and the DNS satisfy $S_e^H > S_s^H$, where $H = [0, L_z]$. Therefore, the direction of rotation of coherent structures should be set as in Figure 3.5b and Figure 3.5d such that ejections dominate over sweeps. A noteworthy feature observed from comparing (a) and (b), and (c) and (d), is that the sweep motion plays a much less important role in the coherent structure than in the ensembles of velocity fields. The relative role of ejections to sweeps can be quantified by $r_e = S_e^H / S_s^H$. This value is approximately 1.5 and 1.2 for the ensembles of the DNS and the LES, respectively; but 7.1 and 5.5 for the coherent structure of the DNS and the LES, respectively. It is consistently found that $S_s(z)$ and $S_e(z)$ peak at greater distance from the wall in the DNS than in the LES for the ensembles as well as the two-dimensional coherent structure $\psi^{(1)}(r_y, z)$. This agrees with Figure 3.2, namely that the energetic turbulent structures in the DNS are farther from the wall than in the LES due to the lower Reynolds number and therefore the presence of a more significant viscous layer.

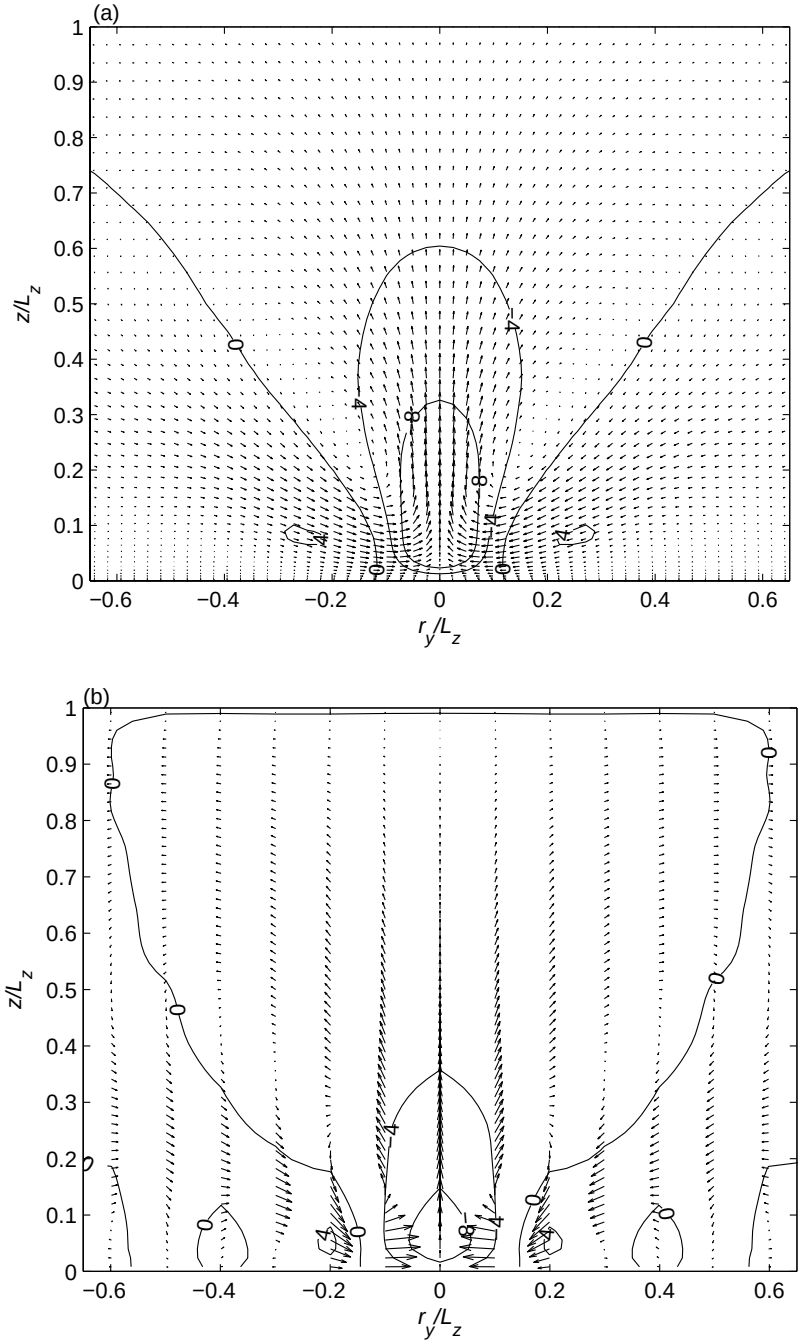

Figure 3.6. The Two-dimensional coherent structures $\psi^{(1)}(r_y, z)$ for the entire domain of (a) the DNS channel flow and (b) the LES ABL. u -contour lines with isovalues labelled are superposed onto $v - w$ vector plot. All the velocity components have been normalized by the friction velocity

With the direction of rotation of coherent structures determined, $\psi^{(1)}(r_y, z)$ of both the DNS and the LES are visualized in Figure 3.6 in the form of the superposition of the u-contour and the $v - w$ vector plots (c.f. Figure 11 in (Moin and Moser 1989)). Note that the isovalues of u on the plot represent the normalized velocity. The normalizing velocity is u_τ for the DNS and u_* for the LES, respectively. The similarities between the DNS channel and the LES ABL appear as: (1) strong ejections in the central area with relatively weak sweeps on both sides; (2) a pair of global flow circulations whose axes are close to and approximately parallel with the u-contour line with the isovalue 0, which roughly indicates the sweep/ejection boundary. The circulations form into a pair of counter-rotating vortices, with the left one rotating counter-clockwise. The specific positions of the vortex centers in (a) and (b) can not be rigorously identified because the overall shape of the circulations is rather flat and also the resolution of LES ABL is not high enough. However, it can still be noticed that the vortices of LES ABL are systematically lower than that in DNS channel flow, which is consistent with the result of the zero-crossings of $\psi_2^{(1)}$ in the one-dimensional analysis.

The comparison in Figure 3.3 has shown a consistent picture between the one-dimensional turbulent structures in the coarse grid and the nested grid of the LES. This comparison can be extended to two-dimensional analysis, as illustrated in Figure 3.7. Note that, as with the one-dimensional analysis, since the nested grid covers only the

lower part of the ABL domain, we need to conduct the two-dimensional analysis for the two different resolutions over the same region (i.e., $z \subset [0, L_n]$) to make this comparison.

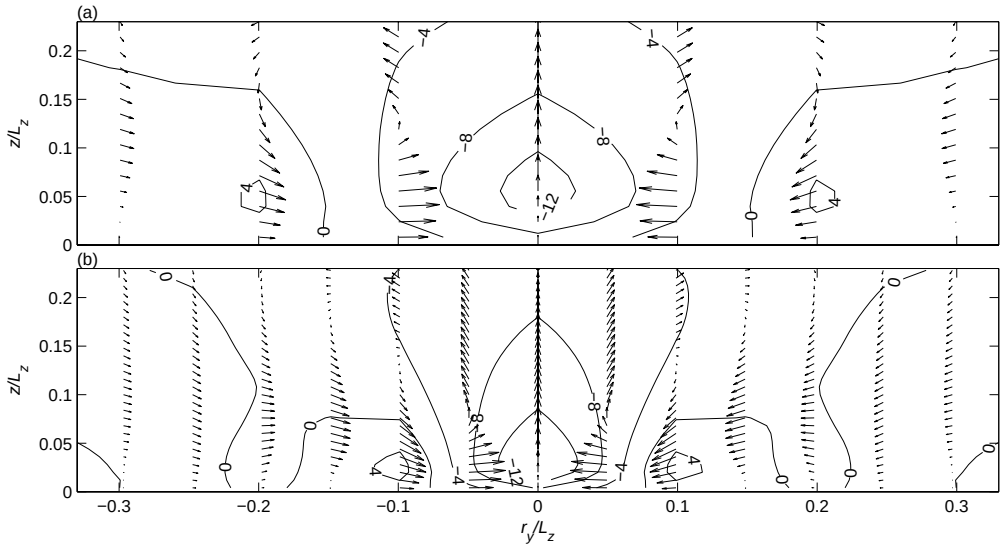

Figure 3.7. The Two-dimensional coherent structures $\psi^{(1)}(r_y, z)$ for (a) the coarse grid and (b) the nested grid of the LES in the near wall domain. u -contour lines with isovalues labelled are superposed onto $v - w$ vector plot. All the velocity components have been normalized by the friction velocity

Both the coarse grid and the nested grid produce strong ejections on the central area and a pair of counter-rotating vortices. Figure 3.7a resembles the near wall portion of Figure 3.6b while Figure 3.7b is basically a better resolved version of Figure 3.7a except that the isovalue lines of 0 and 4 do not go through the same area. The general consistency suggests that the nested grid demonstrates the same dynamics as the coarse grid but with more detail. Owing to this fact, we will only focus on the nested grid henceforward as far as the near-wall region is concerned. Even though the central position of the counter rotating vortices and the global circulations can not be defined

precisely, it is natural to use the v zero crossings to approximate it. In Figure 3.8, the elevations of the v zero crossings z_v are plotted versus the spanwise distance r_y for the two dimensional coherent structures. z_v of the DNS channel is uniformly greater than z_v of the LES ABL by $\sim 0.05L_z$. The tilt angle of inclination is approximately 45° in the area close to the center of the coherent structure ($r_y / L_z < 0.4$), and then decreases gradually as it goes farther outward.

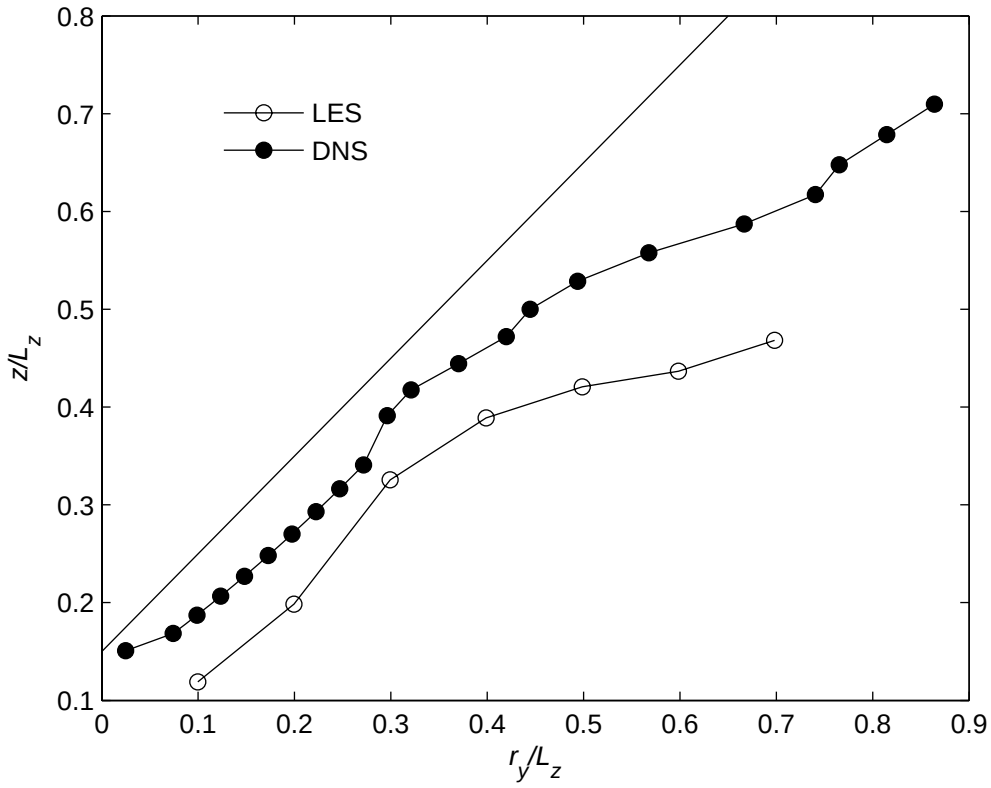

Figure 3.8. Height of zero-crossings of v in $\psi^{(1)}(r_y, z)$ versus r_y for the LES and the DNS channel flow in the entire domain. The straight line with the tilt angle of 45° is also plotted for reference.

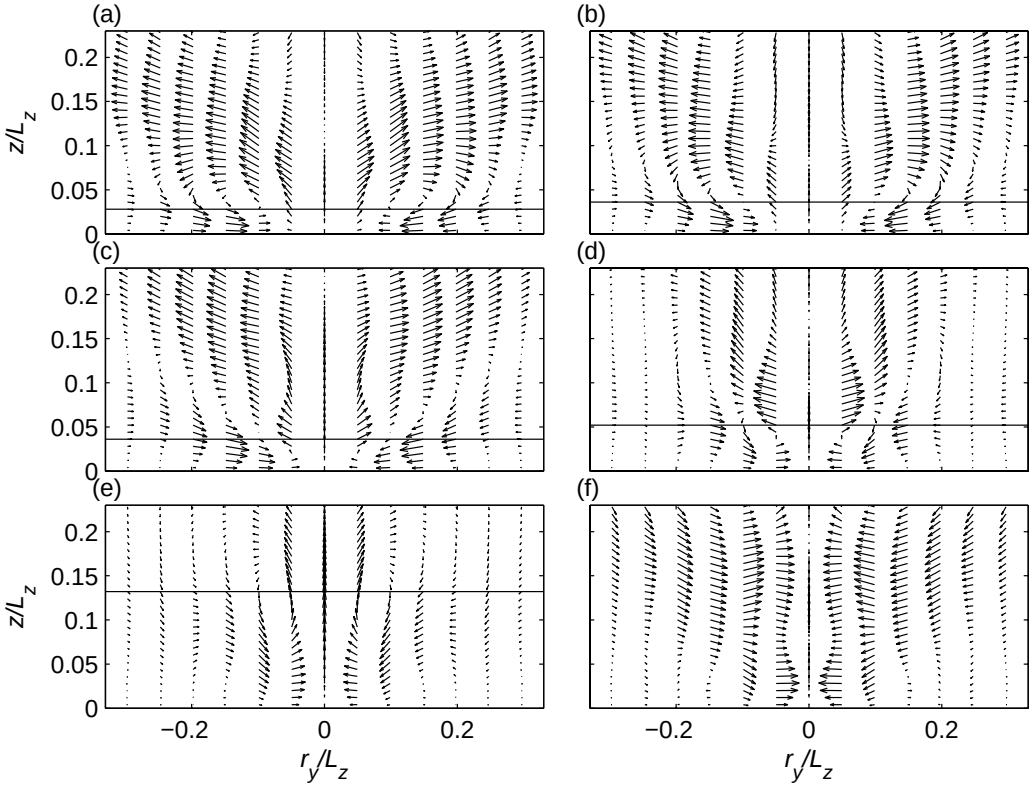

Figure 3.9. $v-w$ **velocity vectors of** $\psi^{(1)}\left(r_x, r_y, z\right)$ **of the nested grid in the near-wall domain of the LES projected onto the** $y-z$ **plane at** $r_x / L_z =$**: (a) -0.4; (b) -0.3; (c) -0.2; (d) -0.1; (e) 0 and (f) 0.1, respectively. The elevations of the** v **zero crossings at** $r_y / L_z = 0.1$ **are plotted as straight lines parallel with the** x **axis except in (f)**

The two-dimensional coherent structure in the *y*-*z* plane represents an effect of statistical average in the *x* direction. In order to understand how the coherent structure is oriented in the streamwise direction x, it is necessary to conduct the three-dimensional analysis. In Figure 3.9, the $v-w$ velocity vectors of cross-section of the three-dimensional coherent structure $\psi^{(1)}\left(r_x, r_y, z\right)$ are projected onto the $y-z$ plane at a range of streamwise locations $r_x/L_z = \{-0.4, -0.3, -0.2, -0.1, 0, 0.1\}$ for the nested

grid. The three-dimensional analysis for the coarse grid obtains similar results and is not shown here. Figure 3.9a-e resembles the two-dimensional structure $\psi_i^{(1)}\left(r_y, z\right)$ in the sense that it consists of a strong ejection in the centre and a double-roller on both sides. The double-roller structure is inclined in the downstream direction (c.f. Figure 17 in (Moin and Moser 1989)).

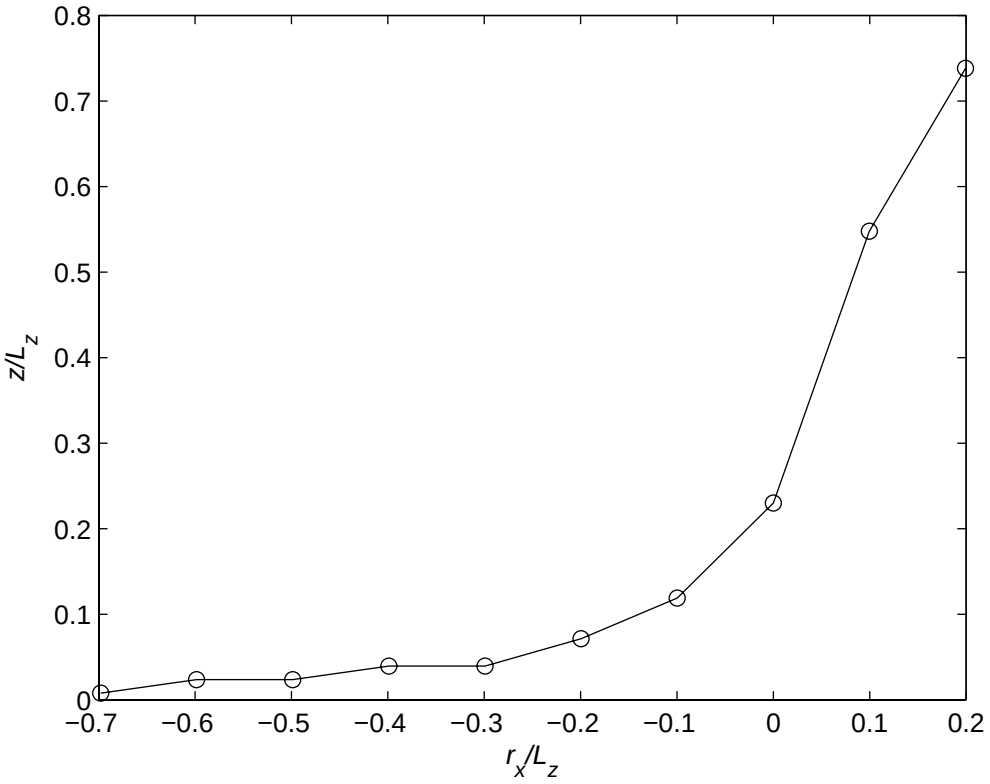

Figure 3.10. Height of zero-crossings of v (at $r_y / L_z = 0.1$) of the $y-z$ slices of $\psi^{(1)}\left(r_x, r_y, z\right)$ versus the streamwise position r_x / L_z for the LES in the entire domain

This trend is quantified in Figure 3.10 for the entire ABL domain, with the heights of the vortex centers identified as the v zero-crossings at $r_y / L_z = 0.1$. The

choice of this cross-wind position is motivated by the fact that in the area close to the centre ($r_y / L_z = 0$) the rotation of the vortex or the global circulation is much stronger than far from the centre. The elevations of the centre of the vortical structure increase rather slowly upstream of $r_x / L_z = -0.3$, with the tilt angle approximately 5° in the range of $r_x / L_z \subset (-0.7, -0.3)$. Downstream of this point, the double rollers begin to climb up dramatically, with the angle increasing to ~ 70°. Although it is difficult to precisely identify the streamwise extent of the coherent structure solely based on Figure 3.10, we can conclude that, it is of the order of L_z. Moin and Moser (1989) obtained comparable values for the streamwise extent and the angle of inclination as those reported for the LES here.

In order to demonstrate the three-dimensionality of coherent structures, the enstrophy of $\psi^{(1)}(r_x, r_y, z)$ of the near wall, denoted here as $\rho = \omega_i \omega_i$, is computed, where ω_i represents the vorticity of $\psi^{(1)}(r_x, r_y, z)$ in the i^{th} direction; and then the isosurface of ρ is plotted in Figure 3.11a. The isovalue is set to 200 times of the spatial average enstrophy. This value has been chosen to adequately visualize the three-dimensional structure. The double roller structure appears as two symmetric inclined cylinders extending along x. There is also an elongated 'tongue' down in the central area, which is mainly due to the vertical gradient of the strong ejection motion. The isosurface of the x component of enstropy $\rho_1 = \omega_1 \omega_1$ is then presented in Figure 3.11b

with the isovalue set as 1000 times of the spatial average, which singles out the double roller structure by neglecting the rotations occurring in the $x-y$ and $x-z$ planes. These results in terms of the geometric information of three-dimensional vortical structures can be related to the classical hairpin structures that are normally seen using the traditional flow visualization techniques. For example, Head and Bandyopadhyay (1981) demonstrated hairpin vortex in the outer region of the boundary layer and concluded that the vortex is inclined at approximately 45° to the wall in the streamwise direction.

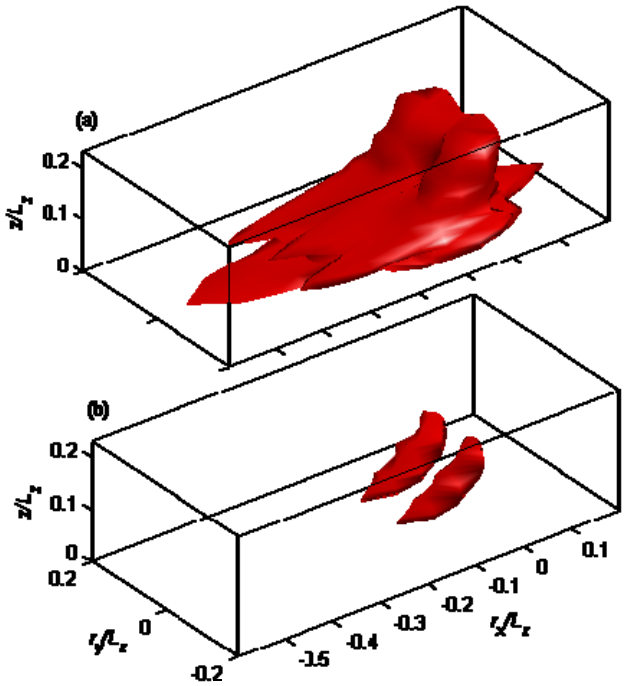

Figure 3.11. (a) Isosurface of enstrophy ρ for the nested grid of the near-wall domain; (b) Isosurface of the x component of ρ (ρ_1) for the nested grid of the near-wall domain. The isovalues are set as (a) 200 (b) 1000 times of the spatial average, respectively

Finally, it is important to note that this study does not simulate the Coriolis force effects, and consequently, the features of coherent structures caused by the Coriolis force should not be expected here. For example, the legs of the hairpin structure turn with height within the ABL when the Coriolis force is taken into account (e.g., Lin et al. 1996); however, they are approximately parallel with the streamwise direction in our work.

3.4 *Truncated Reconstruction*

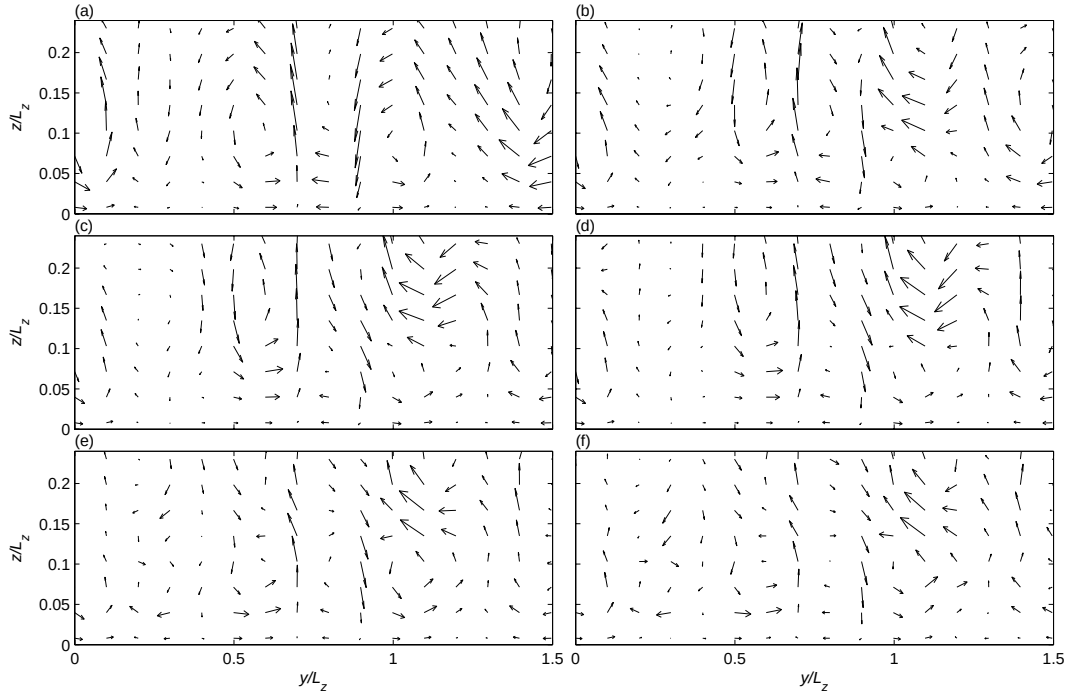

Figure 3.12. Two-dimensional reconstruction for an instantaneous velocity field on the $y-z$ plane with: (a) 1; (b) 2; (c) 3; (d) 4; (e) 10 modes used, respectively; (f) is the original $v-w$ field

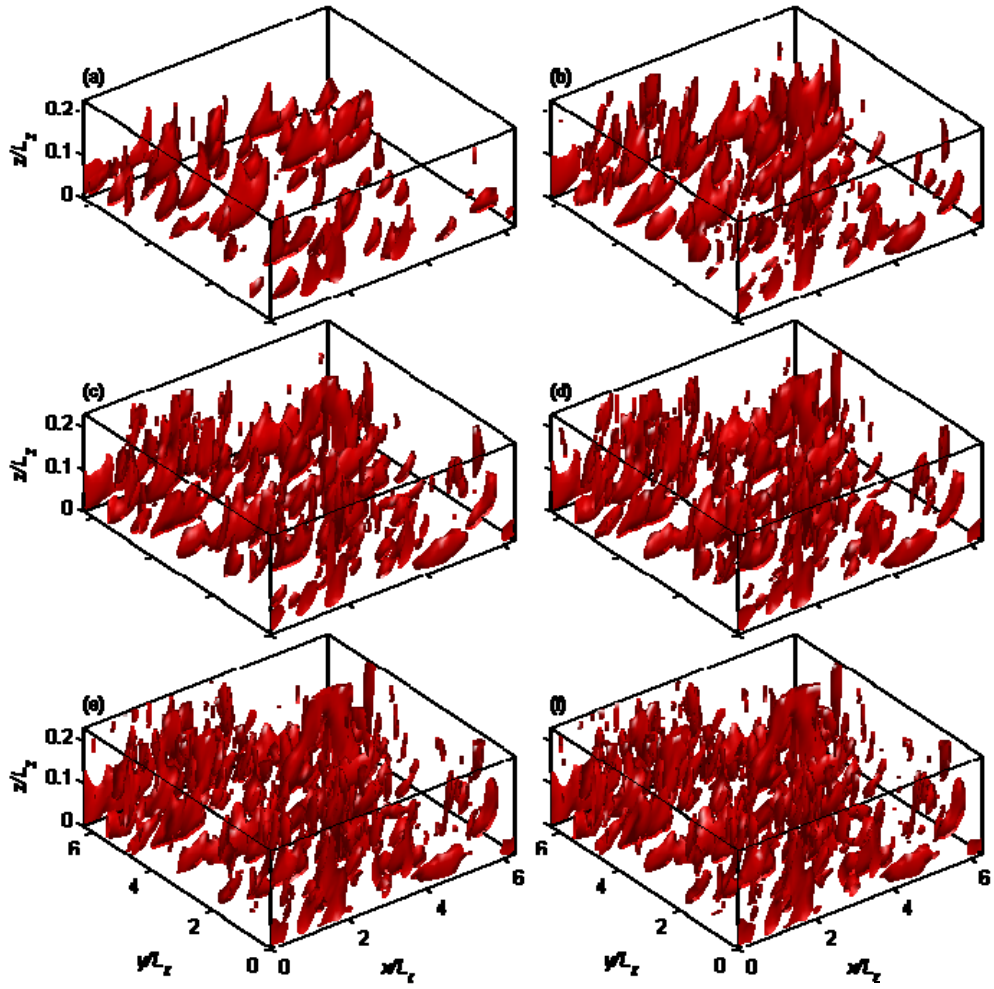

Figure 3.13. Isosurfaces of TKE of a three-dimensional reconstruction for an instantaneous velocity field with: (a) 1; (b) 2; (c) 3; (d) 4; (e) 10 modes used, respectively. (f) is for the original velocity field. The isovalue is set as 3 times of the three-dimensional average

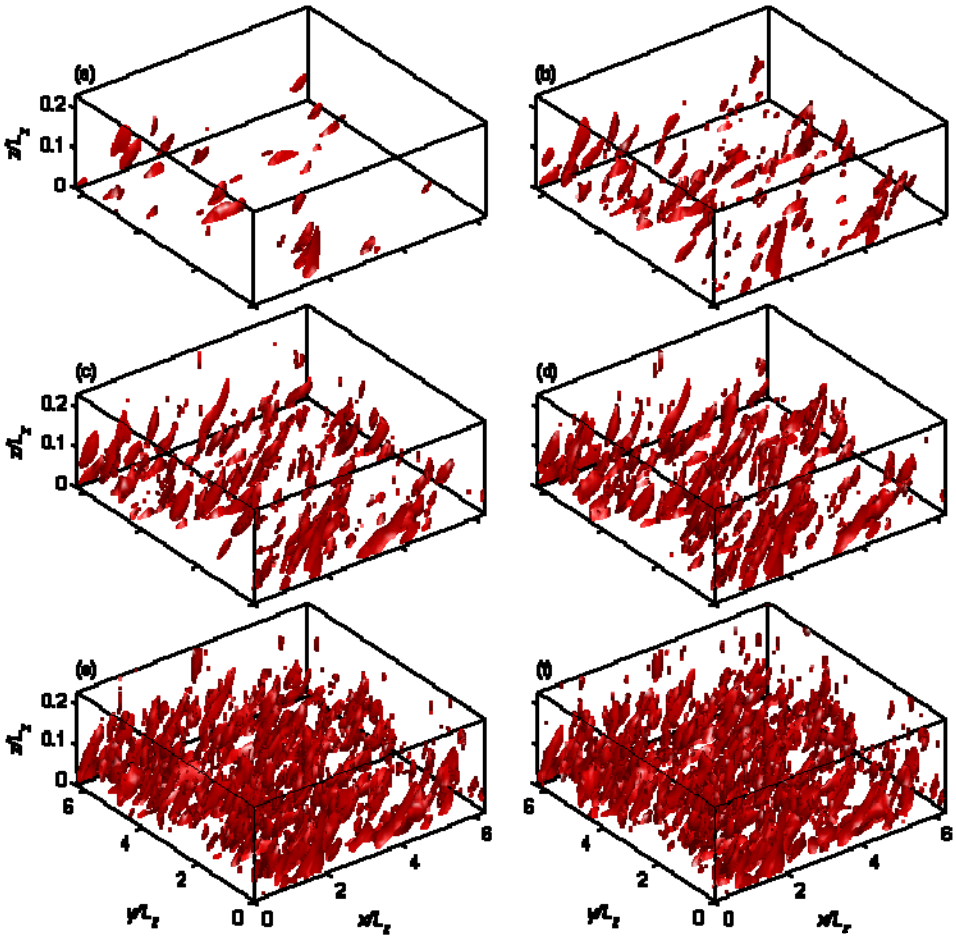

Figure 3.14. Isosurfaces of enstrophy of a three-dimensional reconstruction for an instantaneous velocity field with: (a) 1; (b) 2; (c) 3; (d) 4; (e) 10 modes used, respectively. (f) is for the original velocity field. The isovalue is set as 3 times of the three-dimensional average

Once the important turbulent structures are identified, it is of natural interest to explore the efficiency of these structures in describing the instantaneous turbulent fields. Coefficients $\hat{a}_m\left(k_x, k_y, t\right)$ are multiplied by the corresponding eigenfunctions

$\hat{\phi}_i^{(m)}\left(k_x, k_y, z\right)$ in spectral space and a number of (say p) modes are superimposed to obtain a (p-mode) truncated reconstruction of an instantaneous turbulent velocity field $u_i^p\left(x, y, z, t\right)$ (c.f. equation (2.36)). A formula of two-dimensional reconstruction can be defined similarly. A two dimensional example is showed in Figure 3.12. As more and more modes are superimposed, the reconstruction approaches the original velocity field. The 4- and 10-modes reconstructions are virtually indistinguishable from the original field. Furthermore, we also illustrate the effects of the truncated reconstruction in three-dimensional space by showing the isosurface of the TKE (Figure 3.13) and enstrophy (Figure 3.14). The structures in both figures become closer to the original ones in terms of their shapes and spatial arrangements as more modes are used in the reconstruction process. For the case of the TKE, there is little visible difference between the 4-modes reconstruction and the original field; however, significant differences can be discerned based on the comparison of the 4-modes reconstruction and the original field for the enstrophy. This difference in the efficiency of reconstructing the TKE and the enstrophy originates from the nature of the POD technique, which optimally captures TKE rather than vorticity.

The ability of the POD in reconstructing a similar turbulent field as the original version using only a small fraction of the information of the original field allows us to study the key properties of turbulent flows, such as characteristic time and length scales and intermittency, in a much simpler way, i.e., focusing on the coefficient series

$\hat{a}_m(k_x, k_y, t)$ or $a_m(r_x, r_y, t)$. In fact, Aubry et al. (1988) made use of these coefficient series of the first few energetic modes to reduce the dimensionality of the Navier-Stokes set of equations to a group of nonlinear ordinary differential equations, from which they can then reveal the turbulent dynamics in the wall region of a turbulent boundary layer using the methods of dynamical systems theory.

3.5 *Conclusions*

In this chapter, the POD technique was implemented to identify large-scale coherent structures in one-, two-, and three-dimensions within a high-Reynolds-number ABL from LES and a low-Reynolds-number channel flow from DNS.

Three assumptions were made to determine the geometries of coherent structures as well as their direction of rotation under the framework of the POD: (i) coherent structures are randomly located in homogeneous directions; (ii) coherent structures are spatially compact; (iii) the sweep/ejection dominance of coherent structures is consistent with that of the instantaneous fields in an integrated sense.

Both similarities and differences arise from this comparison. A general consistency of the spatial patterns of coherent structures between the LES ABL and the DNS channel flow is observed. The identified coherent structure was found to be composed of a strong ejection region framed by a pair of counter-rotating vortices in the $y-z$ plane for both the LES and the DNS. This vortex pair inclines in y with a tilt angle of approximately 45°, and curves up in x with the maximum tilt angle around 70°,

which is comparable to 60^{o} obtained for DNS in Moin and Moser (1989). The differences are mainly composed of two aspects. First, the important structures (i.e., the energetic ejections and the vortex pair) are consistently closer to the wall in the LES than in the DNS, if the vertical extent is scaled by the boundary depth L_z for the LES and by half channel width δ for the DNS, respectively. This is logically due to the viscous sublayer being much thicker (in a scaled sense) in the low-Reynolds-number channel flow than in the high-Reynolds-number ABL flow. This thicker viscous sublayer is able to hold these important structures farther from the wall. Second, the eigenvalues of the DNS converge faster than those of the LES, indicating the turbulent structures in the DNS are more organized than in the LES, which is readily attributed to the difference of Reynolds number as well. This comparison demonstrates the ability of LES (with its wall and SGS models) to show realistic coherent structures since all the differences are logically explained in term of the difference in the Reynolds number.

The consistency of the coherent structures between the coarse grid and the nested grid in the LES shows that the nesting technique is able to reveal more detail in small scales of the same turbulent dynamics as the coarse grid while maintaining the same boundary conditions. Since the nested grid resolves smaller scales than the coarse grid and the scale of the dominant structures decreases approaching the wall, the vertical profiles of the second order statistics and the one-dimensional coherent structures $\psi_i^{(1)}(z)$ peak closer to the wall in the nested grid than in the coarse grid.

Another consequence which is likely to be caused by the difference of the number of grid points of the two resolutions is the relatively slower convergence rate of the eigenvalues of the nested grid.

In addition to justifying the use of the LES and the nesting technique in studying the large-scale coherent structures, this chapter also (i) quantitatively showed for the first time that the streamwise vortex pair inclines in the spanwise direction at an angle of approximately 45°; (ii) introduced a simple and robust criterion to determine the direction of rotation of the coherent structures; and (iii) demonstrated the ability of the POD technique in approximating instantaneous turbulent fields with only a few of the most important POD modes $\phi_i^{(n)}(x, y, z)$ and the corresponding coefficients $a_n(x, y, t)$. Using the POD, the TKE can be more efficiently reconstructed than can the enstrophy.

4 The Canopy Sublayer

4.1 *Introduction*

Large-scale coherent structures in the CSL have been under investigation for the past several decades. These organized motions have been shown to be responsible for the majority of mass, momentum and energy transport across the canopy-atmosphere interface (e.g., Gao et al. 1989; Katul et al. 1998; Finnigan and Shaw 2000; Thomas and Foken 2007). Further research indicates that both the geometrical features and the formation mechanism of coherent structures rely on canopy vegetation density (e.g., Novak et al. 2000; Poggi et al. 2004b; Dupont and Brunet 2008b). Since coherent structures play an important role in the canopy-atmosphere interaction and since terrestrial ecosystems cover a very broad range of vegetation densities (Asner et al. 2003), it becomes necessary to understand quantitatively how these large-scale coherent structures change as a function of vegetation density.

The overall behavior of turbulence within the CSL differs significantly from that in the atmospheric surface layer (ASL) (Finnigan 2000) and these differences are characterized by: (1) vertically inflected mean streamwise velocity; (2) rapidly decreasing energy and momentum flux profiles with depth inside the canopy; (3) the important role of large-scale coherent structures on turbulence dynamics through the entire CSL; and (4) domination of sweeps over ejections in vertical momentum transport (Finnigan 2000; Dupont and Brunet 2008b). Raupach et al. (1989, 1996) analyzed

turbulent flows within the CSL and concluded that canopy turbulence behaves much like a plane mixing layer (PML). One of the compelling features is that the ratio of the streamwise separation between adjacent coherent eddies, Λ_x, to the shear length, L_s, matches well the value computed from experiments and numerical simulations in the fully-developed PML (Raupach et al. 1996). Finnigan (2000) described the evolution of the turbulent structures in canopy flows, as being controlled by the Kelvin-Helmholtz instability mechanism, which dominates the formation and evolution of turbulent structures in the PML as well. However, canopy turbulence resembles the PML only in the presence of a homogeneous and 'sufficiently dense' canopy, and this resemblance gradually disappears as the density decreases (e.g., Novak et al. 2000; Poggi et al. 2004b; Dupont and Brunet 2008b). In the extreme case of negligible vegetation, the turbulence appears to resemble a rough-wall boundary layer (e.g., Poggi et al. 2004b). Poggi et al. (2004b) drew on these observations and proposed a phenomenological model for the effective mixing length of coherent structures within the CSL valid for intermediate vegetation densities. This model assumes that near the canopy top the flow field is a superposition of a rough-wall boundary layer and a PML flow. A coefficient (α), which is a function of the vegetation density, was introduced to weight the relative importance of the PML and the boundary layer solutions in affecting turbulent structures in this zone.

In addition to basic flow statistics and characteristic length scales of coherent structures, turbulence investigators have also demonstrated the similarities among turbulent flows within the CSL, the rough-wall boundary layer and the PML in terms of the topological features of the coherent structures as well as their role in describing the TKE. Huang et al. (2009a) examined the large-scale coherent eddies in a large eddy simulation (LES) of the atmospheric boundary layer (ABL) through the use of the proper orthogonal decomposition (POD) technique (Lumley 1967, 1970, 1981). The educed dominant structure (i.e. first eigenmode) was shown to account for over 30 percent of the total TKE in the near-wall domain (vertically extending to approximately 1/5 of the boundary layer depth). Multi-dimensional POD analysis revealed that coherent eddies are comprised of a pair of streamwise counter-rotating vortices framing a strong ejection motion between the vortex pair, which is a major contributor to the vertical momentum transport. The vortices are found to have elliptical cross-sections that are inclined in the span-wise direction and longitudinal alignment that curves upward in the streamwise direction. Similar POD analysis performed on a PML also shows the existence of streamwise vortex pairs and the significance of these structures to the total TKE (Delville et al. 1999). Within the CSL, large-scale coherent structures have been shown to also consist of a pair of counter-rotating streamwise vortices centered above the canopy and represent a large fraction of the total TKE (Finnigan and Shaw 2000). Moreover, between these vortices, there is a weak updraft downstream of a strong sweep.

However, it is still unclear how these characteristic structures depend quantitatively on canopy density.

In this chapter we present results from a series of LES experiments that systematically examines the effects of vegetation density on basic flow statistics as well as on the large-scale coherent structures within the CSL. The POD technique is applied to identify these characteristic structures from the simulated turbulent flow fields. The resulting turbulent structures computed from the LES are compared with those obtained through an analysis of wind-tunnel experimental data. Efforts are also made to quantify the relationship between vegetation density and the extent to which the canopy flow resembles the rough-wall boundary layer and the PML, respectively.

4.2 *Basic Flow Statistics*

Since we will compare our findings of basic flow statistics with prior results obtained from a wind tunnel experiment (Brunet et al. 1994) and a flume experiment (Poggi et al. 2004b) throughout this section, we first introduce the two experiments. In the wind tunnel experiment, elastic cylindrical nylon rods were spaced on a uniform square grid to simulate a horizontally homogeneous canopy with a free stream Reynolds number of 3.40×10^5. The flume experiment used equally spaced steel rods of five different densities in $x-y$ to study the effects of vegetation density on CSL turbulence. The flow Reynolds number varies from 1.71×10^5 to 1.79×10^5. Before comparing the vegetation densities in our LES and the wind tunnel and the flume experiments, the

difference of the definition of the drag force term should be introduced. The drag force in the wind tunnel and flume experiments was defined as $F_i = -\frac{1}{2} C_{d2}(b_2) b_2 Q U_i$ (c.f. equation 12 in Brunet et al. 1994; equation 3 in Poggi et al. 2004b), where $C_{d2}(b_2)$ represents the drag coefficient used and b_2 denotes the elemental area index (EAI, frontal area per unit volume). In consideration of this difference, b_2 can be converted into b as $b = \frac{1}{2} \frac{C_{d2}(b_2)}{C_d} b_2$ (c.f. equation (2.7)). The LAI of the wind tunnel and the flume experiments can be calculated accordingly as $LAI = \frac{1}{2} \frac{C_{d2}(b_2)}{C_d} b_2 h_2$, where h_2 is the height of the rods in the two experiments. We take the relevant parameters from Brunet et al. (1994) and Poggi et al. (2004b), and calculate the effective values for LAD (i.e. b) and LAI (see Table 4-1).

Table 4-1. Original and normalized parameters in wind tunnel and flume experiments

Parameters	h_2 (m)	C_{d2}	EAI (m^{-1})	LAD (m^{-1})	LAI (m^2 m^{-2})
Wind tunnel	0.047	1.35	10	33.75	1.59
Flume	0.12	0.50	0.27	0.34	0.04
		0.61	0.53	0.81	0.10
		0.73	1.07	1.95	0.23
		0.94	2.13	5.02	0.60
		1.15	4.27	12.25	1.47

A series of single point turbulent flow statistics obtained from our simulations is presented in ., and compared with the counterparts in the wind

tunnel and the flume experiments. This comparison serves as the first test of the LES capability to produce realistic dynamics over horizontally homogeneous canopies of different density. The compared statistical variables include: (a) streamwise mean velocity $\langle u \rangle_{xyt}$ scaled by its value at the canopy top ($u_h = \langle u \rangle_{xyt}|_{z=h}$); (b) the total stress τ which is the sum of the resolved stress and the SGS stress the mean stress scaled by the square of the friction velocity $u_*^2 = -\tau|_{z=h}$; (c) streamwise and (d) vertical velocity standard deviations $\sigma_u = \langle u'^2 \rangle_{xyt}^{1/2}$ and $\sigma_w = \langle w'^2 \rangle_{xyt}^{1/2}$ scaled by u_*, respectively; (e) $u - w$ correlation coefficient $r_{uw} = \tau / \sigma_u / \sigma_w$; (f) streamwise and (g) vertical velocity skewness $Sk_u = \langle u'^3 \rangle_{xyt} / \sigma_u^3$ and $Sk_w = \langle w'^3 \rangle_{xyt} / \sigma_w^3$; (h) streamwise and (i) vertical velocity kurtosis $Kr_u = \langle u'^4 \rangle_{xyt} / \sigma_u^4$ and $Kr_w = \langle w'^4 \rangle_{xyt} / \sigma_w^4$.

From Table 4-1 it is clear that the wind tunnel experiment and the densest case of the flume experiments should approximately correspond to the SSC case in the LES, while the sparsest flume experiment should be comparable with the ESC. This speculation can be verified by reference to Figure 4.1.

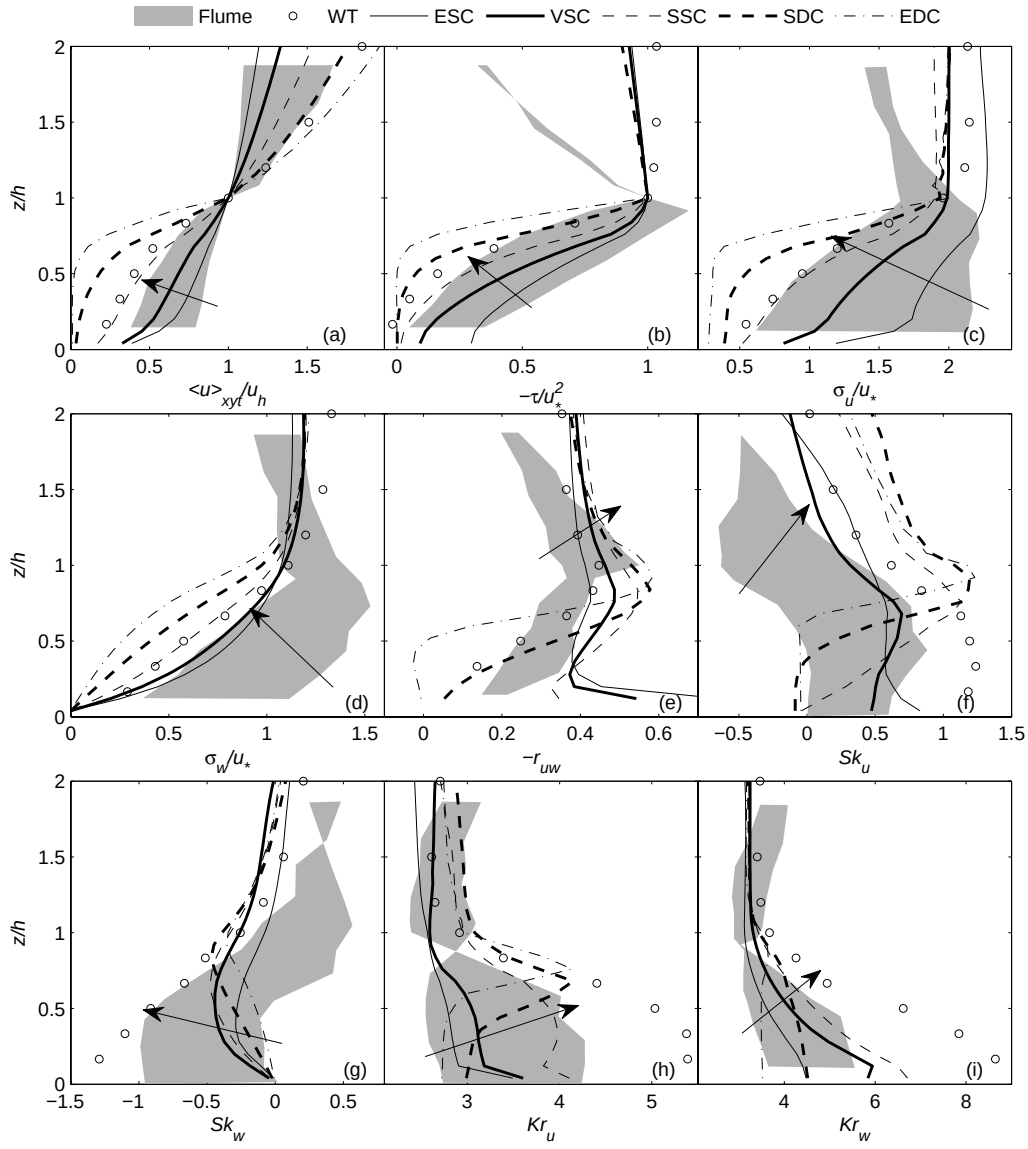

Figure 4.1. Vertical profiles of (a) scaled mean streamwise wind velocity $\langle u \rangle_{xyt} / u_h$; (b) scaled mean shear stress τ / u_*^2 ; (c-d) scaled streamwise velocity (σ_u / u_*) and vertical velocity (σ_w / u_*) standard deviation; (e) uw correlation coefficient r_{uw} ; (f-g) streamwise velocity (Sk_u) and vertical velocity (Sk_w) skewness; (h-i) streamwise velocity (Kr_u) and vertical velocity (Kr_w) kurtosis for LES simulations with varying LAIs, experimental data measured from flume (Poggi et al. 2004b) and wind tunnel (Brunet et al. 1994). The arrows indicate the direction along which rod density increases in the flume experiments

Note that for the flume experiment, the densest canopy case corresponds to the left side of the shaded area inside the canopy for $\langle u \rangle_{xyt} / u_h$, $-\tau / u_*^2$, σ_u / u_*, σ_w / u_* and Sk_w, but the right side for Sk_u, Kr_u and Kr_w. The opposite is true for the sparsest case. Focusing on the region inside the canopy, it can be seen that the LES SSC case, the wind tunnel experiment, and the densest flume experiment all share similar values of $\langle u \rangle_{xyt} / u_h$, $-\tau / u_*^2$, σ_u / u_* and σ_w / u_*; the shaded areas of the flume experiments basically just cover the cases of ESC, VSC and SSC in all flow statistics except σ_w and r_{uw}, which may be due to the fact that σ_u and σ_w are calculated from only the resolved velocity. Close to the ground the amplitudes of the third and fourth order moments of the streamwise and vertical velocities (Sk_u, Sk_w, Kr_u and Kr_w) measured in the wind tunnel are greater than those of the LES and flume experiments. This is probably caused by the so-called 'honami' wave in the wind tunnel experiment, which occurs only in canopies with elastic rods, such as wheat and corn canopies, and is referred to as the coherent waving motion of groups of rods triggered as some gust travels through the canopy (Finnigan 1979b, a). Since the flume experiment utilized rigid steel rods and this type of elasticity is not simulated in the LES, the 'honami' wave can not be produced in these two cases. This inference is evidenced from inspection of the statistics reported in Raupach et al. (1996) (c.f. Figure 1 therein), which also shows that the amplitudes of Sk_u and Sk_w are significantly greater (up to 100%) for waving canopies than most of non-

waving canopies close to the ground. Above the canopy top, the profiles vary significantly between the flume and the LES/wind tunnel. This is likely caused by the smaller ratio between the boundary layer depth L_z and the rod height h in the flume than in the LES/wind tunnel.

Table 4-2. Comparison of statistical flow properties between surface layer, CSL of various LAIs and mixing layer. Values of surface layer and mixing layer are taken from Finnigan (2000)

Property		⟨u⟩ inflection	σ_u / u_*	σ_w / u_*	$-r_{uw}$	$\lvert Sk_u \rvert$	$\lvert Sk_w \rvert$
ASL		No	2.5-3.0	1.2-1.3	~0.3	Small	Small
	ESC	No	2.3	1.1	0.41	0.39	0.07
LES	CSC	Yes	2.0	1.1	0.46	0.33	0.25
CSL	SSC	Yes	1.9	1.0	0.50	0.78	0.34
(z=h)	SDC	Yes	1.9	1.0	0.53	1.20	0.39
	EDC	Yes	1.9	0.9	0.57	1.15	0.34
PML		Yes	1.8	1.4	~0.4	O(1)	O(1)

A number of noteworthy features emerge as we focus on the effects of vegetation density on flow statistics. As the canopy becomes denser, (1) the inflection of $\langle u \rangle_{xyt} / u_h$ at $z = h$ becomes stronger; (2) the shear stress and the velocity variances are damped more rapidly with increasing depth inside canopy; (3) $\lvert r_{uw} \rvert$ increases in the vicinity of canopy top, which implies that a denser canopy is able to transport momentum more efficiently than a sparse canopy across the canopy-atmosphere interface; (4) $\lvert Sk_u \rvert$, $\lvert Sk_w \rvert$, $\lvert Kr_u \rvert$ and $\lvert Kr_w \rvert$ tend to increase around the treetop with Sk_u, Kr_u and Kr_w being positive and Sk_w negative. This can be interpreted as denser canopies producing more

and stronger sweep events than sparse canopies. These tendencies can be clearly observed as the values of relevant statistics of the five simulated cases are aggregated, and compared with the standard values of these statistics for an ASL and a PML taken from Finnigan (2000) in Table 4-2. Note that r_{uw} of canopy turbulence is noticeably greater than that of the ASL and the PML. A possible explanation for this discrepancy is provided in Chapter 4.3. This comparison basically demonstrates that the overall behavior of the CSL with sparse canopies (e.g., ESC) tends to resemble that of an ASL, and as the canopy becomes denser, it changes gradually to be similar with a PML.

Overall, the comparison between our LES and the flume/wind tunnel experiments demonstrates that our LES successfully produces basic flow statistics of canopy turbulence. Before investigating the effects of the LAI values on the geometric features of the large-scale coherent structures, it is necessary to examine the dependence of characteristic length scales, such as integral length scales and mixing length, which are fundamental properties of the coherent structures, on vegetation density.

4.3 *Characteristic Length Scales*

The study of length scales is a first step toward understanding the spatial arrangement and size of turbulent structures. In a horizontally homogeneous stationary flow, the two-point space-time correlation tensor between an arbitrary reference location (x, y, z, t) and another location $(x + \Delta x, y + \Delta y, \tilde{z}, t + \Delta t)$ can be written as:

$$r_{ij}\left(\Delta x,\Delta y,\Delta t,z,\tilde{z}\right)=\frac{\left\langle u_i'\left(x,y,z,t\right)u_j'\left(x+\Delta x,y+\Delta y,\tilde{z},t+\Delta t\right)\right\rangle_{xyt}}{\left\langle u_i'^2\left(x,y,z,t\right)\right\rangle_{xyt}^{1/2}\left\langle u_j'^2\left(x,y,\tilde{z},t\right)\right\rangle_{xyt}^{1/2}}. \tag{4.1}$$

The two-point integral length scales can be obtained by integrating the correlation tensor of zero delay in *y*, *z* and *t* over Δx:

$$L_i\left(z\right)=\int_0^\infty r_{ii}\left(\Delta x,0,0,z,z\right)d\Delta x\,, \tag{4.2}$$

where no summation is implied on the repeated index ii. The streamwise integral length scale L_1 and the vertical integral length scale L_3 are plotted in Figure 4.2a and b for canopies of five densities, respectively.

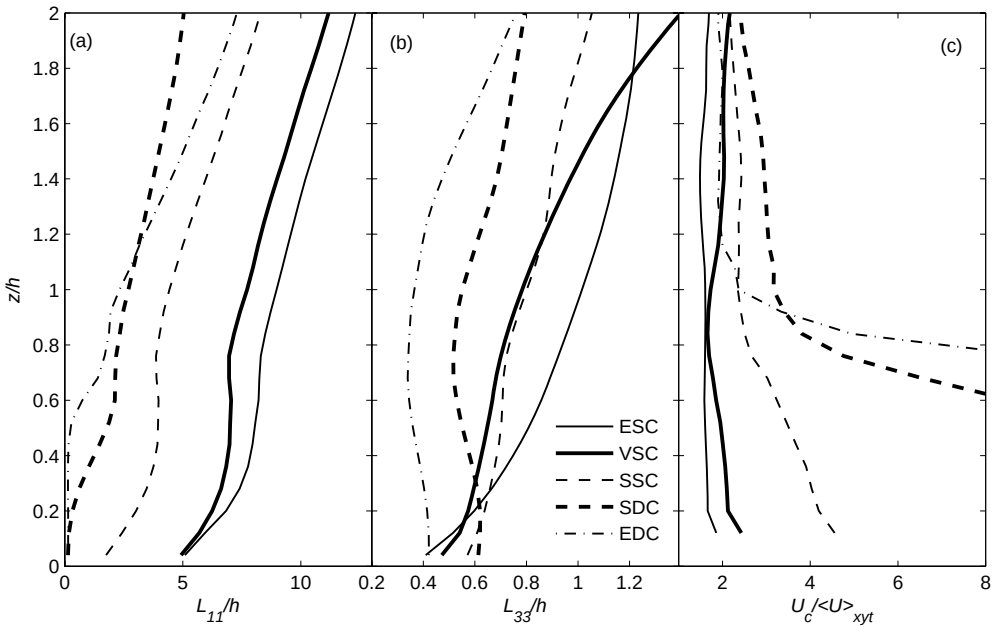

Figure 4.2. Vertical profiles of two-point length scales normalized by *h* (L_{11}/h and L_{33}/h) and the convection velocity U_c scaled by $\langle U\rangle_{xyt}$ for canopies of five LAIs

Shaw et al. (1995) performed the analysis of two-point velocity statistics on the same experimental dataset as in Brunet et al. (1994) and demonstrated that at the canopy top L_1 is ~ $2.8h$ while L_3 is ~ $0.6h$. In the LES we obtain $L_1 \approx 4.4h$, $L_3 \approx 0.8h$ for SSC, and $L_1 \approx 2.7h$, $L_3 \approx 0.55h$ for SDC, which are in good agreement with the wind tunnel analysis because both the LAI value and the results of L_1 and L_3 in the wind tunnel experiment are bounded by those of the SSC and the SDC. In addition to this agreement, three trends can be clearly observed. First, L_i tends to decrease as the vegetation density increases with local exceptions. Since L_i is a measure of the streamwise distance over which turbulent signals become uncorrelated and is known to be proportional to the streamwise separation of coherent structures (Raupach et al. 1996), this tendency reflects that dominant motions within the CSL of denser canopies are positioned closer to each other in the streamwise direction. At the canopy top, L_1 ranges from approximately $2h$ for EDC to $9h$ for ESC, and L_3 from around $0.4h$ for EDC to h for ESC. Second, integral length scales generally increase as it goes farther from the ground. Third, L_3 behaves differently from L_1 in the fashion that it is less sensitive to changes of both LAI and z.

We can calculate the convection velocity u_c, which describes the rate at which the coherent structures are convected along x (Shaw et al. 1995):

$$u_c(z) \Big/ \langle u \rangle_{xyt}(z) = L_i(z) / l_i(z), \tag{4.3}$$

where l_i is the traditional single-point integral length scale calculated from u_i (see e.g. Raupach et al. 1996). The ratio $u_c/\langle u\rangle_{xyt}$ is a measure of the extent to which the investigated flow obeys or disobeys Taylor's hypothesis: the closer the ratio $u_c/\langle u\rangle_{xyt}$ is to 1, the better the turbulence obeys this hypothesis. Here $u_c/\langle u\rangle_{xyt}$ is calculated as L_3/l_3, because the vertical velocity represents the active turbulence while the streamwise velocity is 'contaminated' by the inactive turbulence (see e.g., Katul et al. 1996b), and is plotted in Figure 4.2c. Although the time step Δt is not constant in an absolute sense due to the numerical scheme of temporal integration adopted in the LES, the ratio between the standard deviation and the mean value $\sigma_{\Delta t}/\langle \Delta t\rangle$ is below 9 percent for all five cases. The normalized convection velocity $u_c/\langle u\rangle_{xyt}$ generally increases as the canopy becomes denser except the case of EDC above $z/h \approx 0.9$. At $z = h$, $u_c/\langle u\rangle_{xyt}$ varies from ~1.6 for ESC to ~3.2 for SDC. Inside the canopy, $u_c/\langle u\rangle_{xyt}$ tends to increase as it goes closer to the ground, and this tendency is intensified as the canopy becomes denser. Overall, Taylor's hypothesis is demonstrated to be significantly violated within the CSL and the extent of violation increases as the vegetation density increases and it goes closer to the ground.

Another important length scale is the shear length, which is defined as $L_s = u_h/\left(d\langle u\rangle_{xyt}/dz\right)_{z=h}$. Raupach et al. (1996) predicted that if the canopy turbulence

can be modelled as a PML, a theoretical relationship should exist between the mean streamwise separation of the coherent structures, Λ_x, and L_s, i.e., $\Lambda_x/L_s \subset (7,\ 10)$. This prediction was further verified in Raupach et al. (1996) by examining a number of field and wind tunnel experiments: the ratio Λ_x/L_s was found to be approximately 8.1 and insensitive to LAI, which serves as a strong evidence supporting the mixing-layer analogy for the CSL.

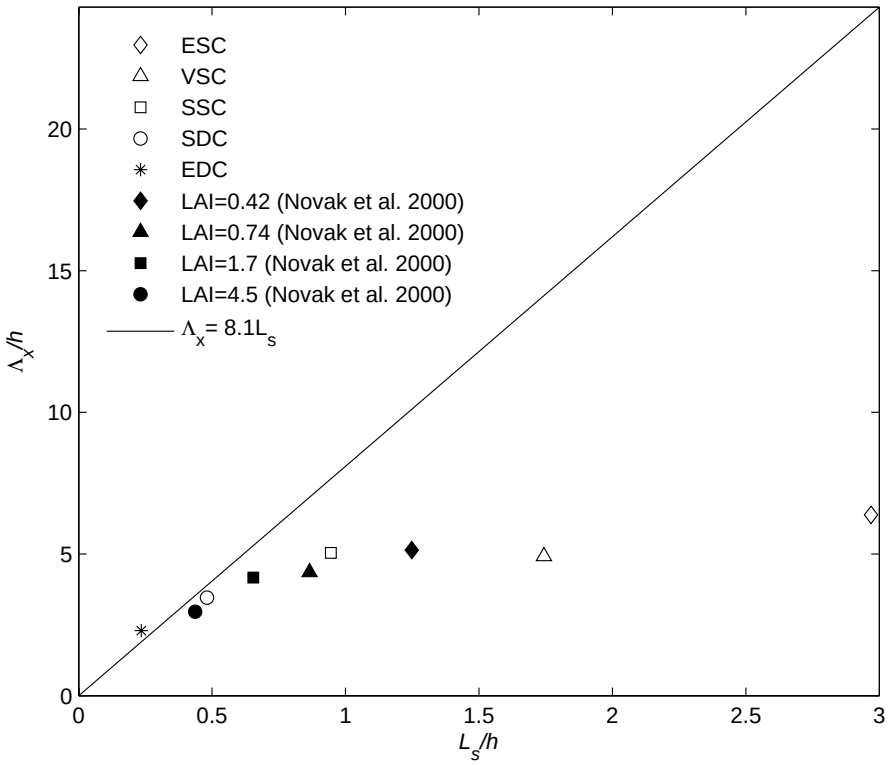

Figure 4.3. Mean streamwise separation Λ_x of coherent structures at canopy top versus shear length scale L_s for canopies of five LAIs. Both axes are scaled by the canopy height h. The wind tunnel results of Novak et al. (2000) are plotted for reference. The straight line is predicted by Raupach et al. (1996) using a number of field experiment data

In order to explore the extent to which this analogy is affected by variations of vegetation density, we calculated Λ_x / L_s for the LES runs of five LAIs. Following Raupach et al. (1996) we estimate Λ_x as $2\pi L_3$, where the factor 2π relates the correlation length of $w(x)$ to the streamwise separation length of adjacent coherent structures. The results are showed in Figure 4.3, where it can be clearly seen that SDC and EDC match the straight line of $\Lambda_x / L_s = 8.1$ quite well while the other three cases deviate farther from this line with Λ_x becoming independent of L_s as the canopy becomes sparser. This suggests that the mixing-layer analogy is applicable only to sufficiently dense canopies with the critical minimum LAI value between 1 and 4.

Given that the canopy turbulence with relatively small vegetation densities (say LAI < 1) can not be modeled as a pure PML, Poggi et al. (2004b) argued that it is affected by the potential mechanism of a rough-wall boundary-layer as well. They proposed a linear superposition model to compute the effective mixing length of the CSL with the relative importance of the PML mechanism to the boundary-layer mechanism depending on vegetation densities. Instead of modeling the mixing length within the CSL empirically, here we propose a theory for the estimation of the mixing length of canopy turbulence without introduction of empirical parameters. This theory assumes that the mixing effects of both turbulence sources add up, which is approached through the traditional gradient transport theory. For a pure rough wall boundary layer, the gradient transport theory can be applied to the vertical transport of momentum as:

$$\langle u'w' \rangle = -K_{BL} \frac{d\langle u \rangle}{dz}, \tag{4.4}$$

where K_{BL} is the eddy diffusivity for the boundary layer. Similarly for a pure PML, we have:

$$\langle u'w' \rangle = -K_{ML} \frac{d\langle u \rangle}{dz}, \tag{4.5}$$

where K_{ML} is the eddy diffusivity for the PML. Since both turbulence sources exist in the CSL, the eddy diffusivity of the CSL K_{CSL} should be modeled as the sum of K_{BL} and K_{ML}:

$$\langle u'w' \rangle = -K_{CSL} \frac{d\langle u \rangle}{dz} = -(K_{BL} + K_{ML}) \frac{d\langle u \rangle}{dz}. \tag{4.6}$$

Using the Prandtl's mixing length theory the eddy diffusivities can be expressed as a function of the effective mixing length, i.e.,

$$K_{BL} = l_{BL}^2 \left| \frac{d\langle u \rangle}{dz} \right|, . \tag{4.7}$$

$$K_{ML} = l_{ML}^2 \left| \frac{d\langle u \rangle}{dz} \right|, . \tag{4.8}$$

and

$$K_{CSL} = l_{CSL}^2 \left| \frac{d\langle u \rangle}{dz} \right|. \tag{4.9}$$

Substituting equation (4.7), (4.8) and (4.9) into equation (4.6) l_{CSL} can then be calculated as:

$$l_{CSL}^2 = l_{BL}^2 + l_{ML}^2 . \tag{4.10}$$

In equation (4.10) the actual value of l_{CSL} can be obtained from the vertical profiles of $\langle u'w' \rangle$ and $\langle u \rangle$ by combining equation (4.6) and (4.9). We use l_{sup} to denote the modeled value of l_{CSL} (i.e. $\left(l_{BL}^2 + l_{ML}^2\right)^{1/2}$) while using l_{CSL} to represent the actual value:

$$l_{CSL}(z) = \left| \langle u'w' \rangle \Big/ \left(d\langle u \rangle / dz \right)^2 \right|^{1/2} . \tag{4.11}$$

l_{BL} is provided by the Monin-Obukhov similarity theory as

$$l_{BL}(z) = k(z - d), \tag{4.12}$$

where k is the von Karman constant and d is the zero plane displacement height calculated as

$$d = \frac{\int_0^h z f_1(z) dz}{\int_0^h f_1(z) dz} . \tag{4.13}$$

We now seek a formula for l_{ML}. A CSL is analogized as a PML under the assumption of a vertically symmetric mean streamwise velocity profile with respect to the horizontal plane of the canopy top. Provided that the mean streamwise velocity at the canopy top is u_h and the low speed free stream velocity is 0, the high speed free stream velocity is $2u_h$. Consequently, L_s can be connected to the vorticity thickness of the PML (δ_ω) as $\delta_\omega = 2L_s$.

A popular expression for the mean streamwise velocity in the PML is an error function in the form of:

$$\frac{\langle u \rangle(z)}{u_h} = 1 + erf\left(\frac{\sqrt{\pi}}{2}\frac{z-h}{L_s}\right). \tag{4.14}$$

According to the direct numerical simulation (DNS) results with the thickness Reynolds number reaching 2×10^4 in Rogers and Moser (1994), the Reynolds stress profile can be fitted as the following function:

$$\frac{\tau(z)}{u_h^2} = -0.04\exp\left\{-\left(\frac{z-h}{L_s}\right)^2\right\}. \tag{4.15}$$

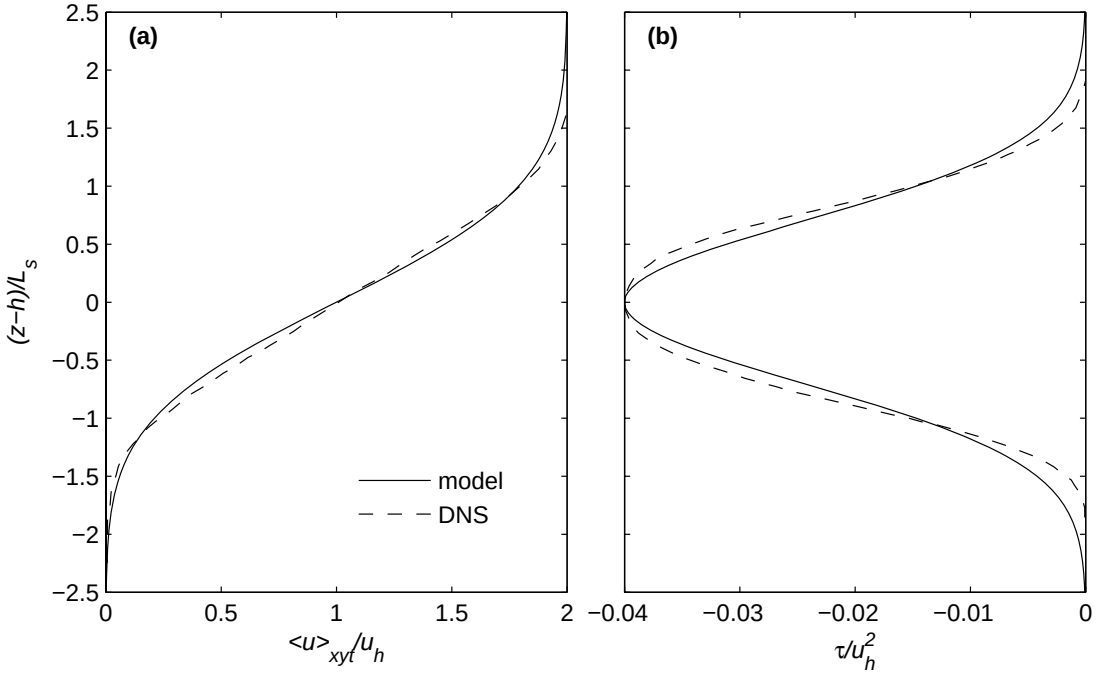

Figure 4.4. Comparison between our models (Equation (22) for (a) and Equation (23) for (b)) and the DNS results in Rogers and Moser (1994) for (a) the mean streamwise velocity profile and (b) the Reynolds stress profile of the PML

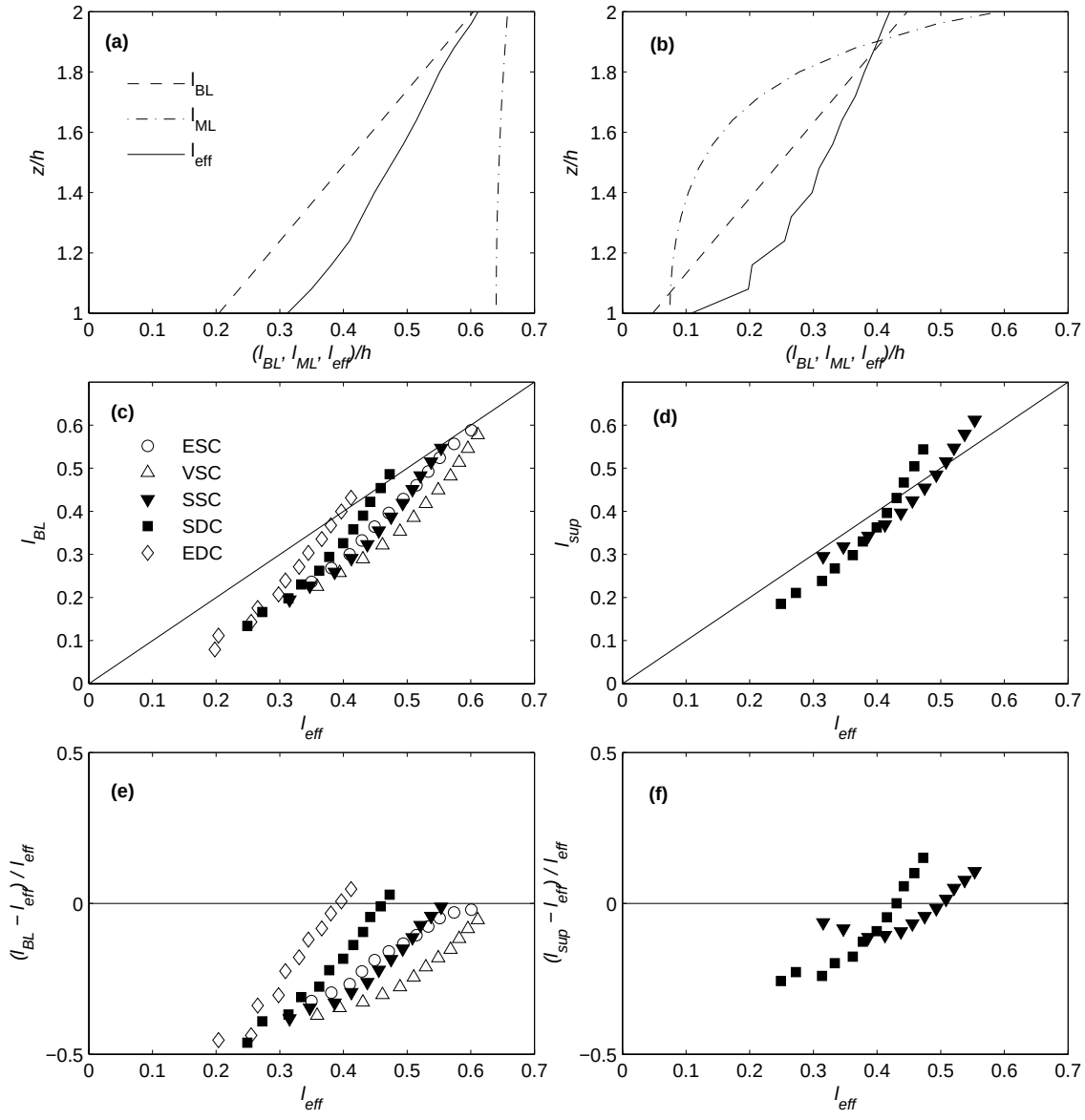

Figure 4.5. The effective mixing length of the CSL l_{eff}, of the rough-wall boundary layer model l_{BL} and of the PML model l_{ML} for (a) ESC and (b) EDC; (c) l_{BL} versus l_{eff} for all the five LAI cases; (d) l_{sup} versus l_{eff} for SSC and SDC; (e) the measure of the performance of the rough-wall boundary layer model $(l_{BL} - l_{eff})/l_{eff}$ for all the five LAI cases; (f) the measure of the performance of the superposed eddy diffusivity model $(l_{sup} - l_{eff})/l_{eff}$ for SSC and SDC

Figure 4.4 demonstrates the comparison of the mean streamwise velocity profile and the Reynolds stress profile between the DNS results in Rogers and Moser (1994) and the prediction using equation (4.14) and (4.15). Following Rogers and Moser (1994), the momentum thickness δ_m is converted to the vorticity thickness δ_ω as $\delta_m = \delta_\omega / 4.44$. Substituting (4.14) and (4.15) into (4.5) and (4.8), we obtain the formula of the mixing length of the PML as:

$$l_{ML}(z) = 0.2 L_s \exp\left\{ \frac{\pi - 2}{4} \left(\frac{z-h}{L_s} \right)^2 \right\}. \tag{4.16}$$

Figure 4.5a and b show the vertical profiles of l_{BL}, l_{ML} and l_{eff} in the vertical region $z/h \subset [1.0, 2.0]$ for ESC and EDC, respectively. For the ESC case, l_{eff} falls between l_{BL} and l_{ML}, but close to l_{BL}. As we focus on the VDC case, l_{eff} becomes greater than both l_{BL} and l_{ML} in most of the shown vertical range. An examination of the other three cases reveals that the same trend exists for VSC, SSC and SDC as well. It can be seen clearly in Figure 4.5c that l_{BL} tends to systematically underestimate l_{eff}. Figure 4.5d shows l_{sup} for the cases of intermediate canopy densities (SSC and SDC), where the underestimation has been corrected in l_{sup}. To further quantify the performance of the pure rough wall boundary layer model and the eddy diffusivity superposition model, the relative errors of the two models have been calculated and shown in Figure 4.5e and f, respectively. The relative error of the pure rough wall boundary layer model, $(l_{BL} - l_{eff})/l_{eff}$, is mostly negative for all the five LAI cases with the minimum ≈ –0.5. The amplitude of this value decreases as l_{eff}

increases, implying that this model performs better as it departs farther from the canopy. As far as the eddy diffusivity superposition model is concerned, its relative error ranges between ≈–0.25 to ≈0.15 for SSC and SDC. The general consistency between l_{sup} and l_{eff} also explains why canopy turbulence is able to transport vertical momentum more efficiently than both the ASL and the PML, as suggested by the r_{uw} values in Table 4-2.

4.4 *One-Dimensional Analysis*

Finnigan and Shaw (2000) analyzed the same dataset as in Brunet et al. (1994) and revealed the geometries of coherent structures based on one- and two-dimensional POD analyses. The first three one-dimensional POD modes of SSC are compared with those in Finnigan and Shaw (2000) in Figure 4.6 since the adjusted LAI of the wind tunnel experiment (LAI=1.59) is closest to that of SSC (LAI=1). In order to make our results comparable with Finnigan and Shaw (2000), we perform one POD analysis jointly for u and w, and another separate one for only v. All the modes of the wind tunnel results are non-dimensionalized by the friction velocity ($u_*^{WT} = 0.87$ m s^{-1}) as for the LES by $u_* = 0.3$ m s^{-1}. The general patterns of the one-dimensional eigenmodes from both studies are in a good agreement, which appears as: (1) the same trend of relative signs of u and w modes; (2) similar amplitudes in all six comparisons of eigenmodes; (3) similar elevations of zero-crossings. This comparison demonstrates that our LES is able to produce similar canopy turbulence structures as in wind tunnel experiments with vegetation of similar density values.

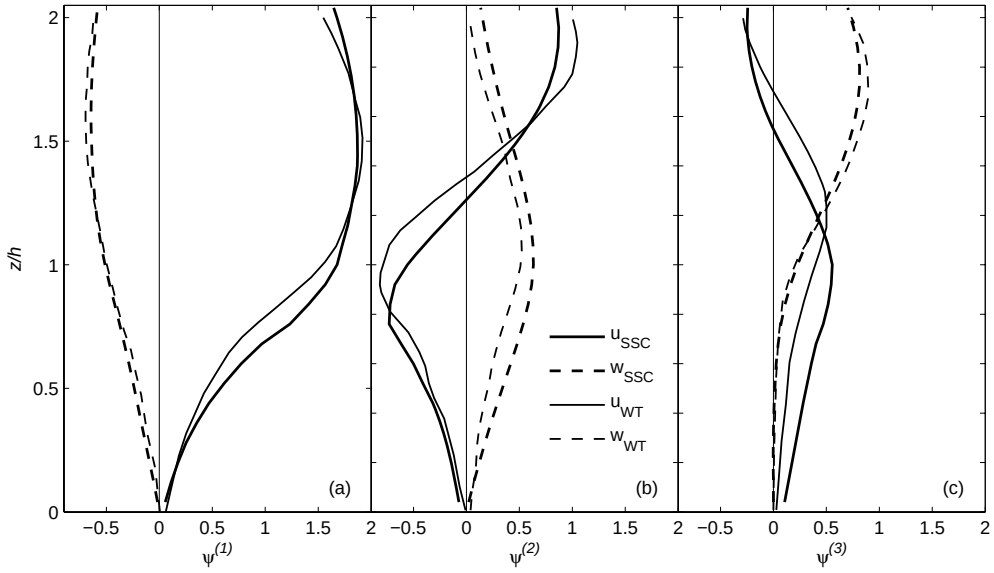

Figure 4.6. Comparison of the first three one-dimensional eigenmodes $\psi^{(i)}$ between the SSC in the LES and the wind tunnel experiment

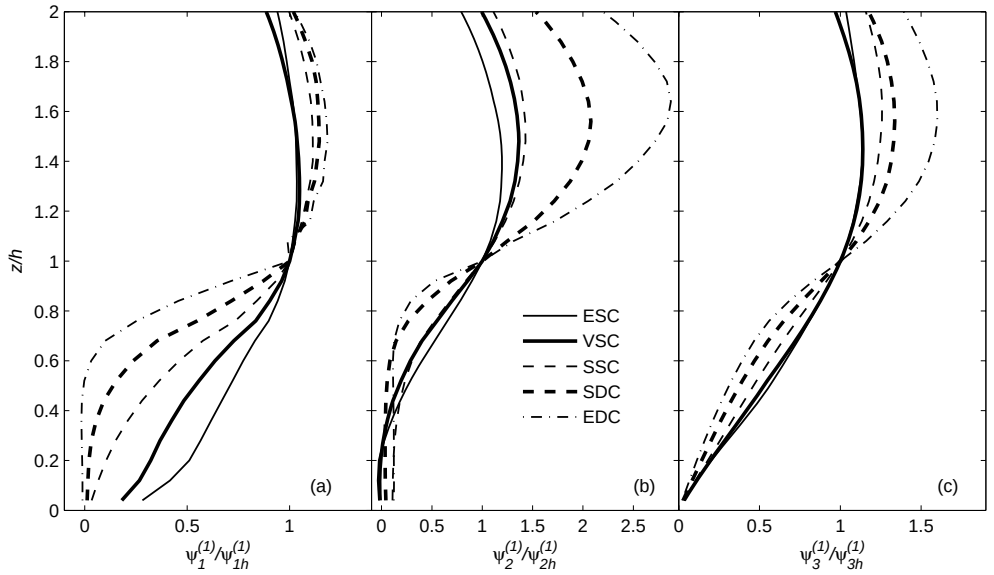

Figure 4.7. Comparison of the first one-dimensional eigenmodes of (a) u; (b) v; and (c) w for canopies of five different LAIs

We explore the effects of canopy vegetation density on the one-dimensional energetic structures in Figure 4.7. The eigenmodes for the five different cases in the LES are normalized by their values at $z = h$, as $\psi_i^{(1)} / \psi_{ih}^{(1)}$. Similar with the mean streamwise velocity profile, the structures of denser canopies have stronger inflection for all cases with the u structure showing a more pronounced change of curvature inside the canopy and the v structure above the canopy.

In addition to the geometrical features in z, we are also interested in studying the relative importance of each individual eigenmode and the effects of vegetation density on it. For this purpose we focus on the convergence rate of the eigenvalue series $\lambda^{(m)}$, which measures how efficiently the POD concentrates the TKE into the leading mode. The cumulative contributions of all the eigenmodes to the total energy of $\left\langle u'^2 + w'^2 \right\rangle_{xyt}$ have been computed for all the LAI cases. It is found that the LAI does not have a significant influence on convergence rates. In the wind tunnel experiment (Finnigan and Shaw 2000), the first mode accounts for approximately 53 percent of the total TKE and the first five modes capture up to 82 percent of the total TKE; similarly, in our LES results, the percentage of the first mode ranges from 54 percent (VSC) to 61 percent (ESC), and the first five modes between 85 percent (VSC) to 89 percent (EDC).

4.5 *Multi-Dimensional Analysis*

The one-dimensional POD analysis reveals the structural features of the coherent eddies only in the vertical direction. In this section the POD analysis is extended to

multi-dimensions to explore the structural features in the spanwise direction as well as in the streamwise direction.

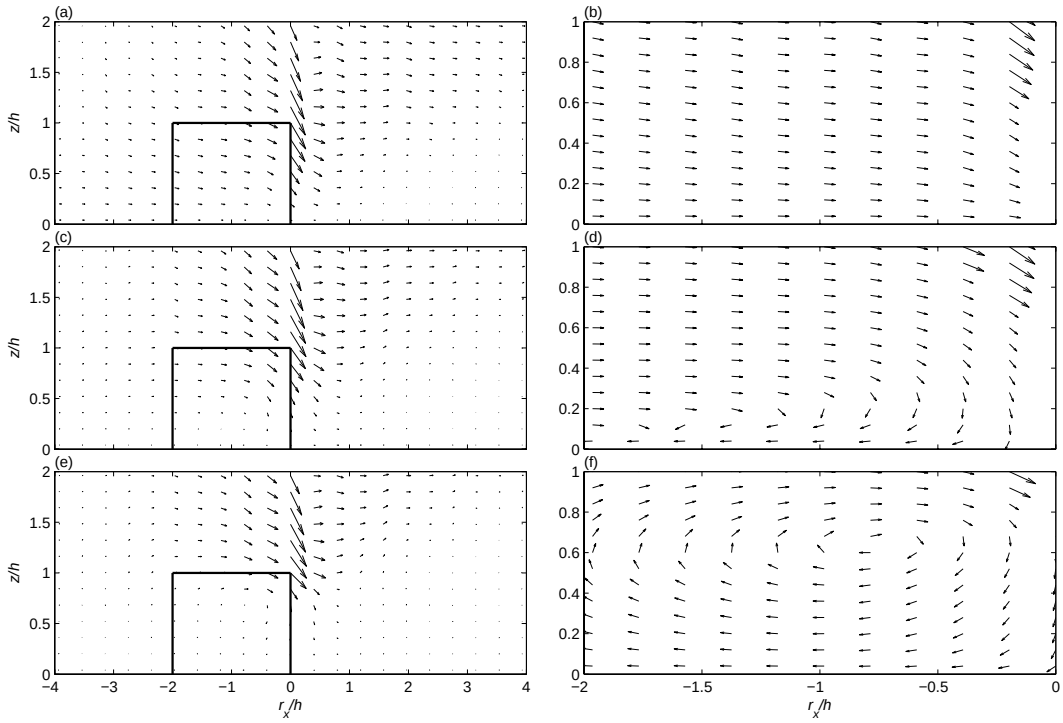

Figure 4.8. u – w vector plot of the two-dimensional turbulent structure in the x – z plane for (a) ESC, (c) SSC and (e) EDC. (b,d,f) are the zoom-in and magnified version corresponding to the framed areas on the left side

We first conduct two-dimensional analysis in the x – z plane. Prior field and laboratory experiments have painted a consistent picture of turbulent structures in the CSL in the x – z plane (e.g., Gao et al. 1989; Gardiner 1994; Finnigan and Shaw 2000). The picture is one of intermittent occurrences of strong sweep motions and relatively weak ejection events with ejections becoming more dominant with height. Each right panel in Figure 4.8 is the magnified version of the framed area in its corresponding left panel. The most noticeable feature is the dominance of strong sweep motions.

Vertically, the strength of sweep motions peaks in the range of $z/h \subset [1,\ 1.5]$ and decreases gradually above, which agrees well with available findings (Finnigan and Shaw 2000). The main effect of vegetation density on this two-dimensional structure is the rise of the energetic sweep motions as the canopy becomes denser, and consequently, the lower and middle levels of the canopy are filled by relatively weak circulating flows. There is an interesting pattern hidden inside the canopy ranging from $r_x/h = -2h$ to $r_x/h = 0$. What we see for the ESC case is a broad and weak sweep; but for SSC a clockwise-rotating vortex emerges with its centre approximately positioned at $z/h = 0.2$. As we focus on EDC, the centre of this vortex moves upward and forward to $(r_x/h,\ z/h) \approx (-0.8,\ 0.65)$. It is clear that whether and where this type of vortex is formed relates to the canopy density: the vortex is not formed in the cases of ESC and VSC; however, as the canopy grows denser from SSC to EDC, the vortex is formed and its centre approaches closer to the canopy top. This type of vortex was not found in the two-dimensional analysis of the wind tunnel experiment (c.f. Figure 9 in Finnigan and Shaw 2000), which is possibly due to the insufficient vertical sampling resolution in the measurement procedure. It is unclear at this point whether this type of span-wise vortex is generated by the Kelvin-Helmholtz instability, but it is noted that the centre positions of vortices in Figure 4.8 are not coincident with the elevation of the occurrence of the inflection point. This type of structure can be discerned in previous field studies (c.f. Figure 5-6 in Gao et al. 1989).

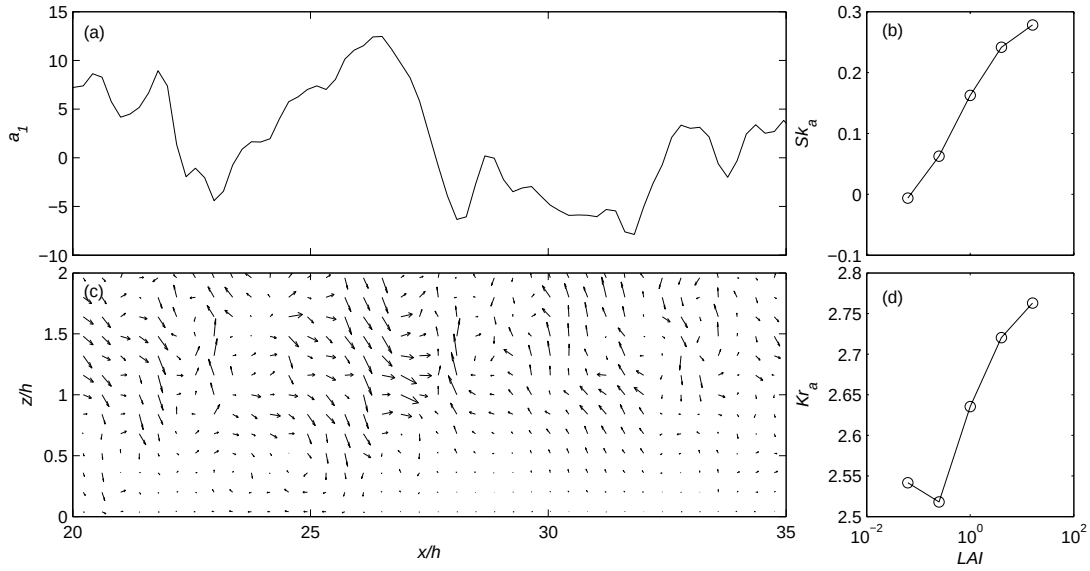

Figure 4.9. (a) A sample of the coefficients of the two-dimensional coherent structures in the $x-z$ plane a_1 for SSC; (c) the corresponding $u-w$ vector plot of the instantaneous turbulent velocity field to the coefficients in (a); (b) the mean skewness of a_1 versus LAI; (d) the mean kurtosis of a_1 versus LAI

Finnigan and Shaw (2000) demonstrated that there is a very weak updraft or ejection around $r_x/h = 5$ following the strong sweeps in the two-dimensional coherent structure in the $x-z$ plane. However, it should be noted that the intermittent occurrence of the sweep/ejection motions is reflected in the sign of the coefficients a_1 rather than in the coherent structure itself. Figure 4.9a and c show a_1 and the $u-w$ vector plot of the corresponding instantaneous turbulent velocity field, respectively. Given that the most energetic component of the instantaneous field (i.e., the truncated reconstruction with only the first eigenmode) is a convolution of a_1 and the coherent structures (see e.g. Moin and Moser 1989; Huang et al. 2009a), it makes sense that a

positive a_1 with a large amplitude (e.g., $x/h \approx 26.5$) corresponds to a strong sweep motion while a negative a_1 with a large amplitude (e.g., $x/h \approx 31.8$) occurs at the same x position as a strong ejection motion. Figure 4.9b and d plot the mean skewness Sk_a and kurtosis Kr_a of a_1 against LAI, respectively. For ESC, $Sk_a \approx -0.006$, which suggests that the ejection motion slightly dominates over the sweep motion. However, as the canopy density increases, Sk_a turns to positive and increases, which demonstrates clearly how the sweep motion begins to dominate and the extent of dominance grows from SSC to EDC. As far as the kurtosis is concerned, it slightly decreases from VSC to SSC as the canopy experiences a transition of the sweep/ejection dominance, and then increases as the canopy becomes denser. This implies that the denser canopy has a higher probability to generate exceptionally strong sweep or ejection events as long as the sweep motion dominates. Overall, the above results, in terms of the sweep/ejection motions are consistent with the prior results that the vegetation density increases the extent of the sweep dominance within the CSL (Novak et al. 2000; Poggi et al. 2004b). In addition to this consistency, this analysis has demonstrated as well that the coherent structures extracted by the POD technique contains only the geometry information, while other aspects of the coherent structures, such as the strength, the sign of the velocity components and the role played in the dynamics of canopy turbulence, remain associated with the coefficients.

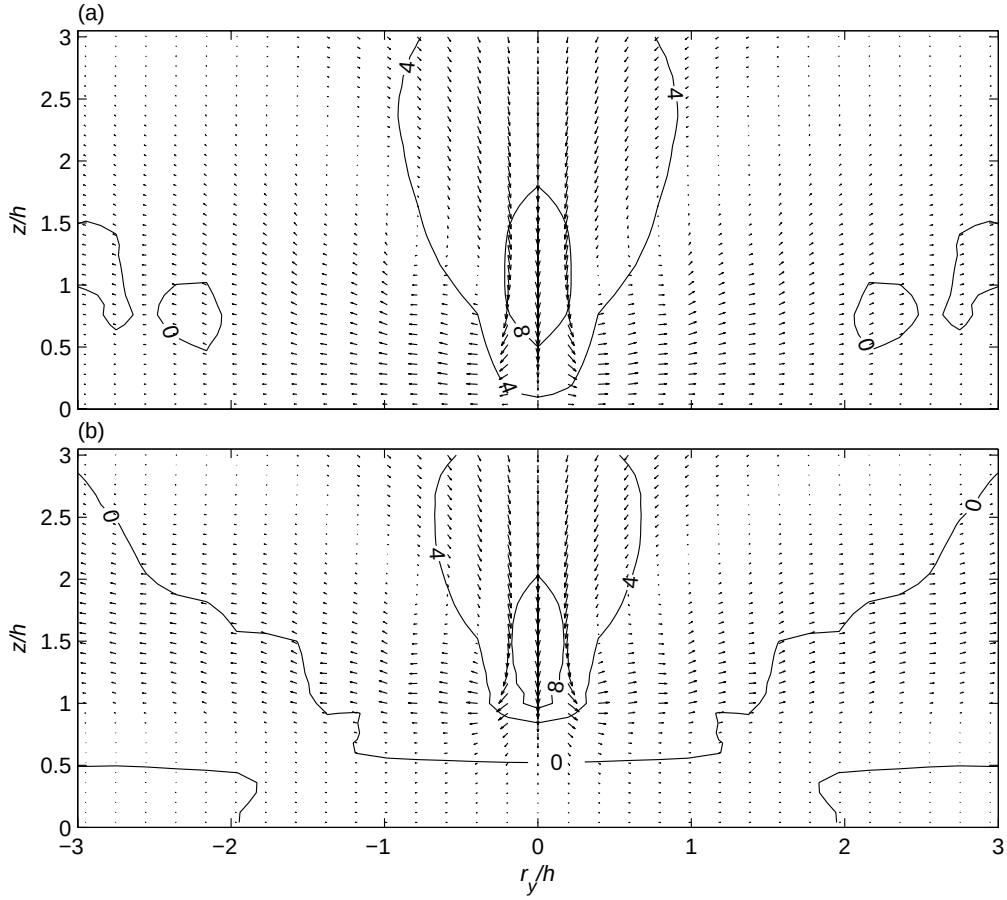

Figure 4.10. $v - w$ vector plot with u contour of the two-dimensional turbulent structure in the $y - z$ plane for (a) ESC and (b) EDC

The two-dimensional structures in the $y - z$ plane have been investigated more extensively than that in the $x - z$ plane. The results have been similar within channel flow (Moin and Moser 1989), ABL (Huang et al. 2009a), PML (Delville et al. 1999) and CSL (Finnigan and Shaw 2000), consisting of a strong sweep or ejection motion framed by a pair of counter-rotating vortices. Within channel flow and the ABL, the dominant motion is an ejection while within the CSL sweep dominates. In Figure 4.10, the vortex

pair is plotted in combination with the u-isolines for ESC and EDC. Both the vortex pair and the u-isolines move upward from ESC to EDC. This is in agreement with the uplift of the sweep motion and the span-wise vortex in Figure 4.8.

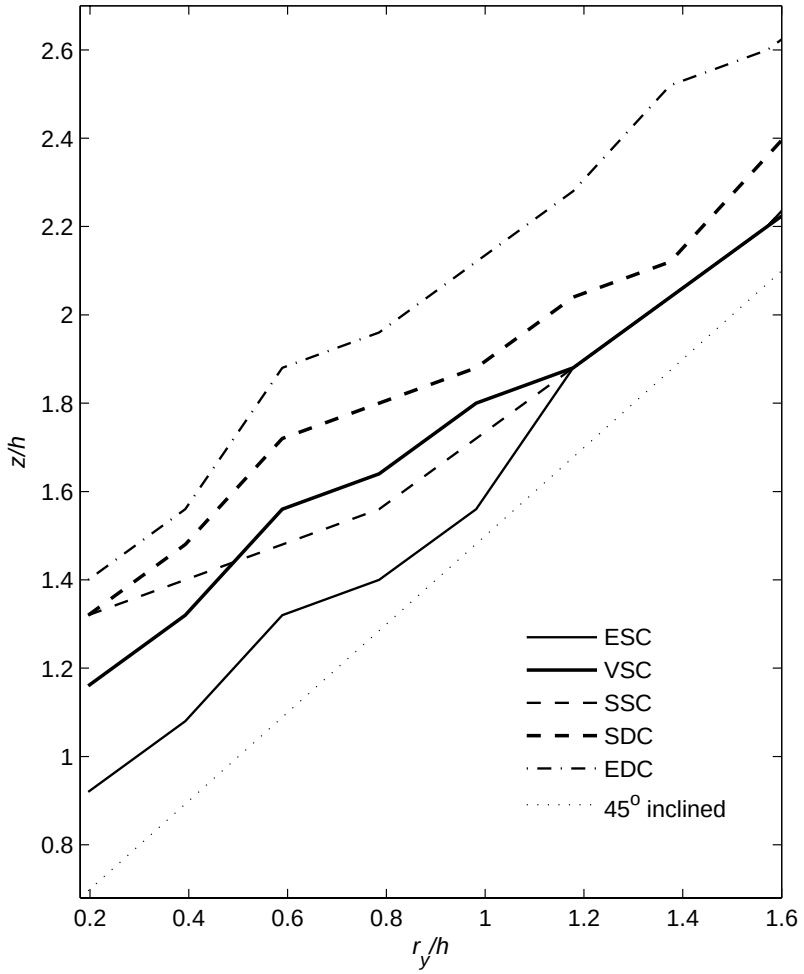

Figure 4.11. Height of v-zero-crossings of the two-dimensional coherent structures in the $y - z$ plane versus r_y for varying LAIs. The straight line with an angle of 45° is plotted for reference

The heights of the v-zero-crossings (i.e., vortex centres) are reported in Figure 4.11 for the five LAI cases. It can be observed that the vortex pair tends to move upward as the canopy vegetation density increases. Also, the centre locations of vortex pair appears to incline along the y direction at an angle of approximately 45°, much as what was shown in the ABL (Huang et al. 2009a).

With three-dimensional coherent structures, we are able to demonstrate the evolution of the $x-z$ plane structure along y in Figure 4.12, and the evolution of the $y-z$ plane structure along x in Figure 4.13, respectively.

In Figure 4.12, the $u-w$ velocity vectors of the coherent structure are projected onto different $x-z$ slices at $r_y/h=\{0, 0.4, 0.8, 1.2\}$ for the cases of SSC and EDC, respectively. Vectors of small amplitudes are magnified so that their directions can be easily discerned. A clockwise-rotating vortex is consistently found in accordance with the two-dimensional version. In the case of SSC, this type of vortex develops from a strong vertical u gradient close to ground at $r_y/h=0$ (Figure 4.12a), and then ascends to around $z/h=0.55$ at $r_y/h=1.2$. The rise of the span-wise vortex is less significant for the case of EDC: the centre of the vortex moves up from approximately $z/h=0.55$ at $r_y/h=0$ to $z/h=0.7$ at $r_y/h=1.2$.

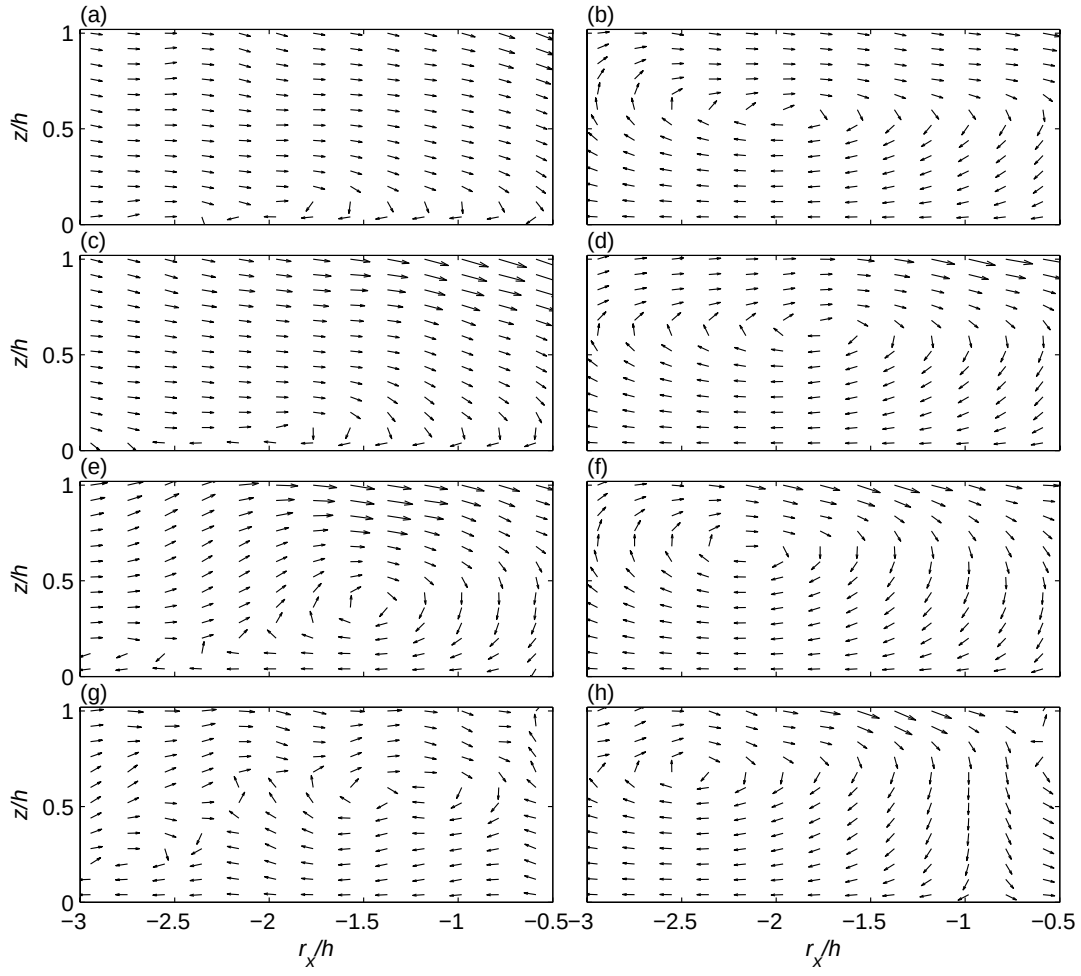

Figure 4.12. $u - w$ velocity vectors of the three-dimensional turbulent structure projected onto the $x - z$ plane for SSC (a, c, e, g) and EDC (b, d, f, h) at $r_y / h = 0$ (a, b), $r_y / h = 0.4$ (c, d), $r_y / h = 0.8$ (e, f) and $r_y / h = 1.2$ (g, h), respectively

In Figure 4.13, the $v - w$ velocity vectors of the three-dimensional coherent structures are projected onto different $y - z$ slices at $r_x / h = \{-0.8, -0.4, 0, 0.4\}$ for the cases of ESC and EDC, respectively. Since the educed coherent structures in the $y - z$ plane are symmetric with respect to $r_y / h = 0$, only half planes of r_y are showed. The

results are similar with their counterparts within channel flow (Moin and Moser 1989) and the ABL (Huang et al. 2009a) with the counter-rotating vortex pairs curving upward along x. The comparison between EDC and ESC suggests that the vortices are positioned higher at a same streamwise location r_x in EDC than in ESC.

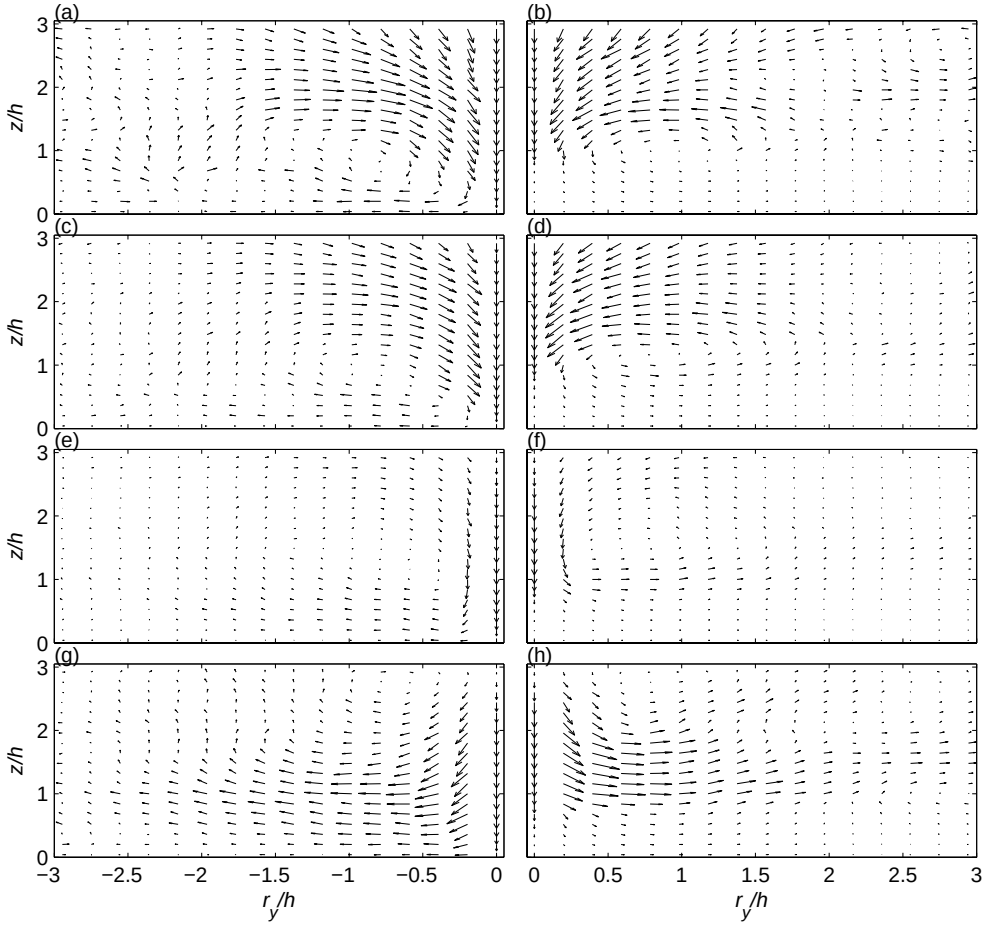

Figure 4.13. v **–** w **velocity vectors of the three-dimensional turbulent structure projected onto the** y **–** z **plane for ESC (a, c, e, g) and EDC (b, d, f, h) at** $r_x / h = -0.8$ **(a, b),** $r_x / h = -0.4$ **(c, d),** $r_x / h = 0$ **(e, f) and** $r_x / h = 0.4$ **(g, h), respectively**

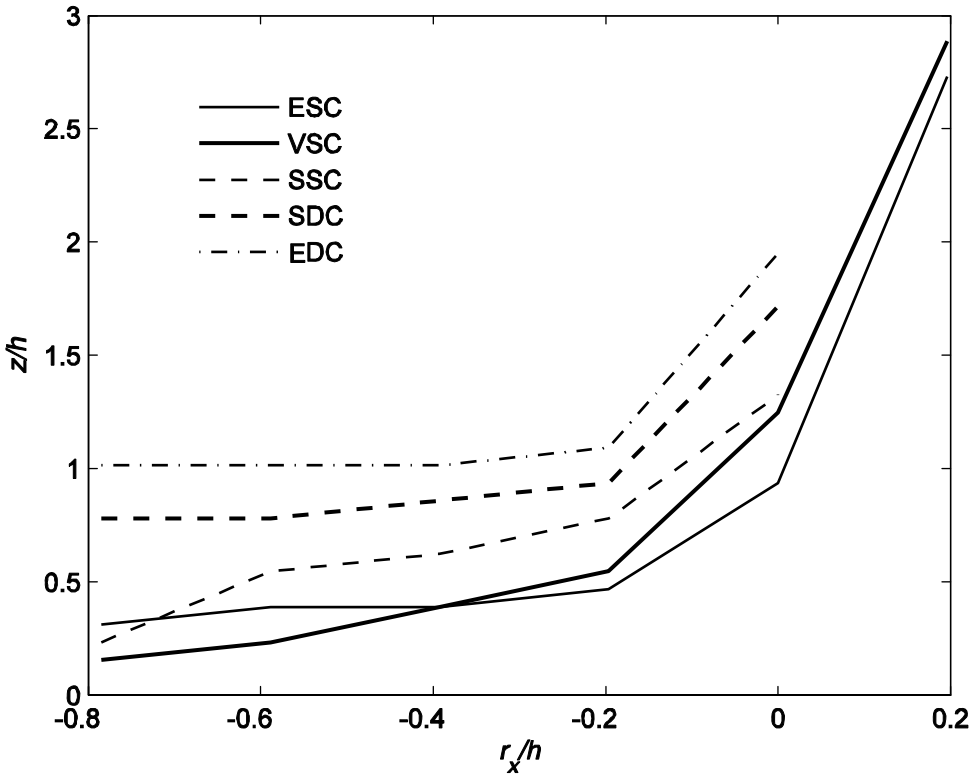

Figure 4.14. Height of v-zero-crossings of the three-dimensional turbulent structure at $r_y / h = 0.4$ against r_x / h for canopies of varying LAIs

In order to quantify the effects of vegetation density on the locations of the three-dimensional coherent structure, heights of v-zero-crossings of the vortices are identified and plotted versus r_x/h for the five cases of different densities in Figure 4.14. The span-wise position $r_y/h = 0.4$ is used to obtain this result, but other reasonable alternatives produce similar results. The streamwise vortex pairs curve up in all five cases with the angle of inclination increasing across a broad range. Taking the example of ESC, this angle is $\approx 0^o$ for $r_x/h \subset [-0.6, -0.4]$, and it increases to $\approx 80^o$ for $r_x/h \subset [0, 0.2]$. Greater

vegetation density clearly tends to cause higher elevation of the vortex pair although the cases of ESC and VSC are slightly entangled upstream of $r_x/h = -0.4$.

4.6 *Conclusions*

In this chapter, the effects of vegetation density on the flow statistics and the large-scale turbulent structures within the canopy sublayer (CSL) were systematically investigated using large-eddy simulation (LES). The results of our LES were compared to those obtained from a flume experiment in Poggi et al. (2004b) and a wind tunnel experiment in Brunet et al. (1994), Shaw et al. (1995) and Finnigan et al. (2000). The overall consistency arising from this comparison verifies the ability of our LES in producing canopy turbulence structures in good agreement with the field and laboratory measurements.

The vegetation density has significant effects on flow statistics. A denser canopy tends to result in: (1) a greater inflection strength for the vertical profile of the mean streamwise velocity at the canopy top; (2) a smaller σ_u, σ_w and $|\tau|$ inside the canopy; (3) a higher efficiency of the vertical momentum transport across the canopy-atmosphere interface; (4) a greater amplitude of skewness and kurtosis in the upper part of the canopy; (5) a smaller amplitude of two-point integral length scale; (6) a higher longitudinal convection velocity (scaled by the mean streamwise velocity) inside the canopy.

It has been shown that as the vegetation density increases from an extremely sparse canopy to an extremely dense canopy, a series of flow statistics properties of the CSL, such as the $\langle U \rangle$ inflection and the sknewness of velocity components, change from a typical value of a PML to that of a rough-wall boundary layer gradually, reflecting that canopy turbulence transitions from boundary-layer-like to mixing-layer-like. Also, the ratio of the streamwise separation between coherent eddies, Λ_x, to the shear length, L_s, converges to the value computed from experiments and numerical simulations in the fully-developed PML as the LAI increases. An exception is the $u - w$ correlation coefficient r_{uw}, whose magnitude for a dense canopy is noticeably higher than that of a rough-wall boundary layer and that of a PML. A reasonable hypothesis to interpret this is that the ability of vertical momentum transport of the two turbulence sources tends to be additive in canopy turbulence.

The large-scale coherent structures obtained from the LES were compared to those from the wind tunnel in Finnigan and Shaw (2000). A number of similarities arise from this comparison: (1) the one-dimensional coherent structures exhibit strong inflections at the canopy top, and carry over 50 percent of the total turbulent variations of u and w; (2) on the $x - z$ plane the coherent structures appear as strong sweep motions with the most energetic portion in the upper part of the canopy and above the canopy top up to $z/h \approx 2$; (3) on the $y - z$ plane the coherent structures are composed of a strong sweep motion framed by a counter-rotating vortex pair. In addition to these

similarities, many features of the coherent structures have also been demonstrated: (1) a spanwise vortex is found inside the canopy for the coherent structures projected onto the $x-z$ plane, and this vortex ascends along y; (2) the streamwise vortex pair appears as elliptical cross-sections inclined at a tilt angle of approximately 45 degree in y; (3) the streamwise vortex pair curves upward with an inclination angle up to ≈ 80 degree in x.

The effect of the vegetation density on the coherent structures was systematically investigated. As the canopy becomes denser, (1) the inflection in the one-dimensional coherent structures is intensified with the span-wise velocity component most sensitive to the density change; (2) the percentage that the coherent structures contribute to the turbulent variations of u and w does not have a significant change; (3) the peak range of the amplitude of the sweep motion in the $x-z$ projected coherent structure as well as the spanwise vortex move up; (4) the streamwise vortex pair in the $y-z$ projected coherent structure is more elevated; (5) the tilt angles of the streamwise vortex pair in both x and y do not vary significantly.

5 Across a Vegetation Discontinuity

5.1 *Introduction*

It has been shown that landscape fragmentation is one of the more ubiquitous characteristics of the modern world (Laurance 2004). Such fragmentation significantly affects, among other things, the way in which mass and momentum are exchanged between the land and the atmosphere across very broad spatial scales. In the meso-scales (O(10 km)), the area-aggregated fluxes are strongly influenced by organized motion that is driven by distinct surface contrasts such as irrigated areas in an arid region (e.g. Ookouchi et al. 1984; Michels and Jochum 1995; Jochum et al. 2006); and, at boundary layer scales (100 m – 10 km), it has been shown that the regional evapotranspiration models should take account of the effects of spatial variability in surface conditions on the dynamics of the atmospheric boundary layer (ABL) to achieve reasonable performance (e.g. De Bruin 1989; Meijninger et al. 2006). Some studies (see e.g. Albertson 1996; Bou-Zeid et al. 2007) have attempted to examine these transitions with patchworks of roughness length in large-eddy simulation (LES). However, as one of the most fundamental and representative scenarios in fragmented landscapes, vegetation transition between forested canopies and non-forested areas cannot be simply simulated by change of roughness length because the canopy morphology cannot be neglected, nor fully represented by a single roughness length (e.g. Cassiani et al. 2008).

The overall behaviour of turbulent flow in and just above the canopy airspace across the clearing-to-forest transition has been characterized as deceleration of the streamwise mean flow, an upward deflection of the mean flow, suppression of second-order moments of velocity components, and a marked increase of velocity skewnesses (Yang et al. 2006). Dupont and Brunet (2008a) studied the enhanced gust zone (EGZ) around the canopy top at several heights downstream of the leading edge of the forest. They also investigated the effects of canopy morphology on the wind flow across a forest edge, and concluded that the distance downstream needed for the flow to reach equilibrium decreases for increasing canopy density. Cassiani et al. (2008) studied the effects of canopy density on the bulk flow properties across a forest-to-clearing transition. They observed, in LES results, two mean flow recirculation zones for dense canopies: one is in the clearing area downstream of the forest-to-clearing trailing edge; another is inside the forest area. A conceptual model was proposed to interpret the mean velocity in the forest-to-clearing transition area at an intermediate canopy density as a superposition of 'exit flow' and back-facing-step-like flow, with the weights in the superposition depending on canopy density.

On the other hand, it is widely recognized that the majority of mass, momentum and energy transport between the land and the atmosphere is carried by organized turbulent motions, i.e., coherent structures (e.g. Wilson 1996; Katul et al. 2006a; Huang et al. 2009a). It has been shown that within the ABL the coherent structures are composed

of a strong sweep or ejection motion framed by a pair of counter-rotating vortices oriented generally along the streamwise direction (Huang et al. 2009a). This combined flow pattern is responsible for over 30 percent of the total TKE, and curves up in the streamwise direction with the maximum tilt angle around 70^{o} (Huang et al. 2009a). This structure has been compared to the longitudinal roll vortex observed in field studies (Wilson 1996).

The coherent structures within the canopy sublayer (CSL) have been demonstrated to be similar to those found in the ABL in the sense that they also consist of a strong sweep or ejection motion framed between a pair of streamwise vortices (Finnigan and Shaw 2000; Huang et al. 2009b). However, the coherent structures represent a greater fraction of the TKE in the CSL than in the atmospheric surface layer (ASL) (Finnigan and Shaw 2000). Huang et al. (2009b) investigated the effects of vegetation density on the morphology of the coherent structures within a horizontally homogeneous CSL. It was shown that as the canopy vegetation density increases, (1) the vertical momentum transport at the canopy-atmosphere interface is more efficient; (2) the inflection of the mean streamwise velocity becomes stronger; and (3) the coherent structures are positioned higher and closer together in the streamwise direction.

Although a fair amount of information has been uncovered about coherent structures within both the general ABL and the CSL, little is known about how the coherent structures evolve across a strong vegetation discontinuity. Provided

sufficiently large fetches for both the forested canopy part and the forest clearing part, the coherent structures in the canopy side should converge to those within a pure CSL 'far enough' from the leading edge, and the coherent structures in the clearing side should converge to those within a pure rough wall boundary layer. In this chapter, the fundamental morphological characteristics of the coherent structures across a vegetation discontinuity are explored using LES. We focus on how the following "macro-descriptors" of the coherent structures change as a function of the fetch: (1) the organization of the turbulence represented by the coherent structures, (2) the strength of inflection of the mean streamwise velocity, and (3) the elevation and orientation of the vortical structures. The effects of the ratio between the length of the forest and the length of the clearing under a given streamwise periodicity on the spatial evolution of the coherent structures are investigated as well.

5.2 *Basic Flow Statistics*

Before investigating the morphological features of the coherent structures across the forest-clearing edge, the basic flow statistics of the numerical experiments are examined. Figure 5.1 shows the $x - z$ plane variations of the mean streamwise velocity $\langle U \rangle_{yt}$ scaled by its corresponding friction velocity u_* defined as $u_*^2 = -\left\langle \tau \middle|_{x_{f2c}=-3h,\, z=h} \right\rangle_{yt}$, where τ is the total (resolved and SGS) stress. Cassiani et al. (2008) observed a recirculation zone downstream of the forest-to-clearing edge for the cases that they investigated (LAI = 4, 6 and 8, all with r = 1), which is of notable ecological significance

as it affects seed and pollen deposition in colonized gaps. This recirculation zone is consistently observed in Figure 5.1 over all three different *r* values, as characterized by negative streamwise velocities (marked by grey shaded areas). In all the three cases, the isolines are closer to each other above the forest area than above the clearing area, which is a consequence of the drag force imposed by the canopy elements and the constraint of the continuity equation.

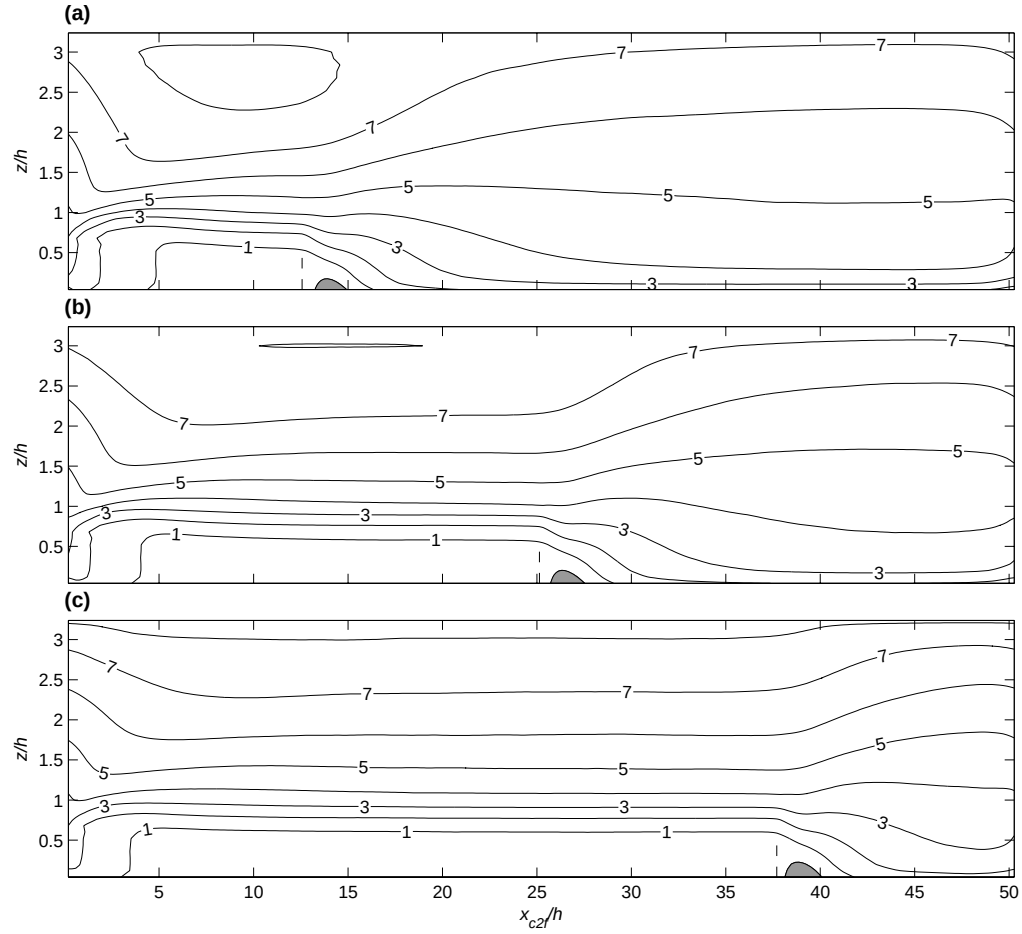

Figure 5.1. Contours of the mean streamwise velocity $\langle u \rangle_{yt}$ scaled with u_* for different forest-clearing ratios: *r* = (a) 1/3; (b) 1; (c) 3. Grey areas correspond to negative velocity and the positions where the forest ends are marked by dashed lines

A feature shared by the three cases is that it takes a much greater distance for the mean velocity to reach equilibrium following the forest-to-clearing transition compared to the clearing-to-forest transition, which is consistent with the analysis of Albertson and Parlange (1999b) for the smooth/rough surface transition. For instance, from Figure 5.1a it can be noted that a fetch of at least 20h is needed to reach equilibrium for $\langle u \rangle_{yt}$ downstream of the forest-to-clearing trailing edge; however, based on Figure 5.1c it is evident that it takes less than 10h downstream of the clearing-to-forest discontinuity for $\langle u \rangle_{yt}$ to reach equilibrium. As r increases from 1/3 to 3 the mean wind flow generally becomes slower, as evidenced by the rise of the isolines of $\langle u \rangle_{yt}$. Taking the example of $\langle u \rangle_{yt} / u_* = 5$, it is positioned around z/h = 1.2 for r = 1/3, and 1.5 for r = 3 in the forest area; around z/h = 1.2 for r = 1/3, and 1.8 for r = 3 in the clearing area.

Figure 5.2 shows similar contour plots as Figure 5.1 but for $\langle w \rangle_{yt}$ (scaled by u_*). Consistent with previous findings in both field (e.g., Irvine et al. 1997) and numerical (e.g., Yang et al. 2006; Cassiani et al. 2008) experiments, a strong downward wind flow is found downstream of the forest-to-clearing trailing edge and an even stronger upward wind flow around the clearing-to-forest leading edge. The results at the forest-to-clearing transition appear to be insensitive to r. Note that close to the edge and ground a small region of positive $\langle w \rangle_{yt}$ exists approximately within the range $x_{f2c}/h \subset (-0.5, 1.5)$ in the x direction and $z/h \subset (0, 0.8)$ in the z direction, marking the same recirculation zone previously defined from $\langle u \rangle_{yt}$ in Figure 5.1.

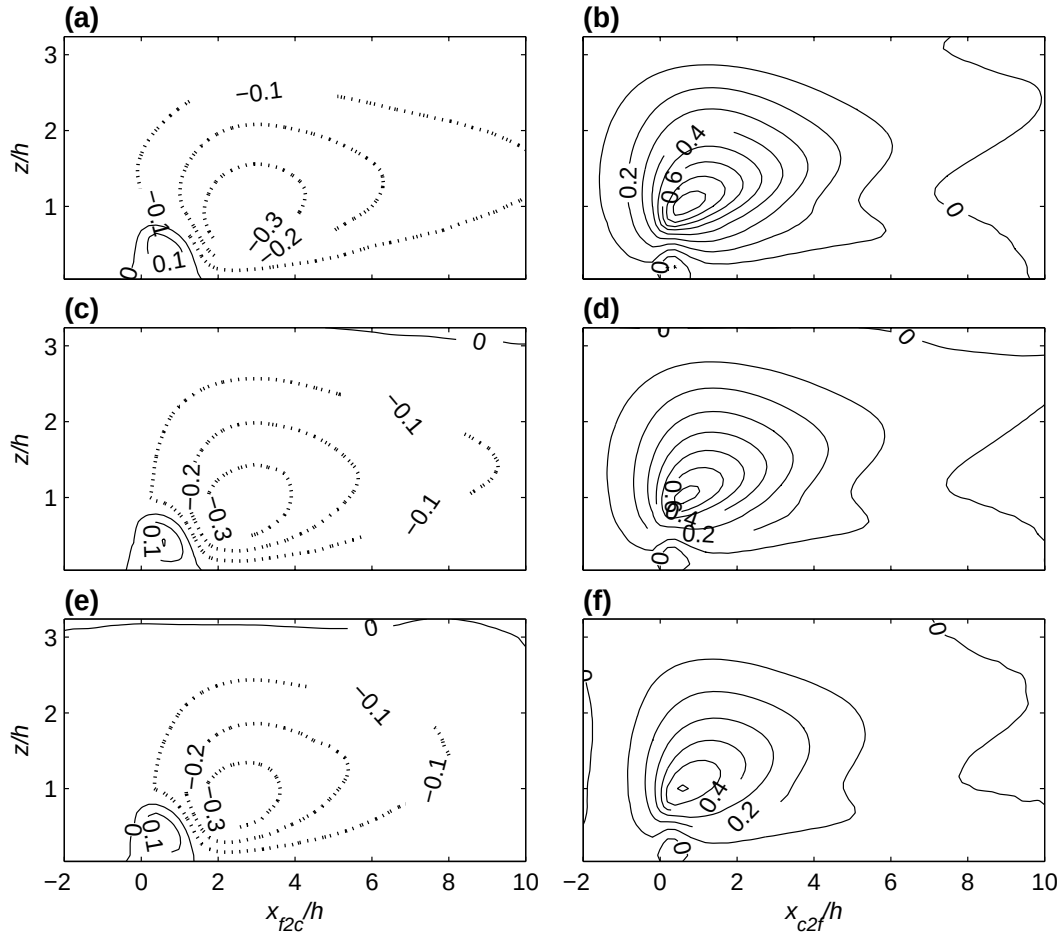

Figure 5.2. Contours of the mean vertical velocity $\langle W \rangle_{yt}$ scaled with u_* for different forest-clearing ratios: r = (a, b) 1/3; (c, d) 1; (e, f) 3: contours of positive values are drawn in thin solid lines and negative values in thick dotted lines

The results for the clearing-to-forest transition (Figure 5.2b, d, f) show that the location of the upward mean flow is insensitive for r. However, the strength of the upward mean wind flow does vary with r. The maximum amplitude of $\langle W \rangle_{yt} / u_*$ decreases from ≈ 0.8 to ≈ 0.6, as r increases from 1/3 to 3. This is consistent with what was found from Figure 5.1: a smaller r generates a stronger inflow upstream of the

clearing-to-forest leading edge, giving rise to a stronger mean vertical transport across the clearing-to-forest transition.

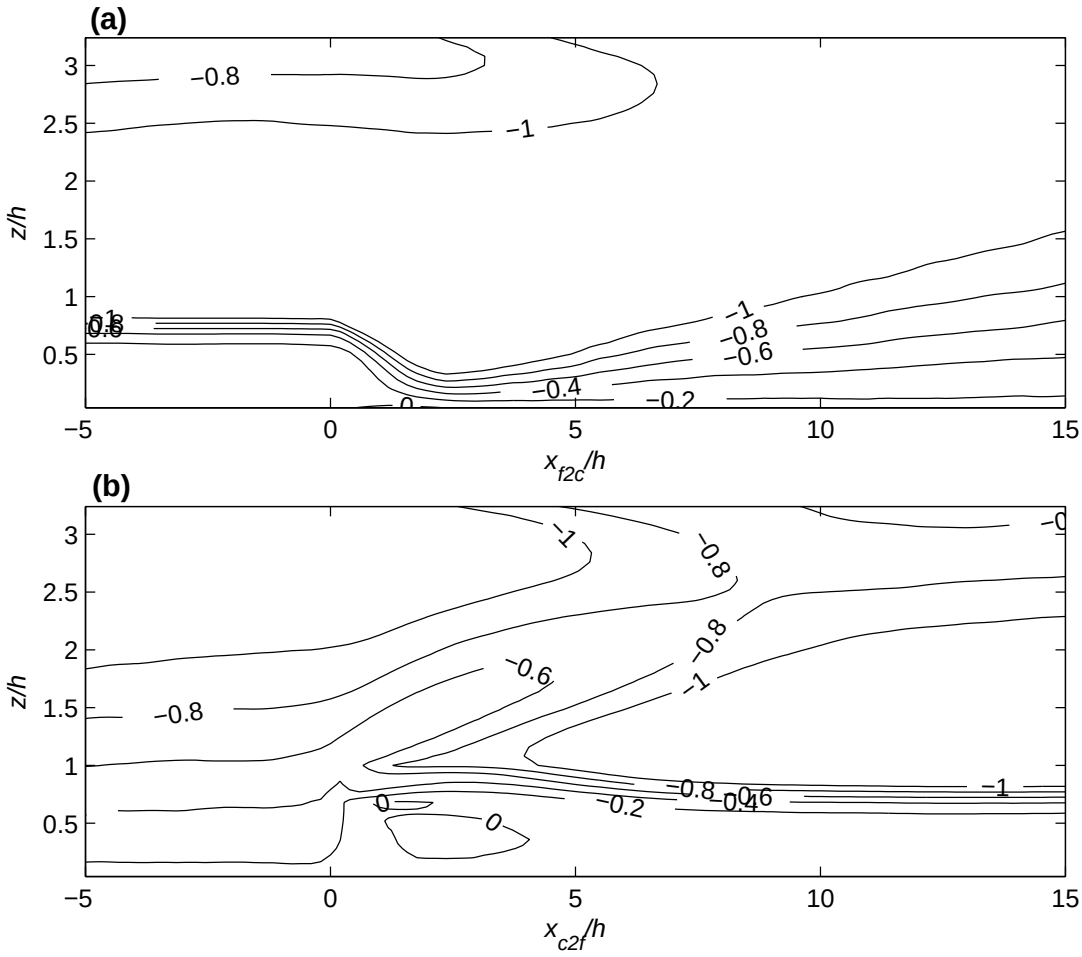

Figure 5.3. Contours of the total stress (the resolved stress and the SGS stress) scaled with u_*^2 in the forest-to-clearing transition (a) and the clearing-to-forest transition (b) for $r = 1$

In Figure 5.3 the total stress τ is presented at both the forest-to-clearing and the clearing-to-forest transitions for $r = 1$. The most pronounced features are the establishments of internal boundary layers downstream of the two edges. The isolines

in the upper part of canopy keep descending across the forest-to-clearing transition due to the mean downward transport until ≈ 3*h* downstream of the trailing edge. Farther downstream, the isolines begin to climb and separate significantly from each other, keeping with the establishment of a classic rough wall boundary layer over the surface of the clearing. The process is similar across the clearing-to-forest transition as can be seen in Figure 5.3b. The isolines begin to climb as a direct consequence of the upward transport of the mean flow surrounding the leading edge. Downstream of the leading edge, a new internal boundary layer is quickly established which is reflected by the ascension and stabilization of the isolines (e.g. $\tau/u_*^2 = -1$). A comparison of the stress results with the results of the mean velocities suggests that a greater downstream distance is needed for the stress to adjust to equilibrium than that needed for the mean velocities to equilibrate yet their probability density functions (PDFs) are closely associated in the equilibrium sublayer (e.g. Chu et al. 1996), which agrees with Yang et al.(2006).

In consideration of the fundamental importance of the inflection point in the mean streamwise velocity profile to generate coherent structures within canopy turbulence (see e.g. Raupach et al. 1996; Finnigan 2000), the curvature of $\langle u \rangle_{yt}$ in the vertical direction is examined. $\langle U \rangle_{yt}$ is scaled by its value at the treetop $u_h = \langle u \rangle_{yt}|_{z=h}$ as $u_s(x,z) \equiv \langle u \rangle_{yt}(x,z) / u_h(x)$. Then the curvature is calculated as

$k(x,z) = \partial_z \partial_z u_s \Big/ \left(1 + \left(\partial_z u_s\right)^2\right)^{3/2}$. Compared to the traditional definition of curvature, which only utilizes the amplitude of $k(x,z)$, the information of the sign is kept here to indicate the concavity or convexity in the vertical profile of the mean streamwise velocity.

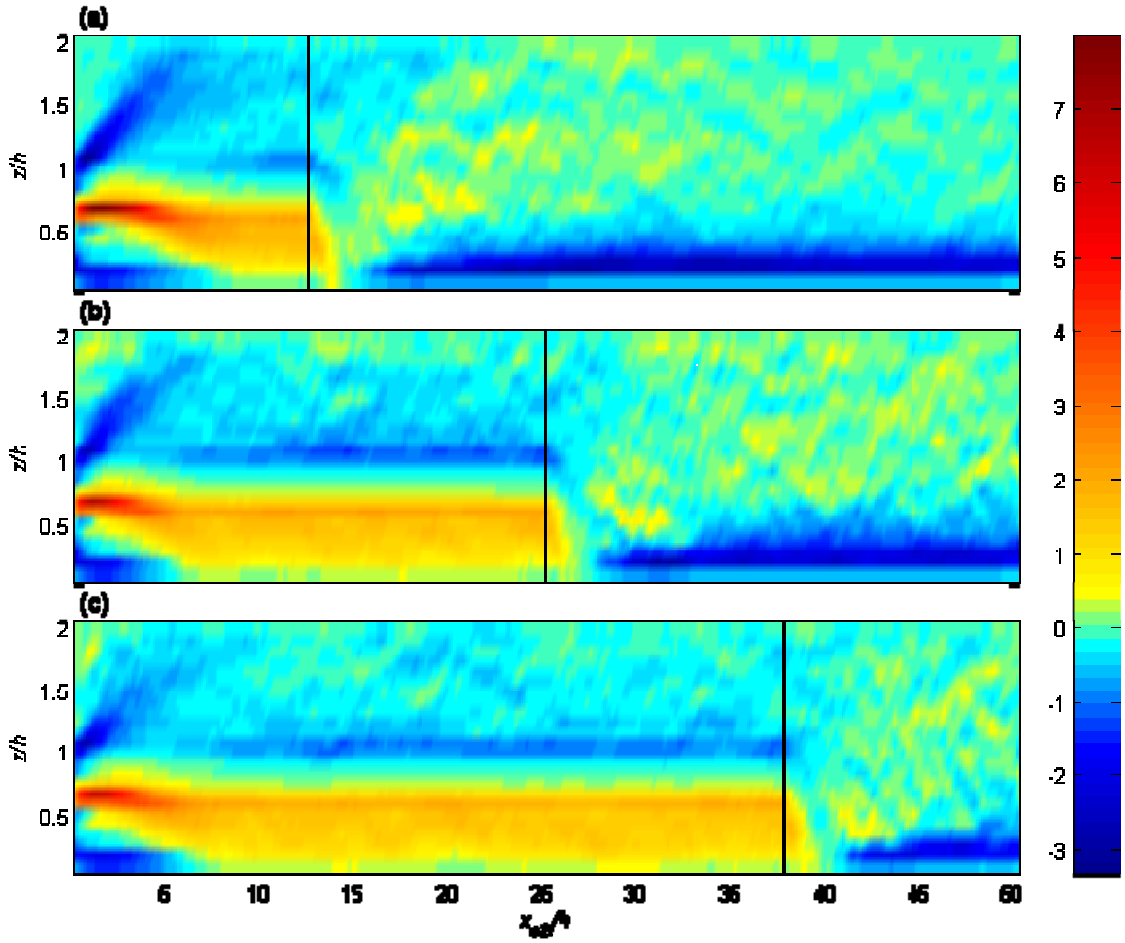

Figure 5.4. Colour plots of curvature distribution of $\langle u \rangle_{yt}/u_h$ on the $x - z$ plane for (a) $r = 0.33$; (b) $r = 1$; (c) $r = 3$. The black line indicates the forest-to-clearing transition

It is clearly visible in Figure 5.4 that the forest area and the clearing area are represented by different patterns of curvature profiles. In the well-developed region of the forest area, the curvature is negative above treetop level with the amplitude peaking around $z/h = 1.1$. Below the treetop the curvature is positive and the amplitude peaks approximately at $z/h = 0.6$. In between, there is an inflection point around the treetop, connected with the generation of Kelvin-Helmholtz instabilities and large-scale coherent structures in the CSL (see e.g. Raupach et al. 1996). The pattern of the curvature in the well-developed region of the clearing area is much simpler with significantly negative curvatures below $z/h = 0.5$ representing the primary instability generated by the interaction between the mean flow and the clearing surface.

Because of the upward mean flow transport, the features of curvature in the clearing-to-forest adjustment zone ($x_{c2f} \subset (0, 10h)$) vary significantly from those in the equilibrium zone (i.e., $x_{c2f} > 10h$): (1) the positive curvature is much stronger in the adjustment zone than in the equilibrium zone and its peak amplitude is more elevated ($z \approx 0.7h$); (2) the position of the peak negative curvature moves upward in the adjustment zone with a distortion angle similar to that of the mean wind flow. The increasing height of both the positive and negative curvature locations in the adjustment zone of the forest results in the corresponding increasing elevation of the inflection and the Kelvin-Helmholtz instabilities. Note that the elevated primary instabilities reside in approximately the same region as the EGZ demonstrated in Dupont and Brunet (2008a).

As *r* increases, the peak amplitudes of both the positive and negative curvatures in the adjustment zone decrease, which then cause the strength of Kelvin-Helmholtz instabilities to decrease. This is consistent with the conclusion drawn from Figure 5.1 and Figure 5.2 that at a smaller *r* the inflow upstream of the leading edge is stronger. In summary, the comparison of the basic flow statistics with previous results supports the general fidelity of the numerical experiments.

5.3 *Quadrant Analysis*

With the LES runs shown to be consistent with previous results, we proceed to study the evolution of coherent structures across the vegetation discontinuities. Among all the coherent structures reported within the CSL and the ABL, the sweep-ejection sequence is probably one of the most common forms owing to the wide application of the quadrant-hole technique as well as the substantial role it plays in momentum transport. What has been consistently found in canopy studies is that the dominant contributor of momentum transport within canopy and around the canopy top is sweep while ejection begins to dominate as it goes upward from the canopy top (Shaw et al. 1983; Finnigan and Shaw 2000; Poggi et al. 2004b). Similar conclusion has been drawn for the ABL that the dominant motion shifts from ejection to sweep as the ground surface is approached with the height of sweep-ejection balance depending on the surface roughness (Raupach 1981; Katul et al. 2006a).

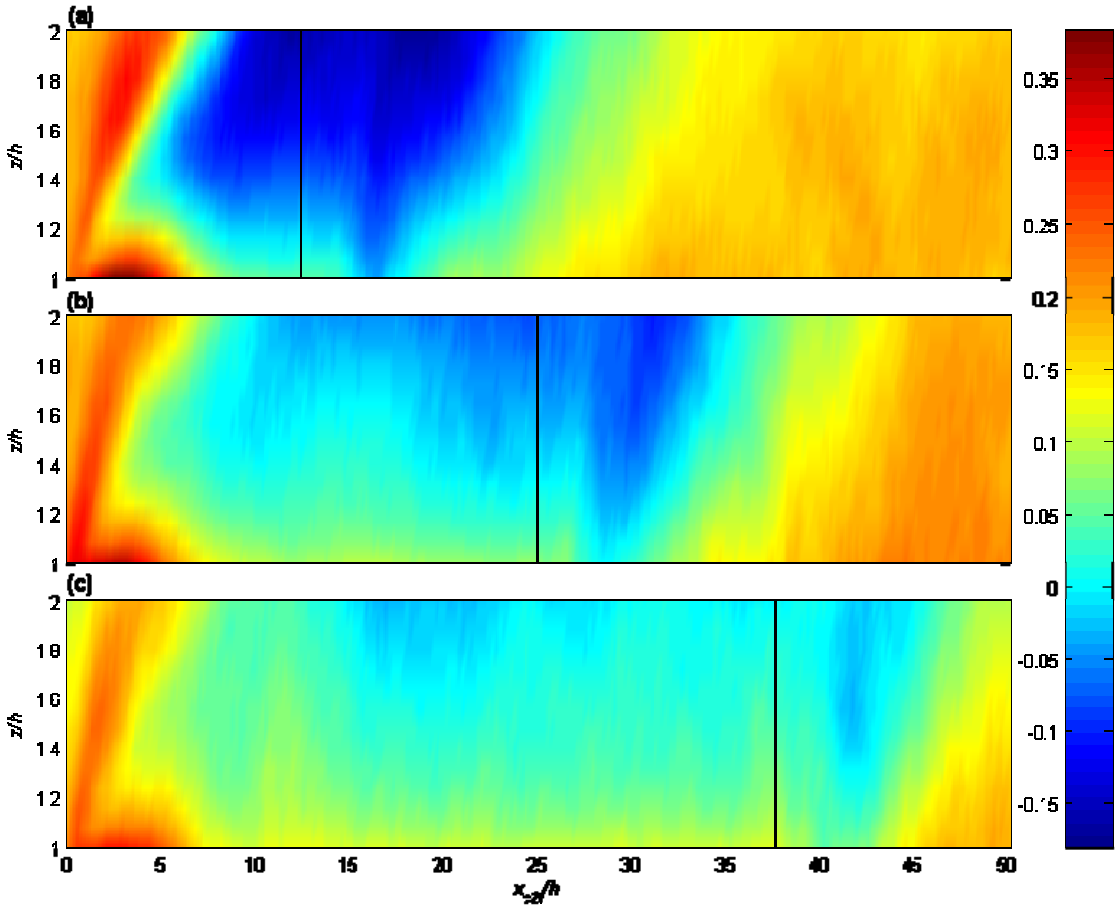

Figure 5.5. Colour plots of ΔS_0 on the $x - z$ plane for (a) $r = 0.33$; (b) $r = 1$; (c) $r = 3$. The black line indicates the forest-to-clearing transition

As a first step towards understanding the significance of the coherent structures in momentum transport, quadrant analysis is conducted to quantify the relative importance of sweep and ejection across the forest-to-clearing transition and the clearing-to-forest transition. To this purpose, we calculate $\Delta S_0(x, z)$, which is defined as

$$\Delta S_0(x,z) = \frac{\langle u'w' \rangle_{yt,IV} - \langle u'w' \rangle_{yt,II}}{\langle u'w' \rangle_{yt}}$$, where $\langle u'w' \rangle_{yt,IV}$ denotes the fraction of $\langle u'w' \rangle_{yt}$

contributed by all the sweep events and similarly $\langle u'w' \rangle_{yt,II}$ the fraction of $\langle u'w' \rangle_{yt}$ by all the ejection events (see e.g. Raupach 1981; Poggi et al. 2004b). From the definition it is clear that positive ΔS_0 implies that sweep dominates over ejection and negative ΔS_0 is for the contrary. In Figure 5.5 the result of ΔS_0 is demonstrated for three cases of different r values. Consistent with previous results in the ABL and the CSL, sweep is dominant below $z/h = 2$ in the equilibrium zone of the clearing area, and in the equilibrium zone of the canopy area the dominant motion shifts from sweep to ejection as it goes up from the canopy top. The mean flow has a marked effect on the sweep-ejection dominance across the transitions. Immediately downstream of the trailing edge of the forest, the dominance of ejection in partial vertical range of $[h, 2h]$ continues as the mean flow moves downward. In the adjustment zone downstream of the leading edge of the forest, the mean flow carries upward the sweep-dominant turbulence which is generated as the mean flow hits the canopy edge. In addition to the effect of the mean flow, it is interesting to observe that the sweep-dominant region extends higher in the equilibrium zone of the clearing area than in the equilibrium zone of the canopy area. This can probably be explained by the vertical length scale of turbulence in the two areas. In the canopy turbulence, the key length scale has been identified as the shear length (defined as the mean streamwise velocity divided by the vertical gradient of the mean streamwise velocity at the canopy top) (Raupach et al. 1996), which is much smaller than the

boundary layer depth in the ABL. Finally, a larger r tends to weaken the dominance of both sweep and ejection.

5.4 *One-Dimensional Analysis*

With the relative importance of sweeps and ejections quantified, we proceed next to reveal the morphological features of the coherent structures. Note that the POD technique itself is not able to distinguish the dominance of sweep and ejection due to its nature of optimizing the variance rather than the covariance (see Holmes et al. 1996; Huang et al. 2009b). The POD modes $\psi^{(m)}$ sequentially represent the coherent structures as they optimally contribute the largest single fraction of the TKE integrated over the region of interest (e.g. Moin and Moser 1989; Finnigan and Shaw 2000; Huang et al. 2009a, b). We first study the 1-D coherent structures in the vertical direction in order to show explicitly the evolution of the inflection of the coherent structures across the vegetation discontinuities. Then, the results of 2-D coherent structures in the $x - z$ plane and in the $y - z$ plane are demonstrated, respectively.

The first one-dimensional modes $\psi_i^{(1)}$ at six different locations downstream of the forest-to-clearing trailing edge are demonstrated in Figure 5.6. The eigenmodes $\psi_i^{(1)}$ are scaled by their values at $z = h$ (denoted as $\psi_{ih}^{(1)}$), where i is the velocity index, to clarify the comparison. Inside and immediately downstream of the forest canopy (e.g., $x_{f2c}/h = 0$ and $x_{f2c}/h = 0.79$), $\psi_1^{(1)}$ is characterized by a strong inflection point, which

peaks around $z/h = 1.2$. Farther downstream, both $\psi_1^{(1)}$ and $\psi_2^{(1)}$ become gradually less inflected. There is no clear trend for the inflection of $\psi_3^{(1)}$; however, an examination of the elevations at which $\psi_3^{(1)}$ reaches its peak values reveals that these decrease until $x_{f2c} = 3.14$, and then increase. Since the vertical velocity is more suitable to reflect the active turbulence than the streamwise and spanwise velocities in the lower part of the ABL (see e.g. Katul et al. 1996b; Raupach et al. 1996), this suggests that the coherent structures move down first and then move up downstream of the trailing edge.

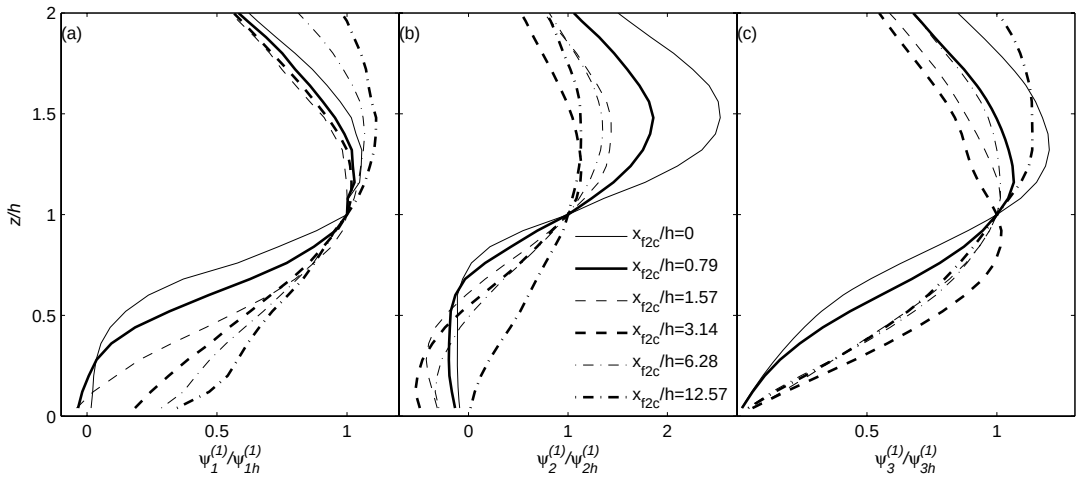

Figure 5.6. Evolutions of the first one-dimensional eigenmodes of (a) u; (b) v; (c) w scaled with their corresponding values at $z = h$ in the forest-to-clearing transition for $r = 0.33$

Figure 5.7 shows the same POD modes but for four different locations downstream of the clearing-to-forest leading edge. The inflection emerges immediately downstream of the leading edge and is strengthened as it goes farther for all the three

velocity components. Consistent with the mean flow results is that it takes a much shorter distance for $\psi_i^{(1)}$ to reach equilibrium from clearing-to-forest than vice-versa.

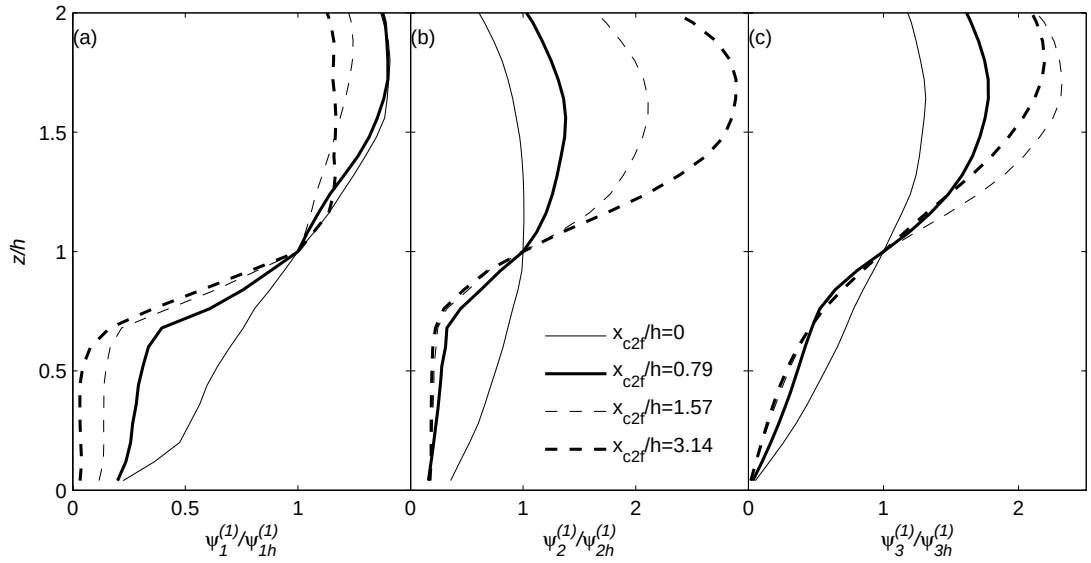

Figure 5.7. Evolutions of the first one-dimensional eigenmodes of (a) u; (b) v; (c) w scaled with their corresponding values at $z = h$ in the clearing-to-forest transition for $r = 3$

In addition to revealing the morphological features of the coherent structures, it is also of interest to understand how important these structures are. One measure frequently used to quantify this importance is the percentage that the first eigenmode represents of the total TKE, defined as $p^{(i)} = \lambda^{(i)} \Big/ \sum_i \lambda^{(i)}$ (e.g. Moin and Moser 1989; Finnigan and Shaw 2000; Huang et al. 2009a, b). Figure 5.8 demonstrates $p^{(i)}$ for the first two eigenmodes and the three different *r* values. Downstream of the forest-to-clearing transition, $p^{(1)}$ decreases quickly and then increases with the location of the minimum falling in the region $2 < x_{f2c}/h < 4$, which implies that the flow loses its

organization to some extent immediately downstream of the canopy edge and then redevelops gradually farther downstream as the mean flow begins to more intensely and consistently interact with the clearing surface. The $p^{(1)}$ have not converged to their equilibrium values for the cases r = 1 and 3 due to their inadequate fetches downstream of the trailing edge.

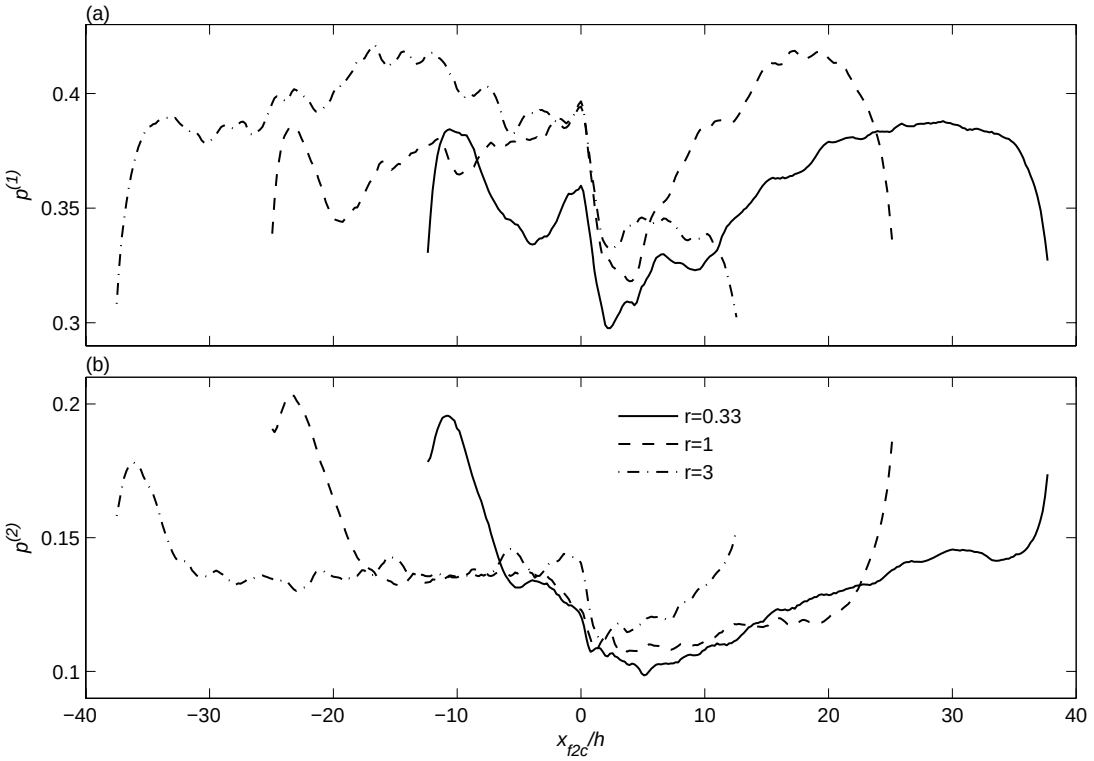

Figure 5.8. Evolutions of the relative contributions of (a) the first and (b) the second one-dimensional eigenmode to the total TKE along the streamwise direction

$p^{(1)}$ begins to decrease around 5h upstream of the clearing-to-forest leading edge, suggesting that the organization of the turbulence is being destroyed gradually in this region. Downstream of the clearing-to-forest edge, $p^{(1)}$ then increases,

corresponding to the formation process of the coherent structures from Kelvin–Helmholtz instabilities. Note that unlike $p^{(1)}$, $p^{(2)}$ keeps increasing across the clearing-to-forest edge from ≈ 2*h* upstream to ≈ *h* downstream. Referring back to Figure 5.2, the position at which $p^{(2)}$ reaches its peak value ($x_{c2f}/h \approx 1$) corresponds to where the amplitude of $\langle w \rangle_{yt}$ is the maximum in the forest area, which indicates that the "secondary coherent structures" (to coin a term) represented by $\psi^{(2)}$ arise from instabilities associated with the vertical transport of the mean wind.

5.5 *Multi-Dimensional Analysis*

Compared to the one-dimensional coherent structures investigated in the previous subsection, the two-dimensional coherent structures provide additional geometric information in the streamwise or the spanwise direction.

Two separate POD analyses have been carried out to educe the two-dimensional coherent structures on the $x - z$ plane and the $y - z$ plane, respectively. For the decomposition on the $y - z$ plane, the POD analysis is performed in the frequency space and the method of *u*-compactness is used for phase recovery, similarly as adopted in Finnigan and Shaw (2000) and Huang et al. (2009b). However, for the decomposition on the $x - z$ plane, it is unnecessary to perform the POD analysis in the frequency space because the streamwise direction is inhomogeneous in the transition areas of our case due to the vegetation discontinuity (see Holmes et al. 1996). Instead, the two-

dimensional coherent structures on the $x - z$ plane have been educed directly from the physical space.

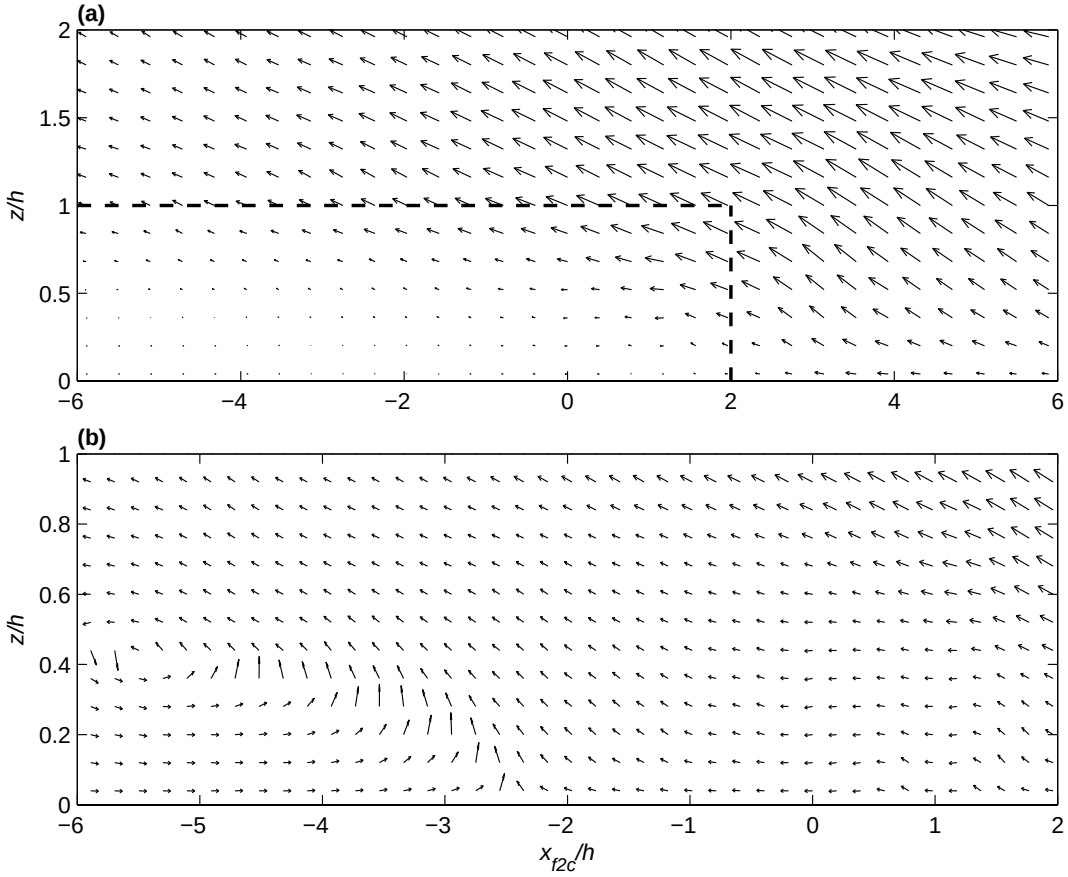

Figure 5.9. Two-dimensional coherent structures projected onto the *x*-*z* plane (*r* = 0.33) for (a) the forest-to-clearing transition; (b) the framed area in (a) with the arrow length magnified (nonuniformly) to reveal more clearly flow directions

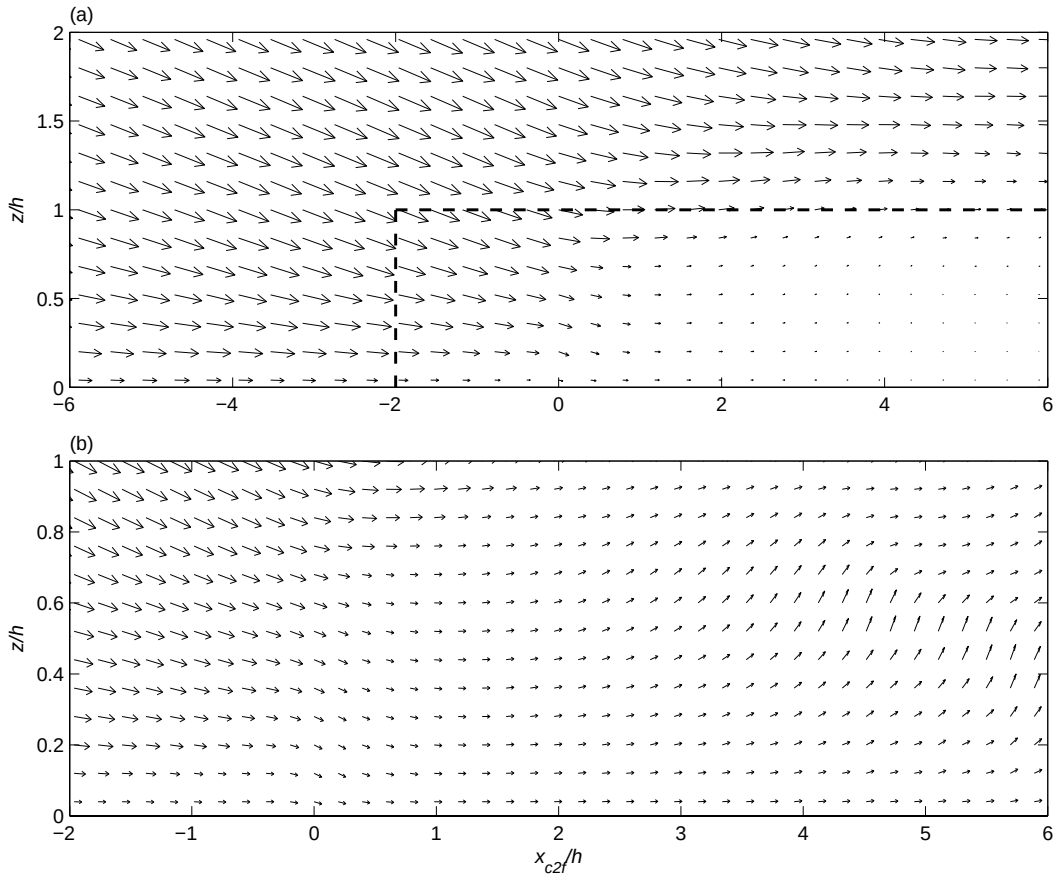

Figure 5.10. Two-dimensional coherent structures projected onto the *x*-*z* plane (*r* = 0.33) for (a) the clearing-to-forest transition; (b) the framed area in (a) with the arrow length magnified (nonuniformly) to reveal more clearly flow directions

The two-dimensional coherent structures projected onto the $x - z$ plane are shown in Figure 5.9 for the forest-to-clearing transition and in Figure 5.10 for the clearing-to-forest transition. In consideration of the result regarding the relative importance of sweeps and ejections in Figure 5.5, the orientation of the coherent structure in Figure 5.9 is forced to be reconciled with ejections while in Figure 5.10 it is consistent with sweeps. Note that the velocity components revealed here are turbulent,

which should be distinguished from the mean flow velocities shown in Figure 5.1 and Figure 5.2. Finnigan and Shaw (2000) performed a POD analysis on turbulent velocities measured in a wind tunnel with a horizontally uniform canopy (i.e. no discontinuity as studied here) and found that the coherent structure in the $x - z$ plane for a CSL consists of a weak updraft and a strong sweep. A similar analysis was conducted by Huang et al. (2009b) through numerical simulations with similarly homogeneous canopies and a spanwise oriented vortex was observed below the treetop for the cases with dense canopies. It is found here that in both the forest-to-clearing transition and the clearing-to-forest transition the dominant motion is characterized by a cluster of sweeps or ejections. A spanwise vortex is observed inside the canopy side of the forest-to-clearing transition with the centre positioned around $\left(x_{f2c}/h, z/h\right) = \left(-5.5, 0.4\right)$. The coherent structures have weaker downward motion in the forest area than in the clearing area at the same vertical level in Figure 5.10. Downstream of $x_{c2f}/h \approx 2$ inside the canopy, the dominant motion is an updraft.

In addition to demonstrating the two-dimensional coherent structures in the $x - z$ plane, the two-dimensional coherent structures in the $y - z$ plane are shown in Figure 5.11 for the forest-to-clearing transition and in Figure 5.12 for the clearing-to-forest transition. The orientation of the coherent structures is forced to be consistent with sweeps for convenience of comparison.

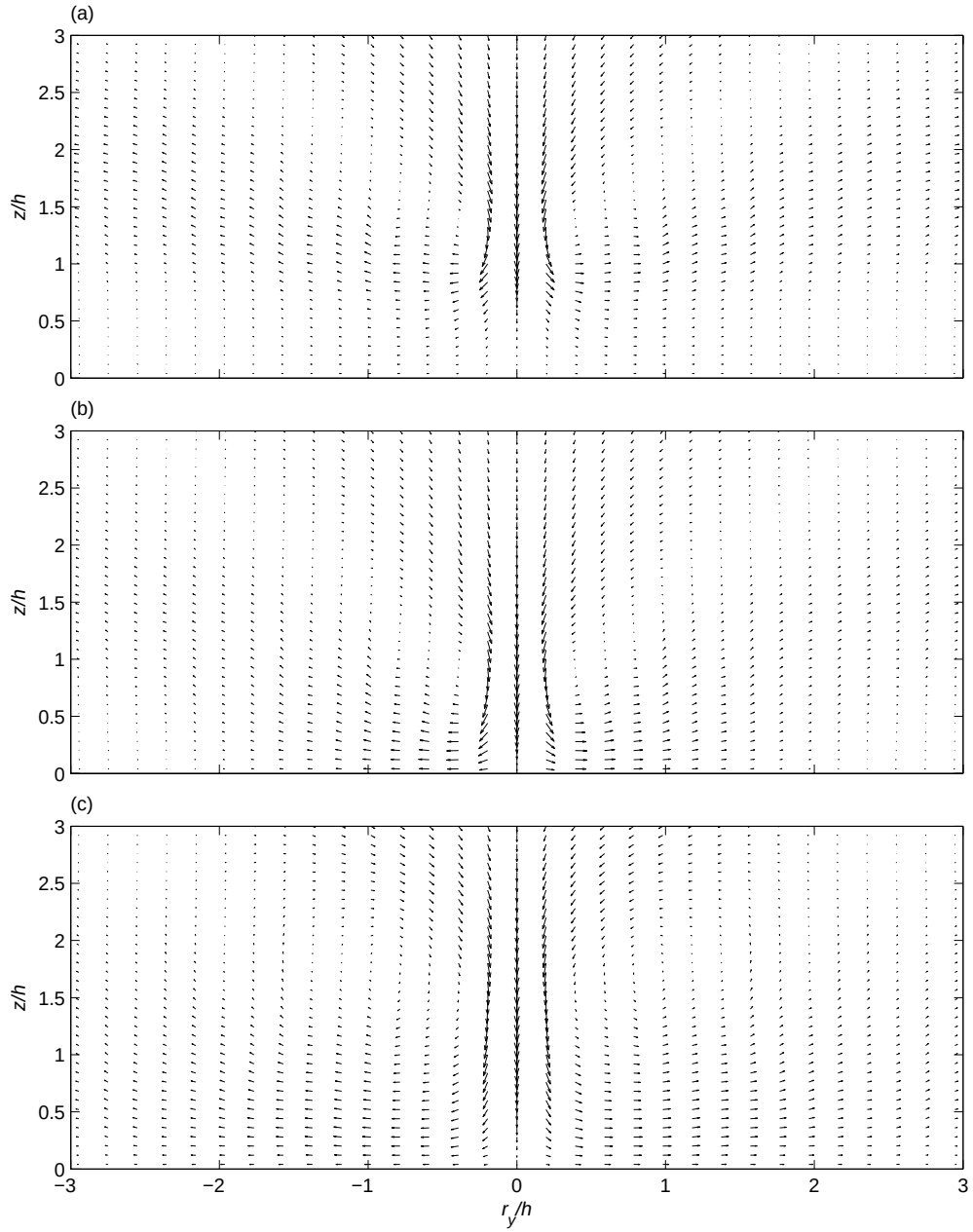

Figure 5.11. Evolution of the two-dimensional coherent structures projected onto the $y-z$ plane in the forest-to-clearing transition at (a) $x_{f2c}=0$; (b) $x_{f2c}=2.95$; (c) $x_{f2c}=10.21$. The case of $r=1$ is used

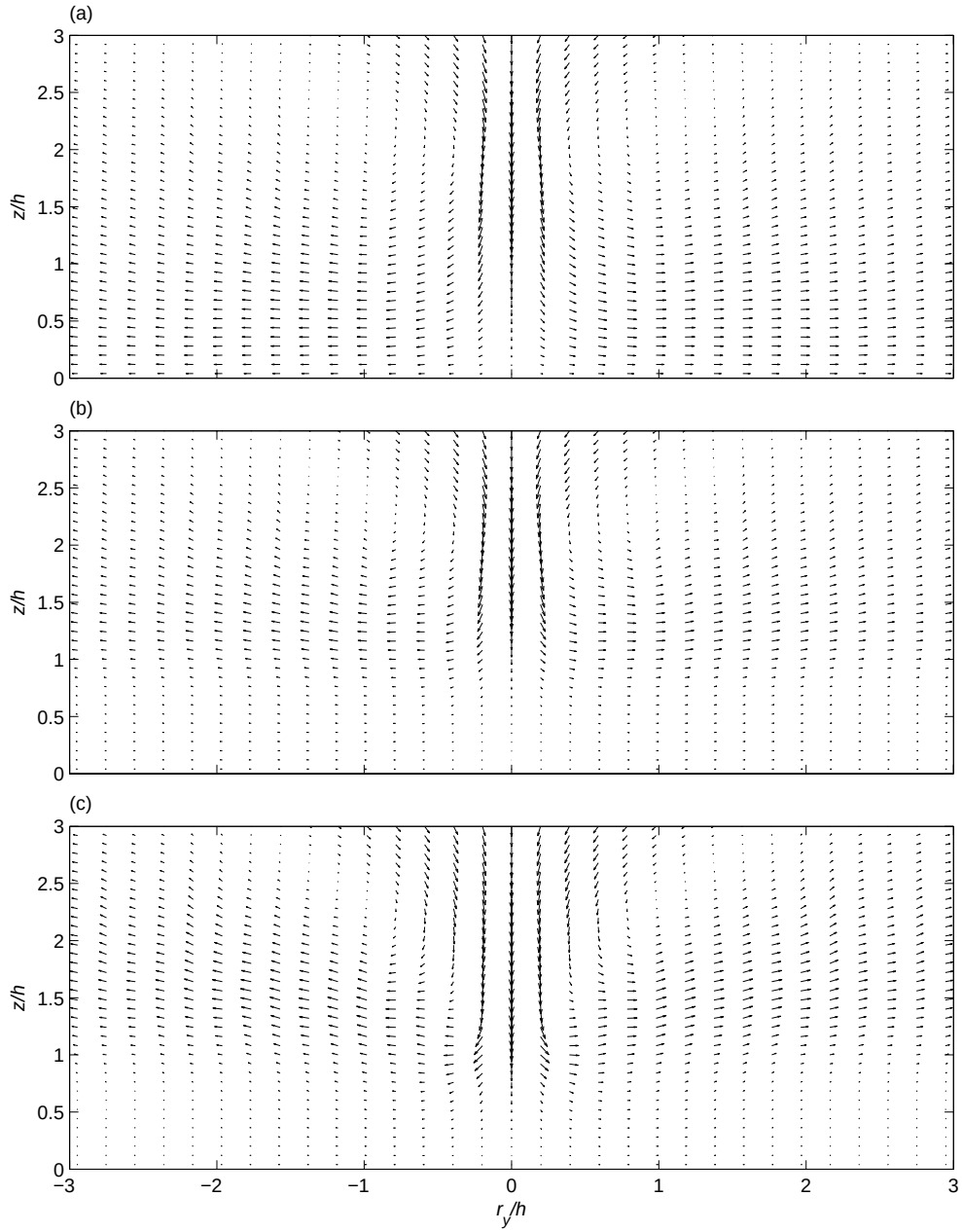

Figure 5.12. Evolution of the two-dimensional coherent structures projected onto the $y-z$ plane in the clearing-to-forest transition at (a) $x_{c2f}=0$; (b) $x_{c2f}=1.96$; (c) $x_{c2f}=3.93$. The case of $r=1$ is used

Finnigan and Shaw (2000) showed that within a CSL the two-dimensional coherent structure in the $y - z$ plane consists of a strong sweep motion framed by a pair of counter-rotating vortices. Huang et al. (2009b) confirmed the existence of the double roller structure. Furthermore, it was concluded in Huang et al. (2009b) that the streamwise vortex pair is systematically positioned lower in case of sparser canopies. Similar structures were found within the ABL (Huang et al. 2009a).

The structural pattern of a strong sweep motion framed by a pair of counter-rotating vortices is consistently observed in this work through the forest-to-clearing transition and the clearing-to-forest transition. However, the vertical position and spanwise orientation of the vortex pair varies significantly across the vegetation discontinuity. Figure 5.11 shows the two-dimensional coherent structures in the y - z plane at three different locations downstream of the forest-to-clearing trailing edge (x_{f2c}/h = 0, 2.95, and 10.21). Two trends in the x direction with respect to the vortex pair can be noted from this figure: (i) the vortex pair descends first following the transition to a clearing and then ascends; (ii) the angle of inclination of the vortex in the spanwise direction decreases. Figure 5.12 presents the two-dimensional coherent structures in the $y - z$ plane at three different streamwise locations downstream of the clearing-to-forest leading edge (x_{c2f}/h = 0, 1.96 and 3.93). Two pronounced trends emerge in Figure 5.12: (i) the vortex pair descends downstream of the leading edge; (ii) the angle of inclination of the vortex in the spanwise direction increases.

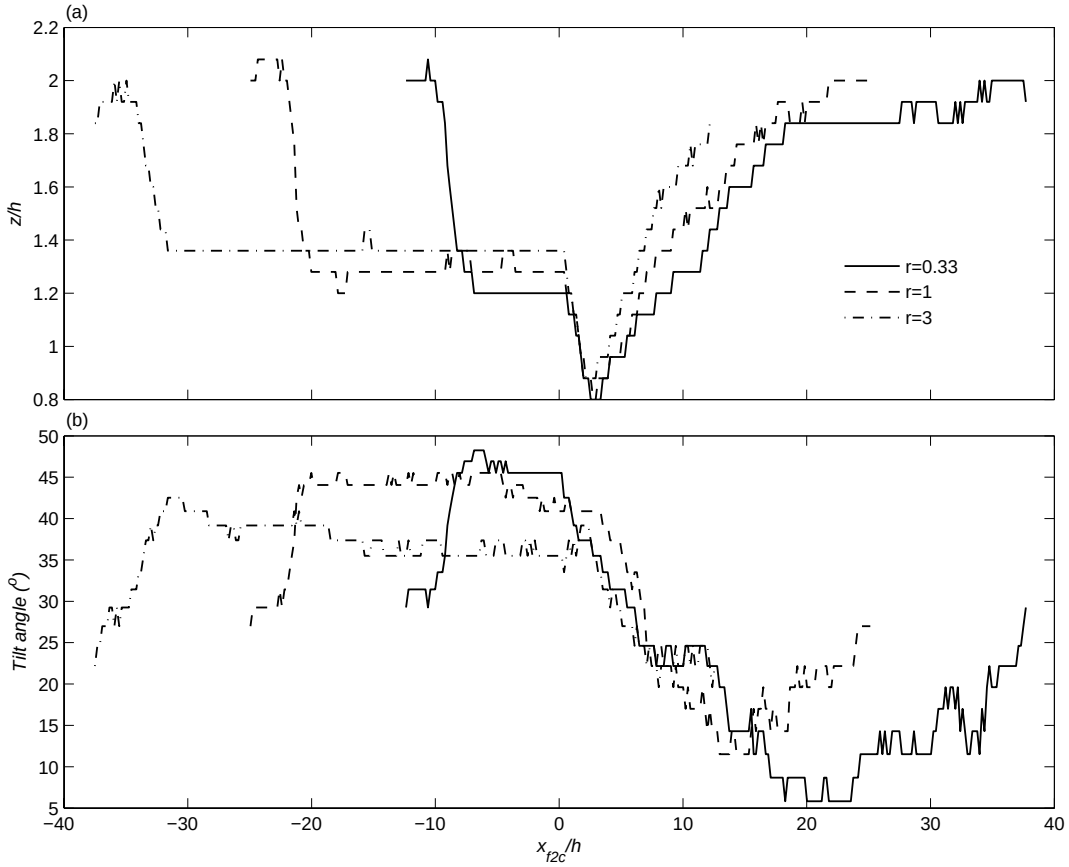

Figure 5.13. (a) Elevations of the zero crossings of v at $r_y/h = 0.2$; (b) Tilt angles of the centres of the counter-rotating vortices in the $y-z$ plane coherent structures, estimated by measuring the elevations of the zero crossings of v at $r_y/h = 0.2$ and $r_y/h = 1.77$

In order to quantify the evolution of the geometry of the coherent structures across vegetation discontinuity, the vertical position of the v zero-crossing z_v at $r_y/h \approx 0.2$ is plotted against x_{f2c} in Figure 5.13a, where z_v is selected as a measure of the vertical position of the vortex pair (another alternative is to use the w zero-crossing) and r_y represents the departure from the centre of the coherent structure in the spanwise

direction. The equilibrium (i.e. at long fetch) value of z_v/h in the canopy area increases from 1.2 to 1.4 as *r* increases from 0.33 to 3. Downstream of the trailing edge of the forest, z_v/h begins to decrease to a minimum of ≈ 0.8 around $x_{f2c}/h = 3$, revealing that the coherent structures move down along with the mean flow. Interestingly, the streamwise location where the minimums of z_v/h take place is consistent with its counterpart for the minimums of $p^{(1)}$ ($x_{f2c}/h \approx 2$ for $r = 0.33$ and 3 and $x_{f2c}/h \approx 4$ for $r = 1$). This consistency implies that the coherent structures keep losing their organization in the readjustment region downstream of the trailing edge, which makes sense as in this region the mean flow interact less with the canopy elements, and the clearing surface, causing the coherent structures to deform. Farther downstream, the mean flow begins to interact with the clearing surface, generating instabilities necessary for maintaining fresh and consistent coherent structures. Consequently, the coherent structures represent a greater fraction of TKE as evidenced by the increase of $p^{(1)}$ and begin to climb until an equilibrium value $z_v/h \approx 1.8$ is reached. This is also in good agreement with the interpretation for Figure 5.3a that an internal boundary layer begins to grow at $x_{f2c}/h \approx 3$, and for Figure 5.6c that the elevation at which $\psi_3^{(1)}$ reaches its peak value is lowest at $x_{f2c}/h \approx 3$. Downstream of the leading edge the vortex pair begins to ascend slightly along with the mean flow until $x_{c2f}/h \approx 1$, and then fall sharply with z_v/h decreasing from ≈ 2 to its equilibrium value over the canopy (i.e. from 1.2 for $r = 0.33$ to

1.4 for $r = 3$). Note that the organization of the coherent structures keeps increasing in the readjustment zone downstream of the leading edge (c.f. Figure 5.8).

The vortex pair also changes its spanwise tilt angle across vegetation discontinuity, as shown in Figure 5.13b. This angle is estimated by measuring the orientation of the line passing the v zero-crossings at $r_x/h \approx 0.2$ and $r_x/h \approx 1.8$. As shown in Huang et al. (2009b), this angle is close to 45 degrees within a homogeneous CSL for varied vegetation densities. Downstream of the trailing edge, it gradually decreases here to ≈ 10 degrees.

5.6 *Conclusions*

In this chapter we have systematically examined the coherent turbulent structures across the forest-to-clearing transition and the clearing-to-forest transition through the use of the POD technique applied to LES results.

The mean flow is characterized by a pronounced downward movement and a recirculation zone above the clearing surface across the forest-to-clearing transition and a strong upward movement across the clearing-to-forest transition. The existence of the recirculation zone implies that there is always a mean flow above the clearing surface advecting toward the forest side regardless of the direction of the driving pressure gradient, which has a significant effect on seed and pollen dispersal (Cassiani et al. 2005; Cassiani et al. 2007).

The vertical movements of the mean flow across the transitions influence the turbulence in these regions directly in the sense that the turbulence downstream of the transitions remains similar to some extent to the turbulence upstream. The results of quadrant analysis reveal that the trend of the sweep-ejection dominance continues immediately downstream of the two transitions. The vertical profiles of the coherent structures immediately downstream of the transitions resemble those upstream of the corresponding transitions. Also, the streamwise vortex pair has been consistently observed across the transitions. However, the turbulence immediately downstream of the transitions also varies significantly from the turbulence upstream. Downstream of the transitions new boundary layers are being formed. The degree of organization of the turbulence, which is described by the percentage that the coherent structures represent of the total TKE, decreases sharply immediately downstream of the trailing edge of the forest as the mean flow drops. Approximately 3*h* downstream of the trailing edge of the forest, the organization of the turbulence begins to be strengthened as the mean flow interacts more with the clearing surface and the coherent structures develop. Immediately downstream of the leading edge of the forest, the organization of the turbulence begins to increase as a result of the formation of Kelvin–Helmholtz instabilities.

Although the streamwise vortex pair has been consistently observed across both the transitions, its morphological features do change as a function of the fetches. Its

height decreases and then increases as it goes farther downstream of the trailing edge of the forest, much as the organization of the turbulence. Downstream of the leading edge of the forest, the height of the vortex pair decreases sharply to its equilibrium value in the canopy area due to the fundamental difference in the formation mechanism of the turbulence in the canopy area and in the clearing area. A larger *r* systematically enhances the height of the vortex pair at the same distance downstream of both transitions.

6 On Scalar Dissimilarity

6.1 *Introduction*

Similarity in turbulent transport of mass (e.g. water vapour and CO_2), heat and momentum is widely assumed in models and interpretation of micro-meteorological measurements. For example, virtually all flux footprint models, which describe the functional relationship between the distribution of a source/sink area of a scalar and the flux of this scalar at a measurement point, assume that all scalars behave similarly (see e.g. Leclerc and Thurtell 1990; Horst and Weil 1992; Vesala et al. 2008; Hsieh and Katul 2009). Moreover, turbulent Schmidt numbers (Prandtl number in case of temperature) are traditionally assumed to be unity under neutral stability conditions (Oke 1987; Garratt 1992), implying the internal mechanism in turbulent scalar transfer is similar to that of turbulent momentum transfer.

However, in the CSL field experiments suggest that scalar similarity is generally violated. The correlation coefficient between two scalars (s_1 and s_2) $r_{s_1 s_2}$ is commonly used as a measure to evaluate the degree to which these two scalars conform to the similarity assumption (e.g. Albertson et al. 1995; Katul et al. 1995; Hsieh et al. 1996; Katul et al. 1996a; Hsieh et al. 2008; Guo et al. 2009). Its value is expected to be ±1 if the assumption of scalar similarity holds perfectly. Field measurements conducted in the CSL do not support scalar similarity, evidenced by significant departures of $r_{q\theta}$ (q for humidity and θ for potential air temperature) (e.g. Katul et al. 1995; Lamaud and Irvine

2006) and r_{cq} (c for CO_2 concentration) (e.g. Scanlon and Sahu 2008; Thomas et al. 2008) from ±1. Also, the Prandtl number is often found to be as low as 0.5 within the CSL (Raupach and Thom 1981; Raupach et al. 1996; Harman and Finnigan 2008). De Bruin et al. (1999), Cava *et al.* (2008), and Katul *et al.* (2008) reviewed the causes for the dissimilarity between q and θ and concluded that heterogeneity in the sources/sinks of scalars is a common one in addition to the influence of entrainment and non-steadiness of the data analyzed (though the latter two influences cannot be readily disentangled using single point measurements). Williams *et al.* (2007) investigated how variations in surface heterogeneity induced by seasonal changes affect the extent to which the application of Monin-Obukhov similarity theory (MOST) is weakened in the CSL and concluded that senescence exacerbates the violation of MOST applied to the CSL and also degrades correlations between scalars across a wide range of eddy sizes due to production of heterogeneity in scalar sources/sinks.

Large-scale coherent structures have been shown to contribute to the majority of the scalar and momentum fluxes across the canopy-atmosphere interface (e.g. Gao et al. 1989; Katul et al. 1998; Finnigan and Shaw 2000; Thomas and Foken 2007), thereby potentially 'encoding' significant information about the production term in the scalar-scalar source-sink dissimilarity. Our hypothesis is that their geometric attributes and their coupling to the source-sink scalar distribution can explain the onset and degree of this dissimilarity. If these coherent structures are large and tightly coupled to scalar

sources or sinks, then they are likely to imprint any scalar-scalar source dissimilarity originating from within the canopy onto micro-meteorological measurements in the CSL. To test this hypothesis, a large-eddy simulation (LES) model is used with carbon, water and heat exchange included along with all key canopy biophysical considerations to estimate scalar sources and sinks inside the canopy volume. The proper orthogonal decomposition (POD) technique is conducted to quantitatively educe the 3D coherent structures following the approach of Huang et al. (2009a, b, 2010). The role of these coherent structures in explaining scalar dissimilarity is then examined with a focus on the following research questions: (1) To what extent is the dissimilarity in the source-sink profiles of the scalars reflected in the geometric attributes of the coherent structures? (2) To what extent is the dissimilarity of turbulent Schmidt numbers from unity potentially explained in terms of the degree of organization of coherent structures? (3) To what extent do the coherent structures describe other major characteristics connected with the sweep-ejection cycle in the scalar and momentum transport?

6.2 *Scaling Analysis*

Consider two scalars s_1 and s_2 (e.g. from c, q and θ) emitted from sources (or removed by sinks) in a stationary and horizontally homogeneous mean canopy flow. The budget equation for their covariance $\langle s_1' s_2' \rangle_{xyt}$ without subsidence and for stationary conditions is expressed as (see Stull 1988; Garratt 1992; Katul et al. 2009),

$$\frac{\partial\langle s_1's_2'\rangle_{xyt}}{\partial t} = 0$$

$$= \underbrace{-\left(\langle w's_1'\rangle_{xyt}\frac{\partial\langle s_2\rangle_{xyt}}{\partial z} + \langle w's_2'\rangle_{xyt}\frac{\partial\langle s_1\rangle_{xyt}}{\partial z}\right)}_{\mathbf{I}} \quad \underbrace{-2\varepsilon_{s_1s_2}}_{\mathbf{II}} \quad \underbrace{-\frac{\partial\langle w's_1's_2'\rangle_{xyt}}{\partial z}}_{\mathbf{III}}, \tag{6.1}$$

where $\langle\ \rangle_{xyt}$ represents a temporal and horizontal average and the prime implies a departure from this average, Term I is the production term, Term II is the dissipation term and Term III is the turbulent transport term.

6.2.1 Functional relationship between $\langle s_1's_2'\rangle_{xyt}$ and sources/sinks

To illustrate the basic connection between vegetation sources/sinks to $\langle s_1's_2'\rangle_{xyt}$, we employ standard closure models for the dissipation which is written as:

$$\varepsilon_{s_1s_2} = \frac{Q}{\lambda_3}\langle s_1's_2'\rangle_{xyt}, \tag{6.2}$$

and the transport term written as

$$\langle w's_1's_2'\rangle_{xyt} = -Q\lambda_1\frac{\partial\langle s_1's_2'\rangle_{xyt}}{\partial z}, \tag{6.3}$$

where $Q = \langle u_i'u_i'\rangle_{xyt}^{1/2}$ is the square root of the turbulent kinetic energy, $\lambda_1 = a_1 l_m$ and $\lambda_3 = a_3 l_m$ with l_m being the mixing length inside the canopy and a_1 and a_3 two constants (Finnigan and Belcher 2004; Katul et al. 2006b; Katul et al. 2009). Substituting (6.2) and (6.3) into (6.1), we obtain a second-order ordinary differential equation (ODE) for $\langle s_1's_2'\rangle_{xyt}$:

$$\lambda_1 Q \frac{\partial^2 \langle s_1' s_2' \rangle_{xyt}}{\partial z^2} + \lambda_1 \frac{\partial Q}{\partial z} \frac{\partial \langle s_1' s_2' \rangle_{xyt}}{\partial z} - \frac{2Q}{\lambda_3} \langle s_1' s_2' \rangle_{xyt} = \langle w' s_1' \rangle_{xyt} \frac{\partial \langle s_2 \rangle_{xyt}}{\partial z} + \langle w' s_2' \rangle_{xyt} \frac{\partial \langle s_1 \rangle_{xyt}}{\partial z}. \quad (6.4)$$

The mathematical properties of this ODE were studied elsewhere (Katul et al. 2009) and we only provide a brief overview of the pertinent findings relevant to the three questions here. Equation (6.4) suggests that the pertinent dynamical variables describing the profile of $\langle s_1' s_2' \rangle_{xyt}$ include a 'geometric' length scale connected with eddy sizes (=l_m), a velocity scale connected with the local TKE (=Q), and the strength of the interaction between the local fluxes of one scalar and the mean concentration gradient of the other.

The general solution to equation (6.4) can be described by a super-position of a homogeneous solution and a particular solution. The homogeneous solution (i.e. derived by setting the right-hand side to zero) is generally dissipative and primarily describes how $\langle s_1' s_2' \rangle_{xyt}$ introduced at some arbitrary level within the CSL is transported and dissipated within the canopy. Its properties are only dependent on the flow statistics, including the vertical variation of Q. The particular solution is primarily connected to the finite value of the non-homogeneous term (i.e. the right-hand side) and represents the main production term for $\langle s_1' s_2' \rangle_{xyt}$. To link the properties of the main production to canopy sources and sinks, consider the most idealized case - which links

gradients to their corresponding fluxes using a standard first-order closure approach. This linkage leads to

$$\frac{\partial\langle s_1\rangle_{xyt}}{\partial z} = -\frac{\langle w' s_1'\rangle_{xyt}}{K_{s_1}};\ \ \frac{\partial\langle s_2\rangle_{xyt}}{\partial z} = -\frac{\langle w' s_2'\rangle_{xyt}}{K_{s_2}}, \tag{6.5}$$

where K_{s_1} is the turbulent diffusivity for scalar s_1 and K_{s_2} the turbulent diffusivity for scalar s_2. Also, K_{s_1} and K_{s_2} are related to their corresponding Schmidt numbers Sc_1 and Sc_2 by,

$$K_{s_1} = \frac{Sc_1}{K_\tau};\ \ K_{s_2} = \frac{Sc_2}{K_\tau}, \tag{6.6}$$

where K_τ is turbulent momentum diffusivity defined as

$$K_\tau = -\frac{\langle u' w'\rangle_{xyt}}{\partial\langle u\rangle_{xyt}/\partial z}. \tag{6.7}$$

Then, the turbulent fluxes are related to the sources/sinks using the mean scalar continuity equation for chemically non-reactive scalars:

$$\langle w' s_1'\rangle_{xyt}(z) = F_1(0) + \int_0^z S_1(z)dz;\ \ \langle w' s_2'\rangle_{xyt}(z) = F_2(0) + \int_0^z S_2(z)dz, \tag{6.8}$$

where $F_1(0)$ is the flux of s_1 at z = 0 (taken as the ground or forest floor) and $S_1(z)$ is the vertical profile of the source/sink strength of s_1 (sink implies $S_1 < 0$) and, similarly for s_2. Substituting (6.5) and (6.8) into (6.4) results in a second-order ODE for $\langle s_1' s_2'\rangle_{xyt}$ in terms of source/sink profiles as well as Schmidt numbers:

$$\frac{\partial^2 \langle s_1' s_2' \rangle_{xyt}}{\partial z^2} + \frac{1}{Q}\frac{\partial Q}{\partial z}\frac{\partial \langle s_1' s_2' \rangle_{xyt}}{\partial z} - \frac{2}{\lambda_1 \lambda_3}\langle s_1' s_2' \rangle_{xyt}$$

$$= -\frac{1}{\lambda_1 Q}\left(\frac{1}{K_{s_1}} + \frac{1}{K_{s_2}}\right)\left(\left(F_1(0) + \int_0^z S_1(z)dz\right)\left(F_2(0) + \int_0^z S_2(z)dz\right)\right) \qquad (6.9)$$

$$= -\frac{1}{\lambda_1 Q}\left(\frac{K_\tau}{Sc_1} + \frac{K_\tau}{Sc_2}\right)\left(\left(F_1(0) + \int_0^z S_1(z)dz\right)\left(F_2(0) + \int_0^z S_2(z)dz\right)\right).$$

Note here that the ground fluxes and the *integrated* sources and sinks play a major role in the production term of $\langle s_1' s_2' \rangle_{xyt}$. Having established a simplified connection between $\langle s_1' s_2' \rangle_{xyt}$ and the integrated scalar sources and sinks, we now proceed to show similar linkages between $\langle s_1' s_2' \rangle_{xyt}$ and the key attributes of the coherent structures.

6.2.2 Functional relationship between $\langle s_1' s_2' \rangle_{xyt}$ and the sweep-ejection cycle

As earlier noted, since the central topic of this paper is about the role of the coherent structure on scalar dissimilarity and since the sweep-ejection cycle can be considered as the 'fingerprint' of the coherent structure, we are also interested in an expression relating $\langle s_1' s_2' \rangle_{xyt}$ and the sweep-ejection cycle. Toward this end, the turbulent flux $\langle w' s' \rangle_{xyt}$ can be written in the following form under steady state and horizontally homogeneous mean conditions (Wilson 1989; Cava et al. 2006):

$$\left\langle w's' \right\rangle_{xyt} = \frac{\tau}{C_4}\left(-\left\langle w'w' \right\rangle_{xyt} \frac{\partial \left\langle s \right\rangle_{xyt}}{\partial z} - \frac{\partial \left\langle w'w's' \right\rangle_{xyt}}{\partial z} + \frac{4}{3}\frac{g}{\left\langle \theta \right\rangle_{xyt}} \left\langle \theta's' \right\rangle_{xyt} \right), \tag{6.10}$$

where C_4 is a closure constant and τ is a Eulerian relaxation time scale (Raupach 1989a, b; Massman and Weil 1999; Poggi et al. 2004a; Cava et al. 2006; Poggi et al. 2006). And, using an incomplete third-order cumulant expansion method (CEM) originally proposed by Katul et al. (1997a), the triple moment $\left\langle w'w's' \right\rangle_{xyt}$ can be linked to the sweep-ejection cycle by (Cava et al. 2006),

$$\left\langle w'w's' \right\rangle_{xyt} = \left(\frac{2\sqrt{2\pi}}{\gamma} \right) \sigma_w \left\langle w's' \right\rangle_{xyt} \Delta S_0 , \tag{6.11}$$

where γ is a constant, σ_w is the standard deviation of the vertical velocity and ΔS_0 is a measure commonly used to quantify the relative importance of sweeps to ejections (Raupach 1981), defined as

$$\Delta S_0 = \frac{\left\langle w's' \right\rangle_{xyt} |_{\text{sweeps}} - \left\langle w's' \right\rangle_{xyt} |_{\text{ejections}}}{\left\langle w's' \right\rangle_{xyt}} . \tag{6.12}$$

Here the sweeps and ejections of $\left\langle w's' \right\rangle_{xyt}$ are determined using standard quadrant analysis classification. Four quadrants are identified through the combination of the signs of s' (abscissa) and w' (ordinate). Although ΔS_0 is originally defined for stress, we extend the definitions of sweep and ejection to scalar transport with the quadrants of sweep and ejection being dependent on the sign of the local flux. For positive local fluxes (e.g. latent heat flux and sensible heat flux in the entire CSL and CO_2

flux near the ground) the sweeps are in quadrant III and ejections in quadrant I. The opposite is true for negative local fluxes (e.g. CO_2 flux in upper canopy and above). Note that expression (6.11) illustrates how the flux-transport term (often the term leading to non-local transport and failure of K-theory for the mean flow) scales with the ejection-sweep properties.

The analysis described above provides a simplified yet analytical framework of how the coherent structures, manifesting themselves in the sweep-ejection cycle, affect scalar covariance.

6.3 *Basic Flow and Scalar Statistics*

In this section, we present the simulation results of three cases with varying LAI values and discuss the effects of the coherent structure on scalar dissimilarity and scalar-momentum transport dissimilarity. We present the basic flow (velocity) statistics to examine the general validity of the LES runs vis-à-vis well known properties of CSL turbulence. Then, we demonstrate the profiles of source/sink strength and other basic scalar statistics and the effects of increasing vegetation density on them. The dissimilarities across scalars and scalar/momentum fluxes are analyzed quantitatively using global measures including scalar-scalar correlations and turbulent Schmidt numbers as well as local measures such as the role of the sweep-ejection cycle on scalar and momentum transfers, respectively. Furthermore, the geometry of the 3D coherent structure incorporating both velocity components and scalars is revealed and the

dissimilarity in the geometric features of different scalars in the coherent structure is then connected to scalar dissimilarity exhibited in the original flow field. The contribution of the coherent structure to scalar dissimilarity is quantified by comparing the results of scalar-scalar correlation, turbulent Schmidt numbers and ΔS_0 for the coherent structure and the original field, respectively.

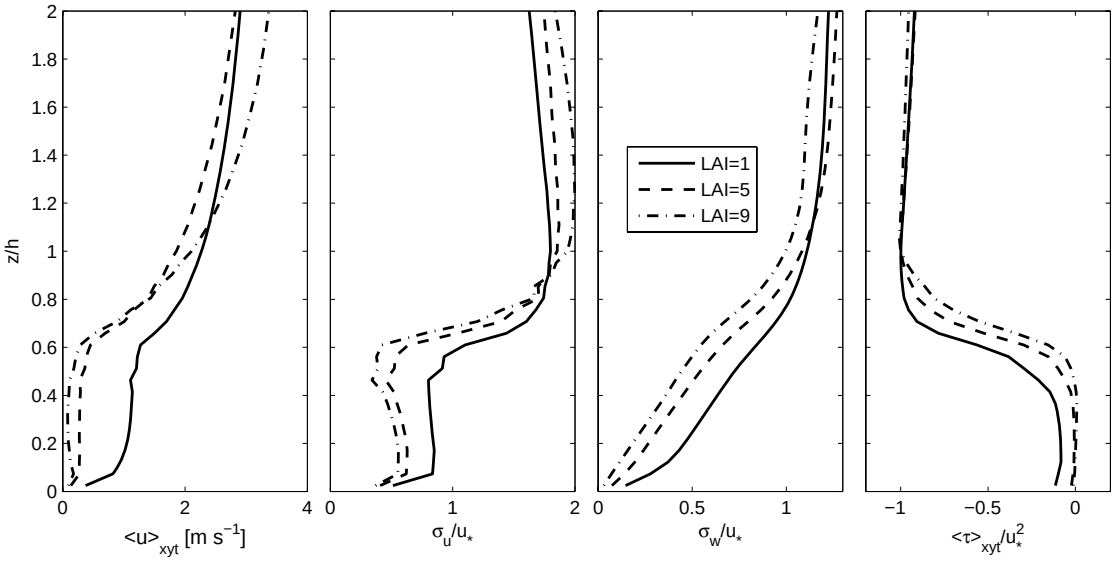

Figure 6.1. Vertical profiles of temporal and horizontal mean streamwise velocity $\langle u \rangle_{xyt}$, normalized standard deviation of mean streamwise velocity σ_u / u_*, normalized standard deviation of vertical velocity σ_w / u_* and normalized stress $\langle \tau \rangle_{xyt} / u_*^2$ (from left to right)

To establish the general validity of the LES experiments, we first show the basic flow velocity statistics for LAI = 1, 5 and 9 in Figure 6.1, including the temporal and horizontal mean streamwise velocity $\langle u \rangle_{xyt}$, the normalized *u* standard deviation σ_u / u_*, the normalized w standard deviation σ_w / u_*, and the normalized total stress $\langle \tau \rangle_{xyt} / u_*^2$,

where τ represents the sum of the resolved stress and the subgrid scale (SGS) stress and $u_* = \left|\langle \tau \rangle_{xyt}\right|_{z=h}^{1/2}$. As expected, an increase in LAI results in a decreased $\overline{u}$ in the lower canopy; however, above the canopy there is a tendency of increasing (normalized) wind speed with increasing LAI, which is due to a 'skimming effect' noted by Albertson et al. (2001). The values of σ_u/u_* and σ_w/u_* (e.g. σ_u/u_* is around 2 and σ_w/u_* is around 1 at the canopy top) are consistent with previous results obtained from numerical (e.g. Huang et al. 2009b) and wind-tunnel (e.g. Brunet et al. 1994) experiments. The small profile irregularities around $z/h = 0.6$ in the profiles of $\langle u \rangle_{xyt}$ and σ_u/u_* are attributed to the primary peak in the vertical canopy structure (c.f. Huang et al. 2009b). Furthermore, Figure 2 also illustrates major differences in how the canopy attenuates the profiles of σ_u/u_* and σ_w/u_*. The LES results are suggestive that deep inside the canopy, there is significant σ_u/u_* (due to turbulence originating well above the canopy), while σ_w/u_* is significantly attenuated, consistent with a number of field experiments (e.g. Katul and Chang 1999; Poggi et al. 2004b). These results are suggestive that the TKE remains significant inside the canopy even for the largest LAI due to eddies produced above the CSL and these eddies do not contribute much to vertical velocity fluctuations.

In Figure 6.2, we present the normalized vertical profiles of the mean scalar $\left(\langle s \rangle_{xyt} - s_0\right)/s_*$, the scalar sources and sinks $\langle S_s \rangle_{xyt} h/(u_* s_*)$, the scalar flux

$\langle w's' \rangle_{xyt} / (u_* s_*)$ and the scalar variance $\langle s'^2 \rangle_{xyt} / s_*^2$, where $s_0 = \langle s \rangle_{xyt} |_{z=h}$, and $s_* = \langle w's' \rangle_{xyt} |_{z=h} / u_*$ for $s = c, q, \theta$ and LAI = 1, 5 and 9. The general agreement in the mean concentration profiles and the source-sink profiles of CO_2 across the three cases of varying vegetation density indicates the approximate linear relationship between the local net CO_2 uptake rate and the local LAD. However, there is also a minor difference among the source-sink profiles of different LAIs in the sense that the strength increases with LAI above the primary peak of LAD but decreases with LAI below. This is due to the dependence of the local net CO_2 uptake rate on the photosynthetically active radiation (PAR) availability, which becomes more vertically inhomogeneous as LAI increases with a higher fraction intercepted in the upper canopy layers and less in the sub-canopy (Albertson et al. 2001). A constant CO_2 source strength of 2 μmol m^{-2} s^{-1} was assigned at the ground to account for the soil and forest floor respiration. However, the relative importance of this CO_2 source to the integrated CO_2 flux decreases with increasing LAI, as shown in the near-ground portion of the source-sink profile and the flux profile.

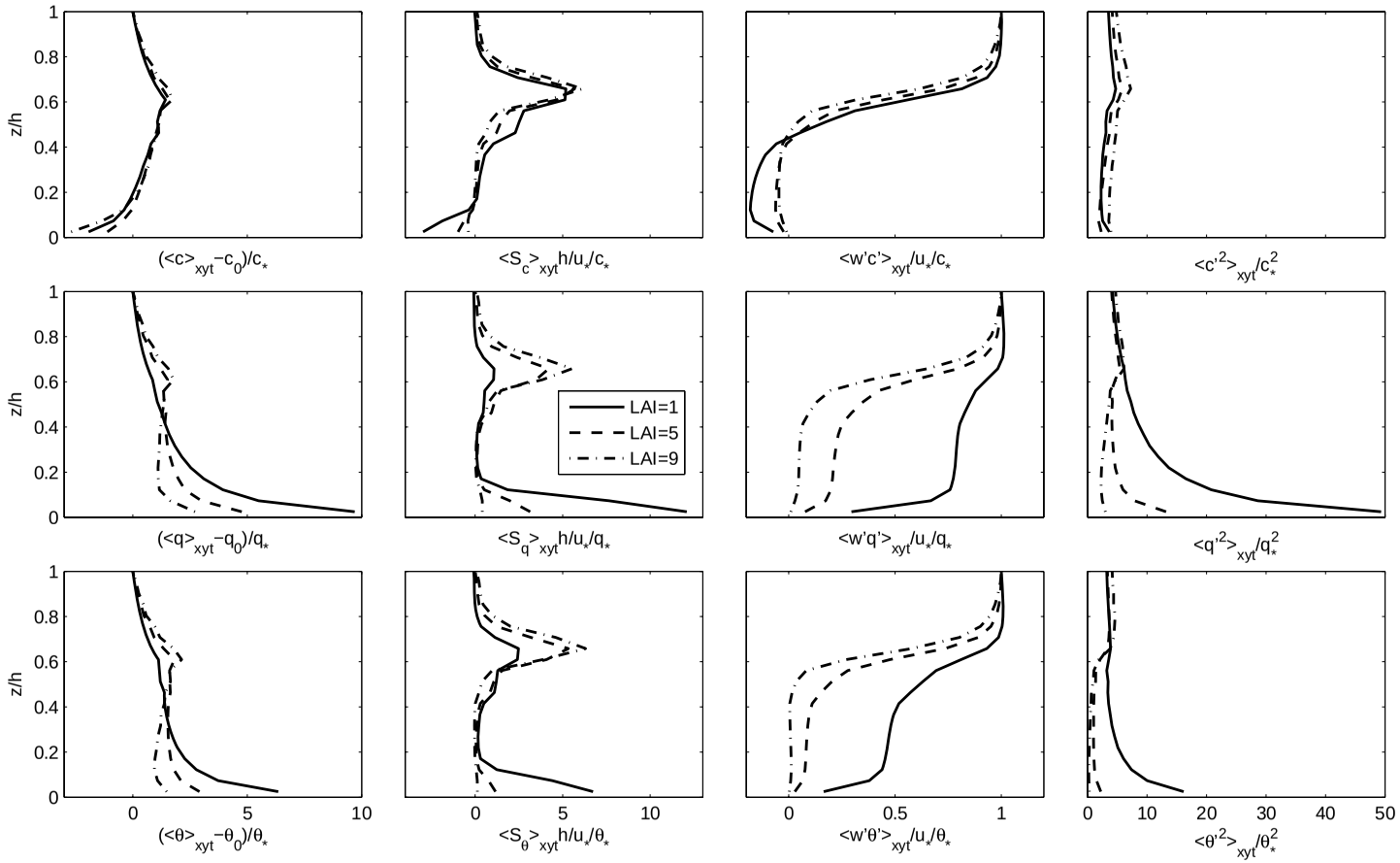

Figure 6.2. Vertical profiles of normalized mean scalar, scalar source/sink, vertical flux and variance for CO_2 concentration c (top row), water vapour concentration q (middle row) and air temperature θ (bottom row), respectively

The major difference of the source-sink profiles between c, q, θ is that the canopy and the soil sources/sinks are of opposite signs for c (canopy as a sink and soil as a source) but of identical signs for q and θ (both as sources). As expected, the vegetation density has significant effects on the source profiles of the latent and sensible heat fluxes. The source strength at the soil-atmosphere interface decreases while the source strength inside the canopy increases with increasing LAI as a result of canopy radiation interception. This results in the ground being the dominant source for the latent and sensible heat fluxes for LAI = 1 and the canopy dominating for LAI = 5 and 9. Consequently, as the canopy becomes denser, the normalized variance generally increases for c inside the canopy and decreases for q and θ from the ground up to around the primary peak of LAD. Note that for any given LAI the ground is relatively more important (than the canopy) as a source of the latent heat flux than of the sensible heat flux: the ratio of the strength between the ground source strength and that at the primary peak of LAD for LAI = 1 is 11.2 for the latent heat flux but only 2.7 for the sensible heat flux. An examination of the mean temperature profile reveals the existence of an unstable stratification throughout the canopy for LAI = 1, whereas there is a deep stable layer (albeit a weak one) for the LAI=9 case with its strong elevated heat source. The normalized variance of CO_2 concentration generally increases with higher vegetation density inside the canopy. Given the sensitivity of the individual scalar variances to LAI variations and given how different these normalized variances are for

various scalars and LAI values, the addition of scalar variance in the POD analysis (i.e. β_2) does achieve extra information about the coupling between the flow and the vegetation beyond what can be achieved by the traditional TKE approach (i.e. β_1), which is predominantly controlled by σ_u/u_*, and hence eddies not locally within the canopy volume.

With these apparent contrasts in the scalar source/sink and scalar variance profiles, and with the variability occurring on a length scale and position overlapping with canopy coherent structures, one might expect scalar dissimilarity to arise.

6.4 *Scalar Dissimilarity in the Original Field*

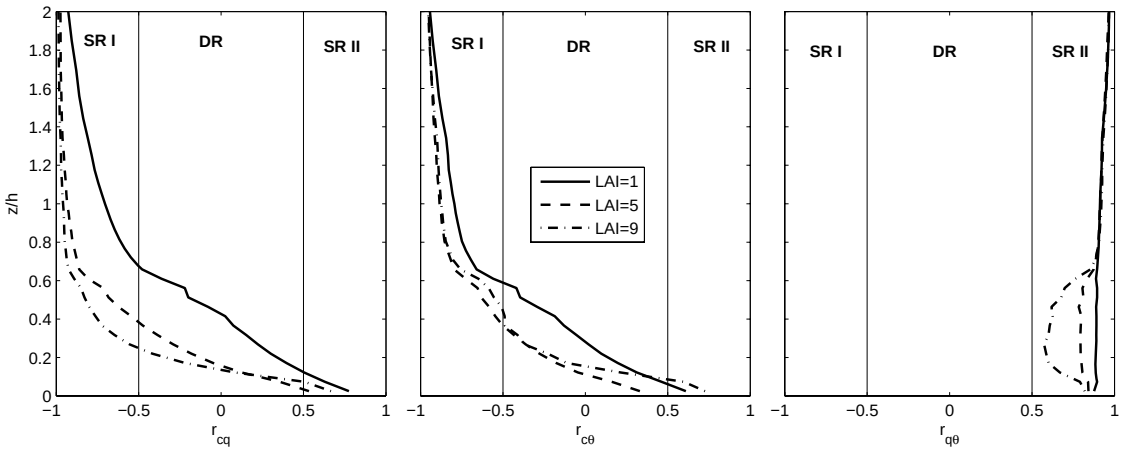

Figure 6.3. Vertical profiles of correlation coefficients r_{cq}, $r_{c\theta}$ and $r_{q\theta}$ (from left to right). SR I, DR, SR II stand for similarity region I, dissimilarity region, similarity region II, respectively

One measure often used to quantify scalar similarity between two scalars (s_1 and s_2) is the correlation coefficient $r_{s_1 s_2}$, which is defined as

$r_{s_1 s_2} = \langle s_1' s_2' \rangle_{xyt} \Big/ \left(\langle s_1'^2 \rangle_{xyt}^{1/2} \langle s_2'^2 \rangle_{xyt}^{1/2} \right)$ and has an expected value of ±1 for strictly similar scalars. Figure 6.3 shows the profiles of r_{cq}, $r_{c\theta}$ and $r_{q\theta}$ for the three LAI cases. We split the vertical range of the CSL (i.e. $z/h \subset [0, 2]$) into three conceptual regions in accordance with the ranges of the value of $r_{s_1 s_2}$, i.e., similarity region I for $-1 \le r_{s_1 s_2} < -0.5$, dissimilarity region for $-0.5 \le r_{s_1 s_2} < 0.5$ and similarity region II for $0.5 \le r_{s_1 s_2} \le 1$. Both r_{cq} and $r_{c\theta}$ cover all the three regions. It is clear that the formation of similarity region I is mainly due to the role of the canopy acting as a sink of CO_2 but a source of water vapour and sensible heat flux. For *c-q* and *c-*θ there is a shallow zone of similarity region II near the soil surface, arising because of the soil being a source of all three scalars. The combined effects of the canopy and the soil act to degrade the modulus of r_{cq} and $r_{c\theta}$, therefore leading to strong scalar dissimilarity inside the canopy between these two similarity regions. Similarity region I of r_{cq} extends deeper into the canopy for the denser cases because the processes of transpiration and photosynthesis inside the canopy are primarily stomatally regulated, which couples tightly the carbon source and the water sink profiles in the canopy. We should note that if the inter-cellular to ambient CO_2 concentration was approximately constant throughout the canopy depth, then the stomatal regulation of both scalars would be complete. However, the biochemical processes controlling photosynthesis, and their switch from temperature to light limitations leads to some CO2 regulation above and beyond the stomatal

regulation. Although $r_{q\theta}$ is in similarity region II for the entire CSL under all three LAI cases, the strength of the similarity decreases with increasing LAI approximately below the primary peak of LAD with $r_{q\theta} \approx 0.9$ for LAI = 1 and $r_{q\theta} \approx 0.6$ at $z/h \approx 0.2$ for LAI = 9. This reduction in $r_{q\theta}$ for the high LAI case is expected given that the sources of water vapour and heat from the soil surface are relatively weak.

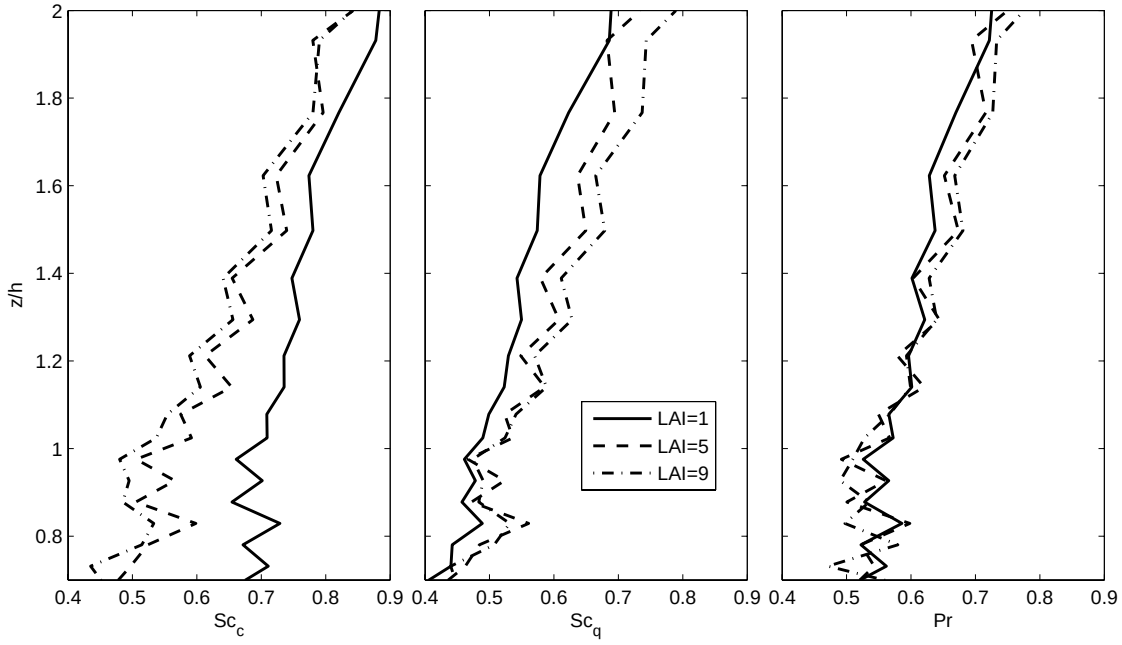

Figure 6.4. Vertical profiles of turbulent Schmidt number for *c*, *q* and θ (Prandtl number) (from left to right)

In Figure 6.4, we present the vertical profiles of the turbulent Schmidt number Sc (Prandtl number for temperature) for each LAI and scalar (c.f. equation (6.6)). Note that the total momentum and scalar transport (i.e. the sum of the resolved and SGS fluxes) are used to calculate Sc. The Sc is only shown in the vertical range of $z/h \subset [0.7, 2]$ because below $z/h = 0.7$ Sc exhibits large perturbations due to the

vanishingly small amplitude of turbulent diffusivities. Sc generally ranges from 0.4 to 0.9, which is consistent with the values reported in the literature (e.g. Koeltzsch 2000; Flesch et al. 2002). There is a clear dependence of Sc on height for all three scalars, which agrees with the conclusion drawn from the wind tunnel experiment in Koeltzsch (2000) and are probably caused by coherent structure transporting scalars in a more local manner than the momentum (Koeltzsch 2000). Likewise, these values are consistent with Harman and Finnigan (2008) – who reported Sc values as low as 0.5 for a number of forest stands. The dissimilarity in the source-sink profile has a significant impact on Sc as evidenced by Sc_c being greater than Sc_q for the case of LAI=1 but of similar magnitude for the case of LAI=9. This is in accordance with the previous recognition by Raupach (1988) that the turbulent diffusivity are strongly influenced by the source/sink distribution of the scalar under consideration, and can be understood in the context of Figure 6.2: note for LAI=1 now the relatively strong ground source causes Sc_q to differ greatly from Sc_c. Since the relative importance of the contribution of the ground surface decreases in the source-sink profile of carbon and water with increasing LAI, Sc_c and Sc_q tend to converge to one another with increasing LAI. Finally, Pr appears insensitive to LAI, which may appear to be a puzzling result. One plausible explanation here is that in the upper layers and above the canopy, the scalar flux budget in eq. (6.10) reduces to an approximate balance between production and dissipation terms that can be written as

$$1-\frac{4}{3}\frac{g}{\langle\theta\rangle_{xyt}}\frac{\langle\theta' s'\rangle_{xyt}}{\langle w' s'\rangle_{xyt}}\frac{\mu}{C_4}\approx-\left(\langle w' w'\rangle_{xyt}\frac{\mu}{C_4}\right)\left(\frac{1}{\langle w' s'\rangle_{xyt}}\frac{\partial\langle s\rangle_{xyt}}{\partial z}\right)\approx\left(\langle w' w'\rangle_{xyt}\frac{\mu}{C_4}\right)\frac{1}{K_s}, \quad (6.13)$$

thereby yielding

$$K_s\approx\frac{\left(\langle w' w'\rangle_{xyt}\frac{\mu}{C_4}\right)}{1-\frac{4}{3}\frac{g}{\langle\theta\rangle_{xyt}}\frac{\langle\theta' s'\rangle_{xyt}}{\langle w' s'\rangle_{xyt}}\frac{\mu}{C_4}}. \quad (6.14)$$

For temperature, $\langle\theta' s'\rangle_{xyt}$ becomes $\langle\theta'^2\rangle_{xyt}$ and $\langle w' s'\rangle_{xyt}$ becomes $\langle w'\theta'\rangle_{xyt}$, and noting the insensitivity in the relationship between $\langle\theta'^2\rangle_{xyt}$ and $\langle w'\theta'\rangle_{xyt}$ to LAI variations (see Figure 6.2) leads to a denominator in K_θ far less sensitive to LAI variations or any potential dissimilarities in scalar sources and sinks when compared to the other two scalars.

Figure 6.5 presents an analysis of the sweep-ejection cycle using ΔS_0 to measure the relative importance of sweeps to ejections across the vertical range $z/h\subset[0.7, 2]$. This analysis was performed using only the resolved w and scalars, which is reasonable because the resolved momentum and scalar fluxes generally capture over 98% of their corresponding total fluxes in the designated range. The results of ΔS_0 are shown in comparison with previous findings from a flume experiment (Poggi et al. 2004b), field experiments in a pine forest (Katul and Albertson 1998) and in a mixed coniferous forest (Cava et al. 2006). ΔS_0 for momentum is in a good agreement with the flume result while

being generally smaller than the field experiments, which are probably due to the difference of the drag coefficients used in our LES from the actual value in field.

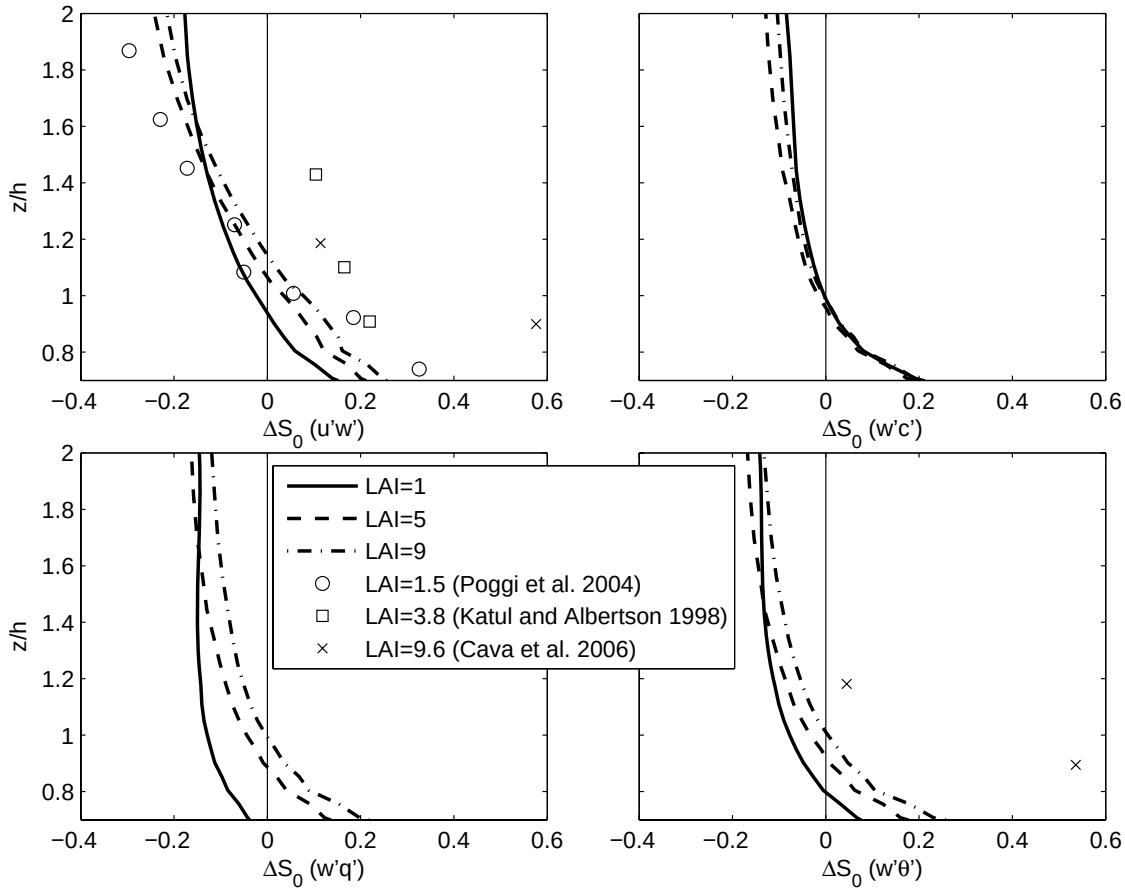

Figure 6.5. Vertical profiles of ΔS_0 for momentum and scalar fluxes. Note that for momentum and w'c', ΔS_0 is calculated as the difference between Quadrant IV and Quadrant II; however, for w'q' and w'θ' it is between Quadrant III and Quadrant I

As vegetation density increases, sweeps tend to be more important than ejections for $z/h < 1.5$, which was shown to reflect the elevation of the coherent structure (Huang et al. 2009b). In fact, these LES results are consistent with a scaling analysis similar to the one reported in equation (6.11), which was shown by Poggi et al. (2004a) to yield:

$$\Delta S_0 = -\frac{Q}{\langle u'w' \rangle_{xyt}} \frac{1}{2\sqrt{2\pi}} \left(\frac{1}{\sigma_u} \frac{\partial \sigma_u^2}{\partial z} - \frac{1}{\sigma_w} \frac{\partial \langle u'w' \rangle_{xyt}}{\partial z} \right). \quad (6.15)$$

Because $\partial \sigma_u^2 / \partial z > 0$ for the region of interest (though not the entire vertical domain), and $\frac{\partial \langle u'w' \rangle_{xyt}}{\partial z} \approx C_d a \langle u \rangle_{xyt}^2$, increasing $C_d a$ (or the inverse of the adjustment length scale) leads to a ΔS_0 that becomes 'elevated' with height with sweeps becoming the dominant mode of momentum transport (i.e. ΔS_o becoming progressively negative) as evidenced by the profiles in Figure 6.1.

Comparatively, ΔS_0 for scalar transport is more influenced by the local source/sink than momentum transport because the values of ΔS_0 are more stable above the canopy for scalars than for momentum. LAI has a noticeable influence on ΔS_0 of water vapour and heat transport, while appearing notably less influential on ΔS_0 of CO_2 transport. This is probably caused by the role of the ground surface emitting both water vapour and heat, which are transferred to around and above the canopy top by coherent eddies with diameters of approximately one half of the canopy height (Scanlon and Albertson 2001). This portion of air flow then reinforces ejection motions of latent heat flux and sensible heat flux. Since the relative importance of the source/sink at the ground level decreases with increasing LAI, ΔS_0 tends to increase for q and θ with increasing LAI.

6.5 *Scalar Dissimilarity in the Coherent Structures*

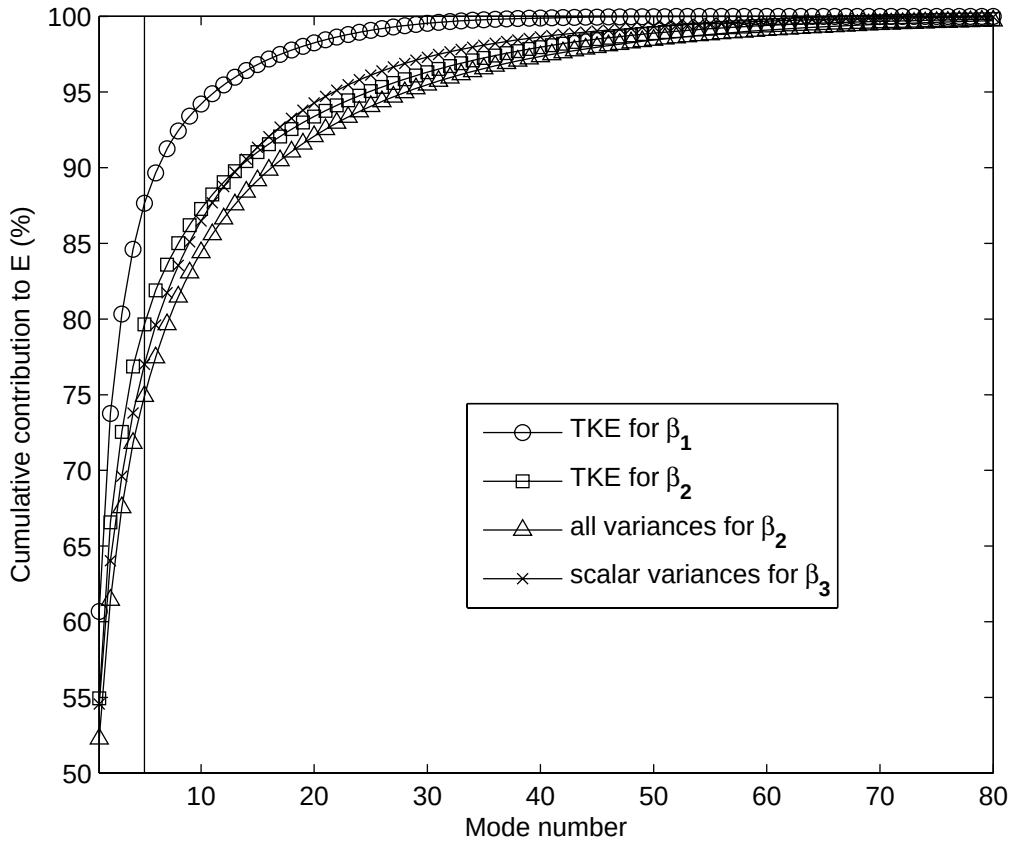

Figure 6.6. Cumulative contribution to the integrated sum of variance of the POD modes for three cases: in the first case β_1 only three velocity components are incorporated while both velocity components and three scalars are included in the second case β_2. The third case β_3 contains only the scalars. The vertical line indicates the results for 5 modes. The case of LAI=5 is used to produce all the results

We now proceed to explore the effects of the coherent structures on the observed dissimilarity. First, we show the overall importance of the coherent structures in capturing the resolved TKE and scalar variances as well as momentum and scalar fluxes. Then, we describe the geometric attributes of these coherent structure using velocity

components and flux contribution. Finally, the scalar dissimilarity captured by the coherent structure is quantitatively compared with that in the original field through the use of scalar-scalar correlations, turbulent Schmidt numbers and the ability of the coherent structure in reproducing the sweep-ejection cycle.

Figure 6.6 shows the cumulative contribution to E (i.e. $\sum_{n=1}^{p} \Lambda^{(n)} \Big/ E$, see equation (2.38)) of the eigenmodes. Note that TKE converges faster in β_1 than in β_2 because the structures educed on β_2 are optimal in the sense of both velocity components and scalars, thereby degrading the optimization of TKE (in isolation) to some extent. However, the coherent structures (i.e. the first eigenmode) obtained through β_2 still describes approximately 55 percent of the total TKE, only 5 percent less than the optimum value obtained through β_1. Overall, the coherent structure describes approximately 52 percent of the sum of all the integrated variances, which equally represent the TKE and scalar variances. Scalar variances in β_3 converge slower than TKE in β_1 with the leading mode capturing ≈55 percent of the total scalar variances, suggesting that the coherency in terms of scalars in the coherent structure is weaker than in velocity components. The convergence rate for all variances in β_2 is close, although slightly lower, to scalar variances in β_3, indicating that the leading modes in terms of velocities in β_1 tightly tie to those in terms of scalars in β_3. In addition to the contribution to the variances, we investigate the percentage contribution of the coherent

structures to the overall vertical fluxes of momentum and scalars (i.e. the covariance) $p_{\beta_i\beta_j}$ in Figure 6.7, where $p_{\beta_i\beta_j}$ is defined as,

$$p_{\beta_i\beta_j} = \frac{\left\langle \beta_i^{(1)} \beta_j^{(1)} \right\rangle_{xyt}}{\left\langle \beta_i \beta_j \right\rangle_{xyt}}, \quad (i \neq j), \tag{6.16}$$

where $\beta_i^{(1)}$ is the reconstructed field described by the coherent structures (c.f. (2.36) and (2.37)). The percentage of the contribution of the coherent structure generally ranges from around 60 to over 100, much larger than that for the variances. This is because the incoherent components of the turbulent series can be uncorrelated, thus contributing only a very small amount to the covariances. However, these components still contribute a significant portion to the variance irrespective of the lack of inter-variable correlation (e.g. σ_u^2). The percentage contribution can be over 100 because the variance-oriented optimization of the POD procedure does not capture the covariance in a monotonic way. Other modes could have small contributions of opposite sign. The percentage for the three scalar fluxes generally peaks at or just above the canopy top, indicating the region where the contribution of the coherent structure to the vertical scalar transport is most dominant. However, $p_{u'w'}$ peaks noticeably higher (at $z/h \approx 1.3$) than the scalar fluxes.

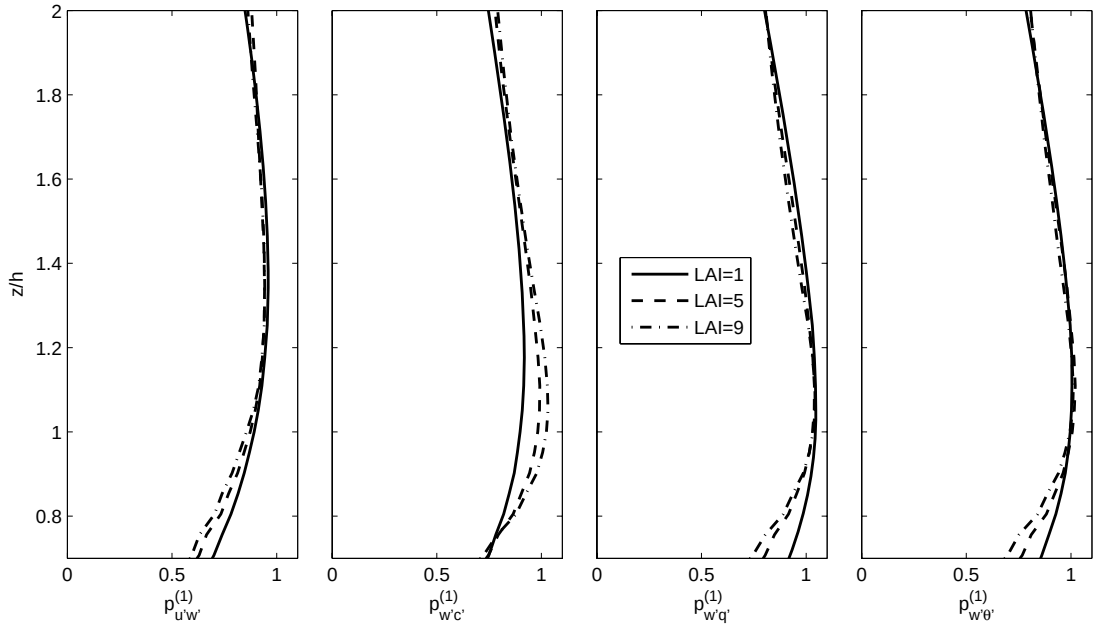

Figure 6.7. Vertical profiles of the fraction of the contribution of the coherent structure to the total flux of $u'w'$, $w'c'$, $w'q'$ and $w'\theta'$ (from left to right)

Given $p_{\beta_i\beta_j}$, it is convenient to calculate turbulent Schmidt numbers associated with the coherent structure $Sc_s^{(1)}$, by which we imply a situation where the bulk momentum and scalar transport is approximated by the contribution of the coherent structure while assuming identical mean fields of velocity and scalars. It follows that $Sc_s^{(1)}$ can be expressed by,

$$Sc_s^{(1)} = Sc_s\left(\frac{p_{u'w'}}{p_{w's'}}\right). \tag{6.17}$$

Figure 6.8 shows the results of $Sc_s^{(1)}$. $Sc_s^{(1)}$ is similar to Sc_s in the sense that: (1) $Sc_s^{(1)}$ generally increases with height and approaches 1; (2) $Sc_c^{(1)}$ tends to decrease with increasing LAI; (3) $Sc_q^{(1)}$ tends to increase with increasing LAI. The scatter plots

contrasting $Sc_s^{(1)}$ and Sc_s reveal that the deviation of $Sc_s^{(1)}$ from Sc_s is generally within the range of [-0.1, 0.1], suggesting the coherent structure has preserved the momentum-scalar transport dissimilarity from the original fields. Note that $Sc_s^{(1)}$ tends to underestimate Sc_s at low values and to overestimate Sc_s at high values with the critical point around 0.7 for all three scalar types and three LAI cases.

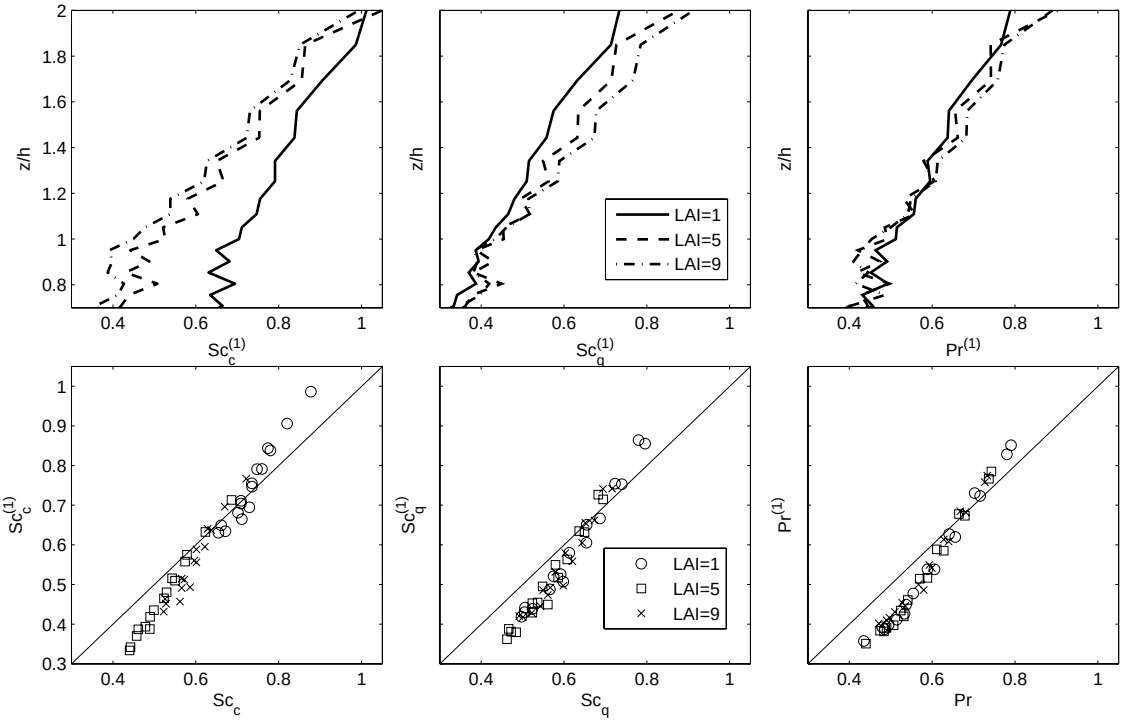

Figure 6.8. (Top row) Vertical profiles of turbulent Schmidt numbers associated with the coherent structures for c, q and θ (from left to right); (bottom row) scatter plots of turbulent Schmidt numbers associated with the coherent structure and from the original for c, q and θ (from left to right)

We explore the morphological features of the 3D coherent structure $\beta_i^{(1)}\left(r_x, r_y, z\right)$ and its effects on scalar dissimilarity first. The central cross-sections of the coherent structure (i.e. $r_x = 0$ and $r_y = 0$) are projected onto the *y*-*z* plane and the *x*-*z* plane,

respectively. The velocity vector plots are presented for LAI=5 where by the results for the cases of β_1 and β_2 are contrasted for the projection onto the *x*-*z* plane in Figure 6.9 and the projection onto the *y*-*z* plane in Figure 6.10, respectively. In the *x*-*z* plane, the coherent structure is characterized by a range of sweep motions centred around the canopy top and $r_x/h = 0$, and a spanwise vortex in the subcanopy region. In the *y*-*z* plane, the coherent structure is composed of sweeps framed by a pair of counter-rotating streamwise vortices. These results are consistent with previous descriptions of the coherent structures conducted in a wind-tunnel (Finnigan and Shaw 2000) and numerical (Huang et al. 2009b) experiments. The difference of the results of the coherent structure identified using β_1 and β_2 appears as that the coherent structure from β_1 is generally more compact (spatially). In conjunction with the results shown in Figure 6.6, this suggests that there is a strong interaction between the coherent structure and the scalar sources/sinks.

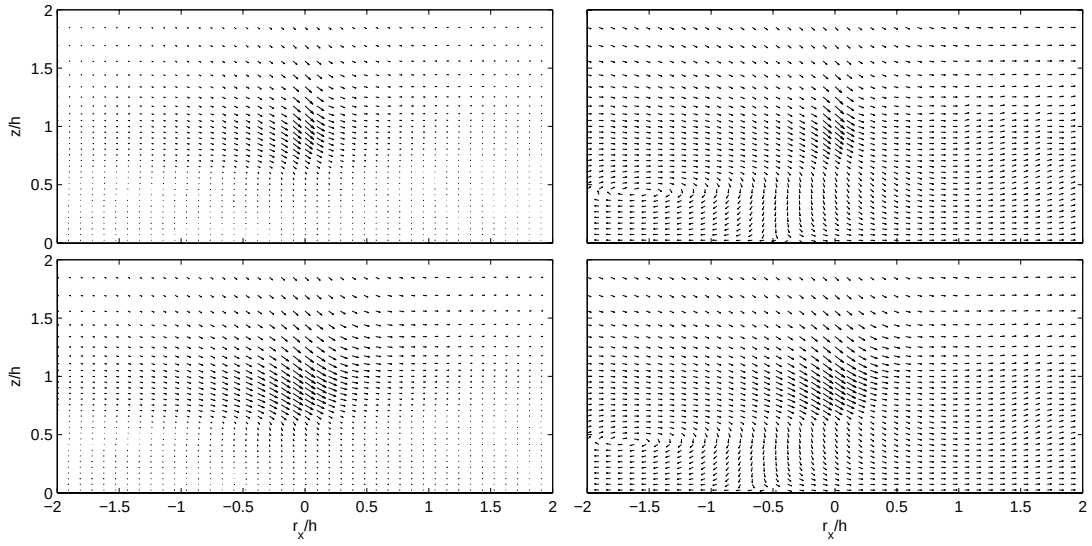

Figure 6.9. Quiver plots of the cross-section of the coherent structure on the *x*-*z* plane at $r_y = 0$ for LAI=5. The results of the top row are obtained from β_1 and the bottom row from β_2. In the panels on the right side, arrow lengths are ununiformly magnified from their corresponding left panels in order to reveal flow directions clearly

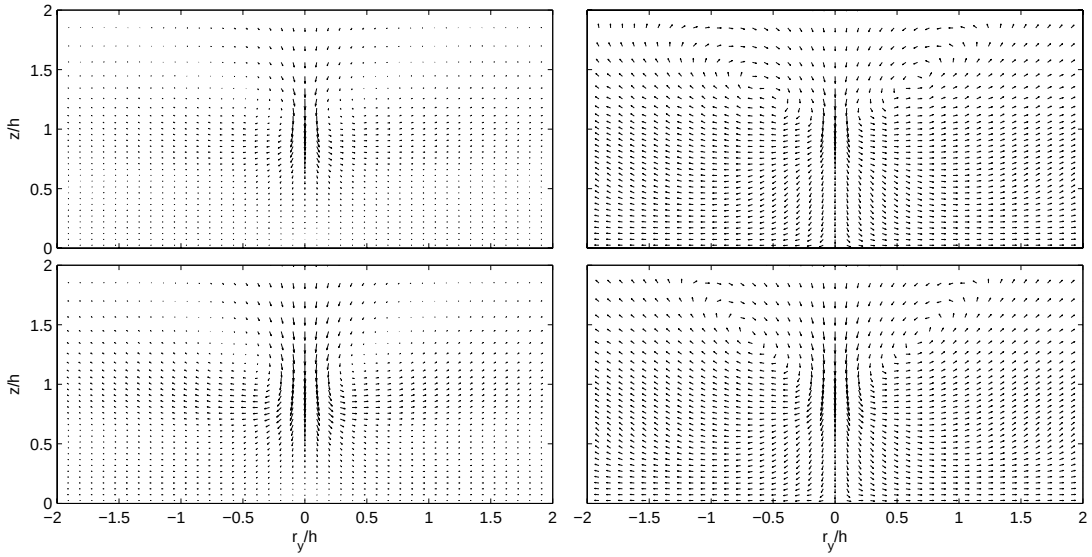

Figure 6.10. Quiver plots of the cross-section of the coherent structure on the *y*-*z* plane at $r_x = 0$ for LAI=5. The results of the top row are obtained from β_1 and the bottom row from β_2. In the panels on the right side, arrow lengths are not uniformly magnified from their corresponding left panels to reveal flow directions clearly

Figure 6.11 and Figure 6.12 show the comparison between momentum and scalar transport contributions of the coherent structure in the *x*-*z* plane at $r_y = 0$ and in the *y*-*z* plane at $r_x = 0$, respectively. Both similarity and dissimilarity between momentum and scalar transport emerge from this comparison. The similarity mainly appears as the core area of the coherent structure (represented by the two cross-sections). The most significant portion of the momentum as well as scalar transport by the coherent structures occurs within the vertical range $z/h \subset [0.6, 1.5]$, which is the central area where the primary stabilities generated by the interaction between the mean flow and the canopy structure arise. As sweep motions hit the canopy, they carry air relatively enriched in CO_2 and depleted in water vapour from above the canopy to this range. And, as ejection motions are generated from the canopy, they carry air relatively depleted in CO_2 and enriched in water vapour from inside the canopy to this range. The transport process is different for heat and momentum transfer because heat modifies the behavior of the flow through buoyancy and momentum is strongly influenced by the pressure field. . Moreover, the momentum and scalar transport carried by the coherent structures increase with increasing LAI. At LAI=1, the coherent structures do capture the major characteristics of the source-sink profiles of the scalars shown in Figure 6.2. The role of the soil surface is much more important in the CO_2 source-sink profile for LAI=1 than for LAI=5 and 9 and this source is captured by the large-scale coherent structures. For momentum transport, the aerodynamic roughness length of the soil

surface can be important only for LAI=1, which is also captured by the coherent structures. As LAI increases, the relative importance of the soil surface in acting as the source of carbon, water and sensible heat and the sink of momentum decreases, thereby increasing the similarity of scalar transport, as evidenced by the approximation of Sc_c, Sc_q and Pr at LAI=9 in Figure 6.4.

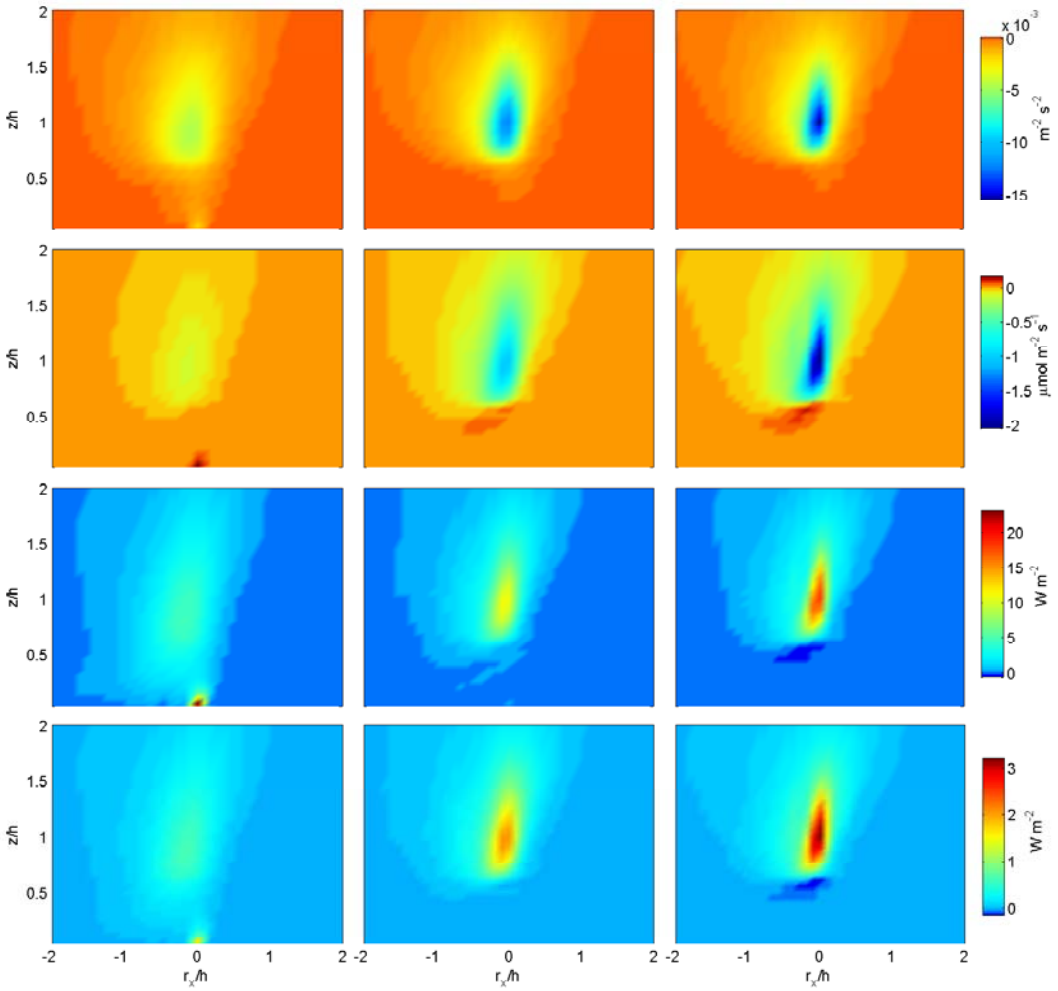

Figure 6.11. Colour plots of flux contribution of the coherent structures on the x-z plane at $r_y = 0$. Fluxes of momentum, c, q, θ from top to bottom, and LAI = 1, 5, 9 from left to right

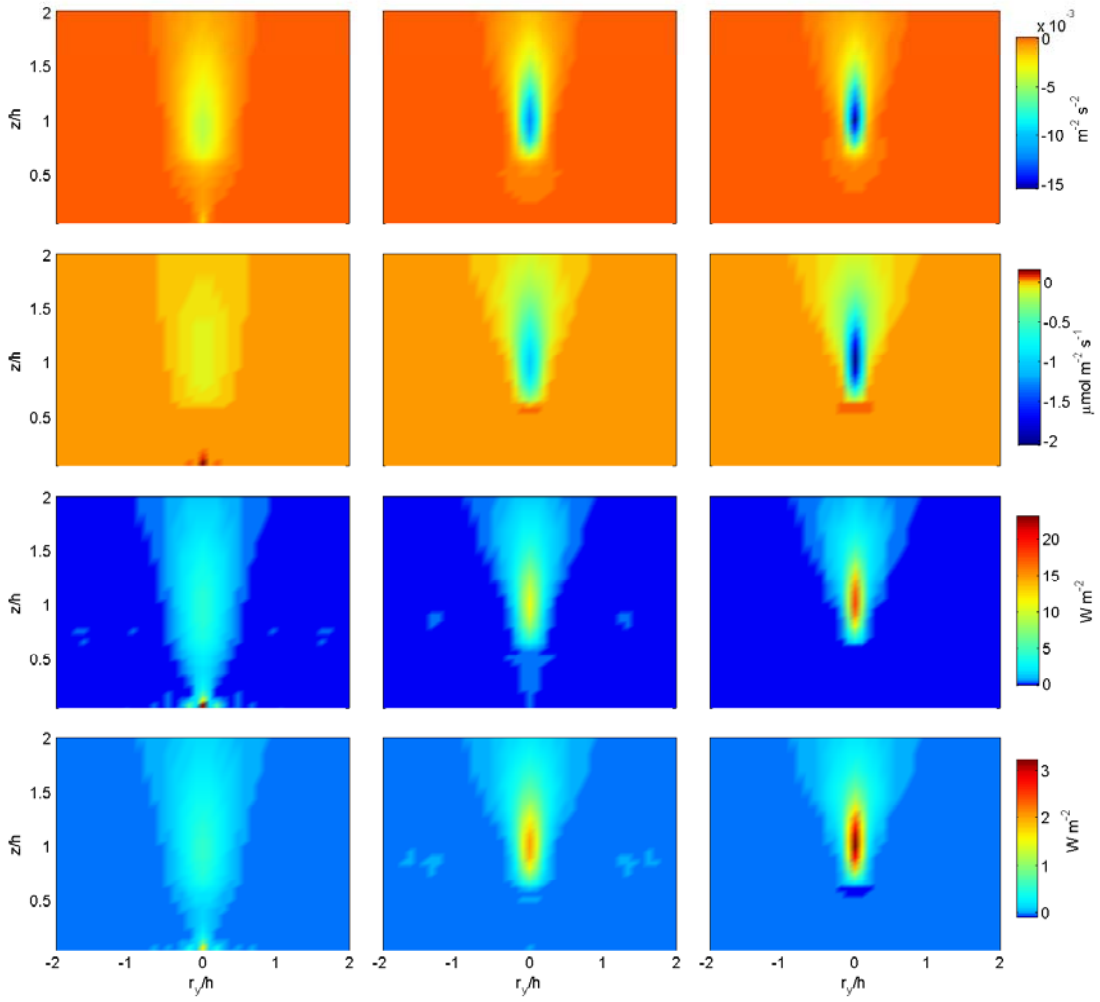

Figure 6.12. Colour plots of flux contribution of the coherent structures on the y-z plane at $r_x = 0$. Fluxes of momentum, c, q, θ from top to bottom, and LAI = 1, 5, 9 from left to right

Another contributor to the scalar transport similarity in dense canopies is the occurrence of the counter-gradient fluxes of carbon, water and sensible heat right below $z/h \approx 0.6$ (the height of the primary peak of the canopy structure profile), which can be explained by sweep motions carrying the air at the level with densest leaf areas which is strongly enriched in water vapour and heat but depleted in CO_2, to the level below as

they penetrate through the entire canopy. However, this counter-gradient flux does not exist for momentum because there is negligible momentum flux below $z/h \approx 0.6$ for LAI=5 and LAI=9 (see Figure 6.1) despite the presence of a mean velocity gradient. Finally, it is interesting to note that the scale of the coherent structure in x is about twice of that in y with the significant portion residing in $r_x/h \subset [-1.5, 0.5]$ and $r_y/h \subset [-0.5, 0.5]$.

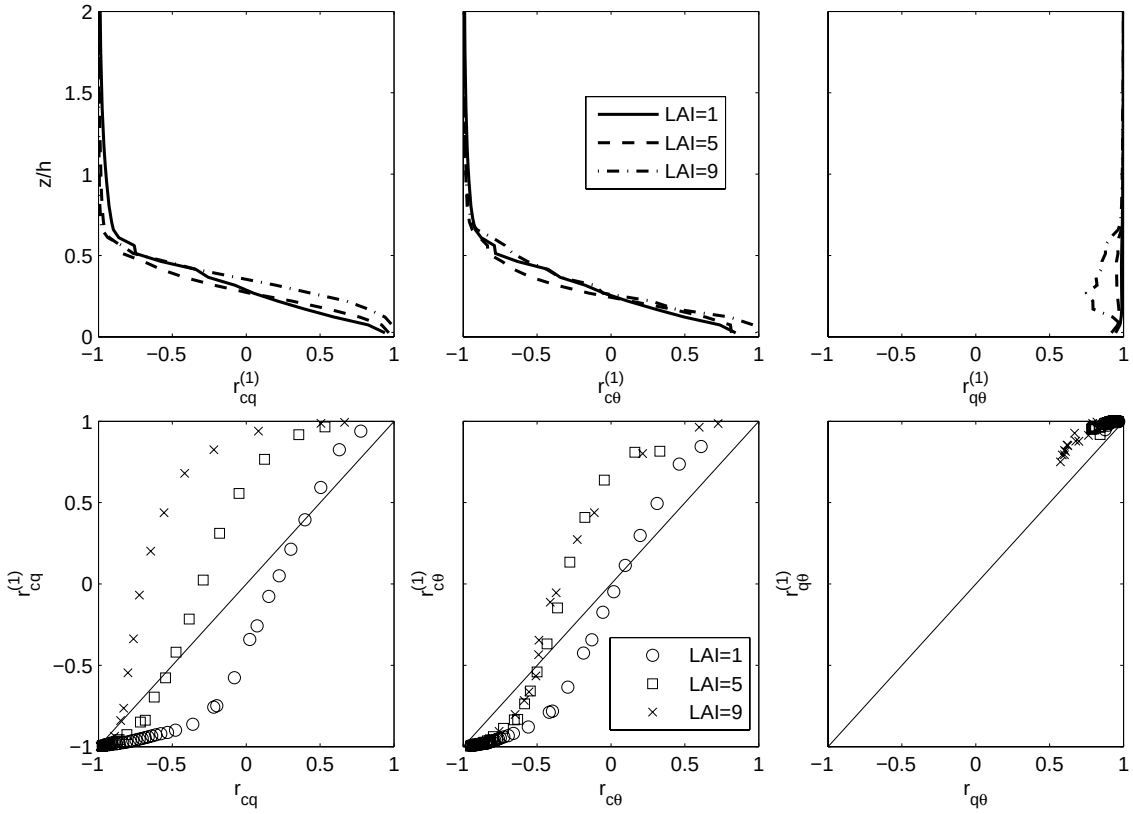

Figure 6.13. (Top row) Vertical profiles of correlation coefficients of the 3D coherent structure among three scalars: $r_{cq}^{(1)}$, $r_{c\theta}^{(1)}$ and $r_{q\theta}^{(1)}$ from left to right; (bottom row) scatter plots between the correlation coefficients of the coherent structures and the corresponding counterparts obtained from the original field: $r_{cq}^{(1)}$, $r_{c\theta}^{(1)}$ and $r_{q\theta}^{(1)}$ from left to right

In addition to revealing the signature of the source-sink dissimilarity in the coherent structure with respect to its geometric attributes, we also examine this signature quantitatively through the study of correlation coefficients. Figure 6.13 demonstrates the correlation coefficients between the scalar components of the coherent structures (represented by $r^{(1)}_{s_1 s_2}$) in contrast to $r_{s_1 s_2}$. It is shown that $r^{(1)}_{s_1 s_2}$ retains the basic pattern of $r_{s_1 s_2}$: $r^{(1)}_{cq}$ and $r^{(1)}_{c\theta}$ approach -1 in the upper part of canopy and above, approach 1 close the soil surface and cross zero in between; $r^{(1)}_{q\theta}$ is close to 1 in the entire CSL with slightly lower values in the sub-canopy region. However, unlike $r_{s_1 s_2}$, $r^{(1)}_{s_1 s_2}$ is relatively insensitive to LAI. This can be explained by the fact that in the three LAI cases, the coherent structures all arises from the same Kelvin-Helmholtz instability generated by the vertically inflected mean velocity profile (see Raupach et al. 1996), thereby transporting all the scalars in a similar way despite the influence of vegetation density on the source/sink strength of carbon, water and sensible heat. This explanation is supported by the conclusion in Huang et al. (2009b) that the mixing-layer analogy works well for canopy turbulence with LAI being around and greater than 1. The results of the correlation coefficients for the coherent structures identify the dissimilarity region defined in Section 4.2 roughly within the same range of $z/h \subset [0.1, 0.4]$ for $r^{(1)}_{cq}$ and $r^{(1)}_{c\theta}$. The sigmoidal shape of the $r_{s_1 s_2} - r^{(1)}_{s_1 s_2}$ plot suggests that the coherent structure tends to amplify the strength of correlation of the scalar quantities in the original field,

particularly when this correlation in the original field is already strong. This reinforces the inference in explaining Figure 6.7 that the incoherent components remaining in the original field after the extraction of the coherent structure are generally uncorrelated or weakly correlated, thus 'contaminating' the correlation in the original field and leading to $\left|r_{s_1 s_2}\right| < \left|r^{(1)}_{s_1 s_2}\right|$ for $\left|r_{s_1 s_2}\right| >> 0$.

In Figure 6.14, the result of ΔS_0 calculated for the truncated reconstruction $\beta_i^{(1)}(x, y, z, t)$ with only the coherent structure, denoted as $\Delta S_0^{(1)}$, are presented. A comparison between $\Delta S_0^{(1)}$ and ΔS_0 then quantifies the skill of the coherent structure in approximating the sweep-ejection cycle in the original field. It appears that the coherent structure retains the boundary layer effects (i.e. an ejection dominance) rather than the canopy effects (i.e. a sweep dominance) evidenced by positive $\Delta S_0^{(1)}$ in the region of examination. This finding may not be entirely surprising. After all, some of the key dynamical features of the coherent structures are influenced by σ_u^2, which is primarily produced well above the canopy. Moreover, ΔS_0 is a function of triple moments (see eq. (6.11)), which the POD identification strategy does not intend to preserve in coherent structures. Also, deep into the canopy, velocity variances sharply decrease such that the POD becomes insensitive to any significant flow characteristics including the relative importance between sweeps and ejections in this region. Moreover, the dependence on height is significantly weakened in $\Delta S_0^{(1)}$ when compared to that in ΔS_0, as evidenced

by the large deviations in the $\Delta S_0 - \Delta S_0^{(1)}$ scatter plot. We note that the addition of one more eigenmode superposed, the truncated reconstruction $\beta_i^{(2)}(x, y, z, t)$ can perform much better than $\beta_i^{(1)}(x, y, z, t)$ in approximating the sweep-ejection cycle in the original field. As shown in Figure 6.15, $\Delta S_0^{(2)}$ is able to capture both the boundary layer effects and the canopy effects and presents more dependence on height than does $\Delta S_0^{(1)}$. To furthermore reveal the effects of higher order modes on the sweep-ejection cycle, in Figure 6.16 we present the trend of $\Delta S_0^{(n)}$ approaching ΔS_0 with n = 1, 2, 5 and 10 respectively, using the case of LAI=5. While it is expected that the inclusion of more higher order modes will enhance the approximation of $\Delta S_0^{(n)}$ to ΔS_0, it is found that only five modes (with about 75 percent of total variances retained as indicated in Figure 6.6) are able to closely capture the values of ΔS_0 above the canopy and the sign and trend of ΔS_0 inside the canopy. For sweeps $\Delta S_0^{(n)}$ approaches ΔS_0 with a generally better performance for momentum than for the scalars due to the reason mentioned above regarding velocity variances.

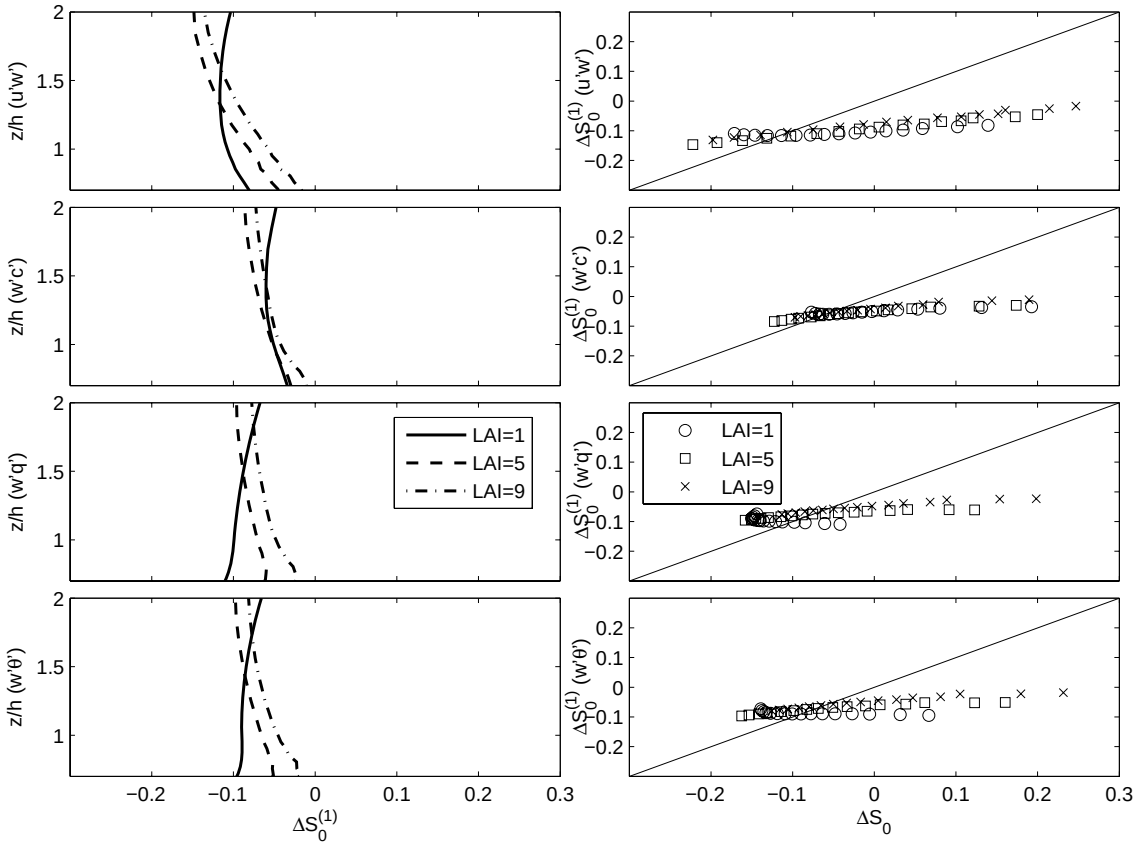

Figure 6.14. (Left column) $\Delta S_0^{(1)}$ for $u'w'$, $w'c'$, $w'q'$ and $w'\theta'$ (from top to bottom); (right column) scatter plots between ΔS_0 and $\Delta S_0^{(1)}$ for $u'w'$, $w'c'$, $w'q'$ and $w'\theta'$ (from top to bottom)

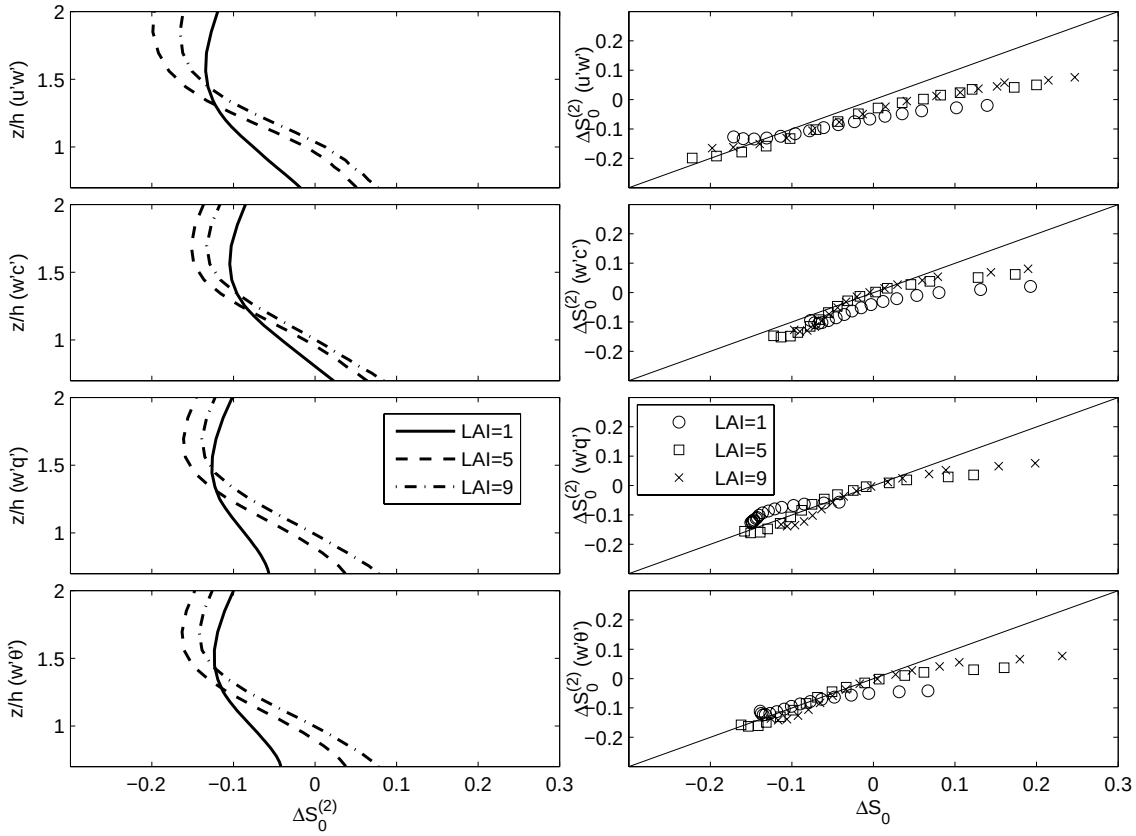

Figure 6.15. (Left column) $\Delta S_0^{(2)}$ for $u'w'$, $w'c'$, $w'q'$ and $w'\theta'$ (from top to bottom); (right column) scatter plots between ΔS_0 and $\Delta S_0^{(2)}$ for $u'w'$, $w'c'$, $w'q'$ and $w'\theta'$ (from top to bottom)

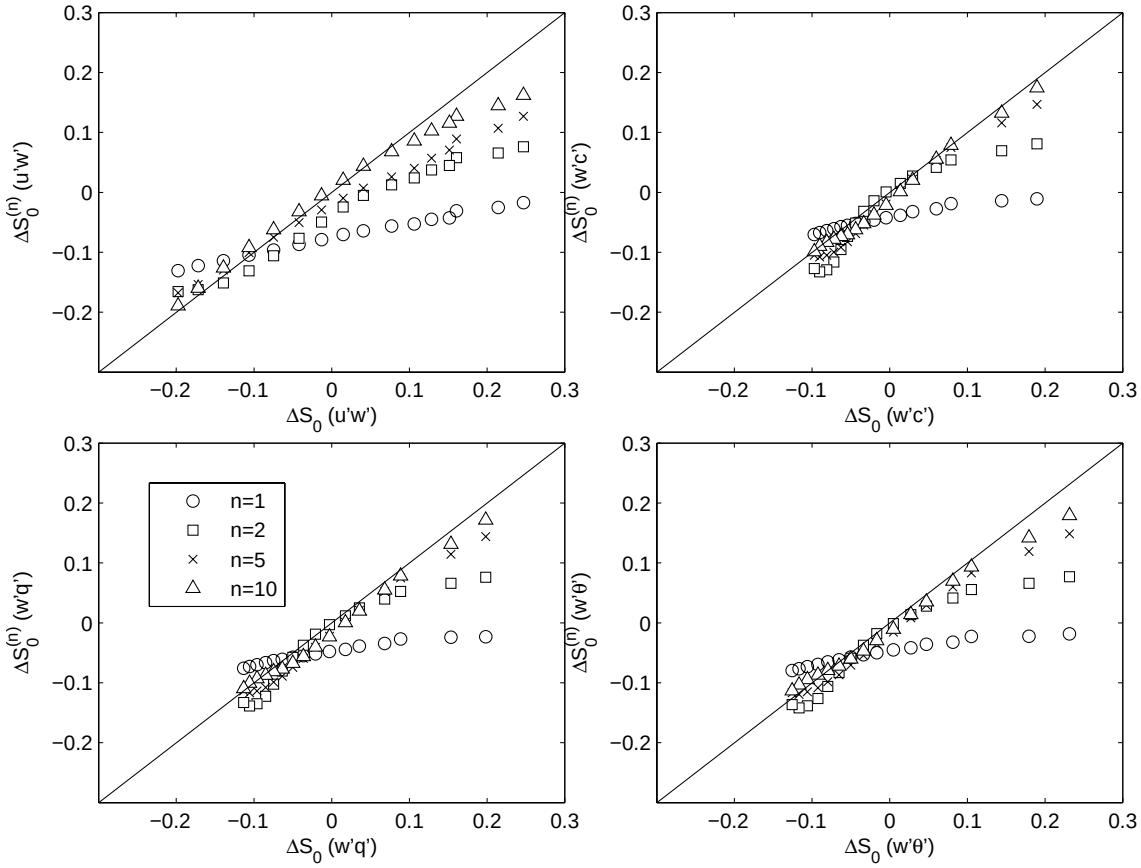

Figure 6.16. Scatter plots between ΔS_0 and $\Delta S_0^{(n)}$ (n = 1, 2, 5 and 10) for $u'w'$, $w'c'$, $w'q'$ and $w'\theta'$, respectively. Note that only resolved velocity and scalar quantities are used to produce this result

6.6 *Conclusions*

The dissimilarity of turbulent transport between two scalars within the canopy sublayer has mainly been attributed to differences in the distribution of scalar sources and sinks throughout the canopy. Since the large-scale coherent structures carry the information of the vertical distribution of the scalar sources and sinks, we hypothesize that their morphological features significantly affect the resulting scalar dissimilarity. This study tests this hypothesis by simulating the interaction between canopy, turbulent

transport and biophysical mechanisms over a forest of horizontally homogeneous foliage density where LAI ranged from sparse (=1) to dense (=9). The simulations were performed under prevailing environmental conditions of a single mid-day period with high sun angles and a prescribed saturation of soil moisture. The coherent structure is educed through the use of the proper orthogonal decomposition and the shot-effect expansion. Two approaches were used in the formulation of the POD: one based on velocity variances and another based on the joint velocity and scalar variances. The two approaches yielded similar results in terms of their geometric features of the velocity components. Based on the LES results and POD analysis, we found the following about the scalar-scalar dissimilarity and the role of the coherent structure:

1. A strong negative correlation between c and q from the top of the canopy sublayer down to a certain height (z/h~0.3) within the canopy exists and this correlation is enhanced as the canopy becomes denser since the CO_2 sink and the water vapour source become both stomatally regulated. Near the ground surface, c and q exhibit a positive correlation owing to that the ground surface emits CO_2 produced by litter and soil respiration and also water vapour through soil (and litter) evaporation. In the middle canopy, c and q are rather uncorrelated or weakly correlated. The CO_2 source from the ground appears to increase its turbulent Schmidt number when compared to the other scalars. On the contrary, the water vapour source and the sensible heat source tend to decrease their corresponding turbulent Schmidt number. In addition to the

impact on turbulent Schmidt number, the water vapour source and the heat source at the ground level also influence their corresponding sweep-ejection cycle by enhancing the relative importance of ejection.

2. The coherent structure is able to approximate turbulent Schmidt numbers obtained from the original fields. A basic agreement is also found in scalar-scalar correlation coefficients between the coherent structure and the original field with the coherent structure tending to magnify the magnitude of the scalar-scalar correlation when this correlation is strong. Finally, the ability of the coherent structure to describe the sweep-ejection cycle of the original field is also investigated. It was found that the coherent structure poorly represents the relative importance of sweep/ejection in the original field with the discrepancy mainly appearing as the lack of the sweep dominance inside the canopy. However, the superposition of higher order modes on the primary coherent structure (i.e. the leading mode) largely diminishes this discrepancy. Moreover, the convergence here is rather rapid with 5 modes recovering much of the ejection-sweep properties inside and above the canopy.

The broader impacts of this work are three fold: On the measurement side, there is now interest in partitioning eddy-covariance fluxes of CO_2 and water vapour into foliage versus forest floor using precisely the scalar dissimilarity (Thomas et al. 2008; Scanlon and Kustas 2010). We showed here that the success of such approaches depends on the spatial coherency of the organized structure. On the modelling side, we

showed that the similarity in Schmidt numbers among scalars, used virtually in all footprint models, may not be valid and does depend on how coupled the coherent structure is to the forest floor. Finally, from a theoretical perspective, this work illustrates the potential for using lower-dimensional models to link the vegetation to the atmosphere.

7 Conclusions

This chapter summarizes the dissertation and offers some suggestions for future study.

7.1 *Summary*

The importance of the coherent structures in turbulent flows has been well recognized for several decades. However, to reach the level of understanding about the coherent structures required for predictions of turbulent motions, the 3D geometrical attributes of the coherent structures as well as their relationship to the boundary conditions which are essential to their formation and growth have to be investigated first. This dissertation delivers such a study in the context of land-atmosphere interaction.

The proper orthogonal decomposition (POD) was adapted as the primary technique to extract the coherent structures mainly because the coherent structures identified by this technique are objective in the sense that they optimally capture the overall variances of the quantities under investigation (the turbulent kinetic energy in the case of turbulent velocities).

We have used large-eddy simulation (LES) as the major tool to reveal the dynamics and the cascading processes of turbulent flows between the land and the atmosphere. Since the LES models (rather than simulates) small-scale turbulent eddies, which do interact with the large-scale coherent structures to some degree, it is

reasonable to ask if and how well the LES is able to simulate the realistic large-scale coherent structures. This issue was addressed in this dissertation by comparing the coherent structures obtained from LES of the atmospheric boundary-layer (ABL) to those from direct numerical simulation (DNS) of channel flow.

With the ability of the LES in producing the coherent structures validated, we then study how the landscape features affect the coherent structures with a focus on the shapes and their importance in describing turbulent exchange of energy, momentum and mass between the land and the atmosphere. The landscape features studied here include horizontally homogeneous vegetation cover with the density ranging from extremely sparse (LAI=0.0625) to extremely dense (LAI=16), and a forest-clearing-forest transition which is periodic in the streamwise direction with various ratios of the length between the forest part and the clearing part.

Finally, we have quantitatively investigated the role of the coherent structures in scalar transport in the canopy sublayer with the emphasis particularly placed on the issue of scalar dissimilarity and momentum-scalar transport dissimilarity.

7.2 *Suggestions for Future Work*

A possible continuation of this work is to develop low-dimensional models of turbulent dynamics in land-atmosphere interaction through the approach of the coherent structures. In fact, together with the Galerkin projection technique, the POD is able to convert the Navier-Stokes equations to a set of ordinary differential equations

(ODEs) with the complexity of the ODEs being dependent on the eigenmodes retained. Thus, it is interesting to study the balance between the modes being retained and the features of some important dynamical phenomena (e.g. the sweep-ejection cycle) being reproduced by the ODEs. Another direction for future studies is to apply the current knowledge we possess about the relationship between the morphological features of the coherent structures and landscape features to develop transport models in the roughness sublayer with better performance.

References

Albertson JD (1996) Large-eddy simulation of land-atmosphere interaction. Ph.D. Thesis, University of California Davis, 185 pp.

Albertson JD, Katul GG and Wiberg P (2001) Relative importance of local and regional controls on coupled water, carbon, and energy fluxes. Adv Water Resour. 24:1103-1118.

Albertson JD and Parlange MB (1999a) Natural integration of scalar fluxes from complex terrain. Adv Water Resour. 23:239-252.

Albertson JD and Parlange MB (1999b) Surface length scales and shear stress: Implications for land-atmosphere interaction over complex terrain. Water Resour Res. 35:2121-2132.

Albertson JD, Parlange MB, Katul GG, Chu CR and Stricker H (1995) Sensible Heat-Flux from Arid Regions - a Simple Flux-Variance Method. Water Resour Res. 31:969-973.

Antonia RA (1981) Conditional sampling in turbulence measurement. Annu Rev Fluid Mech. 13:131-156.

Asner GP, Jonathan MO and Hicke JA (2003) Global synthesis of leaf area index observations: implications for ecological and remote sensing studies. Global Ecol Biogeogr. 12:191-205.

Aubry N, Holmes P, Lumley JL and Stone E (1988) The dynamics of coherent structures in the wall region of a turbulent boundary layer. J Fluid Mech. 192:115-173.

Bakewell HP and Lumley JL (1967) Viscous sublayer and adjacent wall region in turbulent pipe flow. Phys Fluids. 10:1880-1889.

Bergstrom H and Hogstrom U (1989) Turbulent exchange above a pine forest II. Organized structures. Boundary-Layer Meteorol. 49:231-263.

Berkooz G, Holmes P and Lumley JL (1993) The proper orthogonal decomposition in the analysis of turbulent flows. Annu Rev Fluid Mech. 25:539-575.

Bou-Zeid E, Parlange MB and Meneveau C (2007) On the parameterization of surface roughness at regional scales. J Atmos Sci. 64:216-227.

Brown RA (1980) Longitudinal Instabilities and Secondary Flows in the Planetary Boundary-Layer - a Review. Reviews of Geophysics. 18:683-697.

Brunet Y, Finnigan JJ and Raupach MR (1994) A wind tunnel study of air flow in waving wheat: single-point velocity statistics. Boundary-Layer Meteorol. 70:95-132.

Campbell GS and Norman JM (1998) An introduction to environmental biophysics. Springer, New York, 286 pp.

Cassiani M, Franzese P and Giostra U (2005) A PDF micromixing model of dispersion for atmospheric flow. Part 1: development of the model, application to homogeneous turbulence and to neutral boundary layer. Atmos Environ. 39:1457-1469.

Cassiani M, Katul GG and Albertson JD (2008) The effects of canopy leaf area index on airflow across forest edges: Large-eddy simulation and analytical results. Boundary-Layer Meteorol. 126:433-460.

Cassiani M, Radicchi A and Albertson JD (2007) Modelling of concentration fluctuations in canopy turbulence. Boundary-Layer Meteorol. 122:655-681.

Cava D, Katul GG, Scrimieri A, Poggi D, Cescatti A and Giostra U (2006) Buoyancy and the sensible heat flux budget within dense canopies. Boundary-Layer Meteorol. 118:217-240.

Cava D, Katul GG, Sempreviva AM, Giostra U and Scrimieri A (2008) On the anomalous behaviour of scalar flux-variance similarity functions within the canopy sub-layer of a dense alpine forest. Boundary-Layer Meteorol. 128:33-57.

Chu CR, Parlange MB, Katul GG and Albertson JD (1996) Probability density functions of turbulent velocity and temperature in the atmospheric surface layer. Water Resour Res. 32:1681-1688.

Corrsin S (1943) Investigation of flow in an axially symmetric heated jet of air. NACA Adv Conf Rep. 3123.

Davidson PA (2004) Turbulence : An introduction for scientists and engineers. Oxford University Press, New York, 657 pp.

De Bruin HAR (1989) Physical aspects of the planetary boundary layer with special reference to regional evapotranspiration. In: Black TA, Spittlehouse, D.L., Novak,

M.D., and Price, D.T. (ed). Estimation of areal evapotranspiration, Vancouver, BC, Canada1989, vol 177/ IAHS Publication, City, pp. 117-132.

De Bruin HAR, Van Den Hurk BJJM and Kroon LJM (1999) On the temperature-humidity correlation and similarity. Boundary-Layer Meteorol. 93:453-468.

Deardorf JW (1970) A numerical study of three-dimensional turbulent channel flow at large Reynolds numbers. J Fluid Mech. 41:453-465.

Delville J, Ukeiley L, Cordier L, Bonnet JP and Glauser M (1999) Examination of large-scale structures in a turbulent plane mixing layer. Part 1. Proper orthogonal decomposition. J Fluid Mech. 391:91-122.

Dupont S and Brunet Y (2008a) Edge flow and canopy structure: A large-eddy simulation study. Boundary-Layer Meteorol. 126:51-71.

Dupont S and Brunet Y (2008b) Influence of foliar density profile on canopy flow: A large-eddy simulation study. Agric For Meteorol. 148:976-990.

Ellsworth DS, Oren R, Huang C, Phillips N and Hendrey GR (1995) Leaf and canopy responses to elevated CO2 in a pine forest under free air CO2 enrichment. Oecologia. 104:139-146.

Etling D and Brown RA (1993) Roll vortices in the planetary boundary layer: A review. Boundary-Layer Meteorol. 65:215-248.

Finnigan JJ (1979a) Turbulence in waving wheat. I. Mean statistics and honami. Boundary-Layer Meteorol. 16:181-211.

Finnigan JJ (1979b) Turbulence in waving wheat. II. Structure of momentum transfer. Boundary-Layer Meteorol. 16:213-236.

Finnigan JJ (2000) Turbulence in plant canopies. Annu Rev Fluid Mech. 32:519-571.

Finnigan JJ and Belcher SE (2004) Flow over a hill covered with a plant canopy. Q J Roy Meteor Soc. 130:1-29.

Finnigan JJ and Shaw RH (2000) A wind-tunnel study of airflow in waving wheat: An EOF analysis of the structure of the large-eddy motion. Boundary-Layer Meteorol. 96:211-255.

Flesch TK, Prueger JH and Hatfield JL (2002) Turbulent Schmidt number from a tracer experiment. Agric For Meteorol. 111:299-307.

Gao W, Shaw RH and Paw KT (1989) Observation of organized structure in turbulent flow within and above a forest canopy. Boundary-Layer Meteorol. 47:349-377.

Gardiner BA (1994) Wind and Wind Forces in a Plantation Spruce Forest. Boundary-Layer Meteorol. 67:161-186.

Garratt JR (1992) The atmospheric boundary layer. Cambridge University Press, Cambridge, 316 pp.

Guo XF, Zhang HS, Cai XH, Kang L, Zhu T and Leclerc MY (2009) Flux-Variance Method for Latent Heat and Carbon Dioxide Fluxes in Unstable Conditions. Boundary-Layer Meteorol. 131:363-384.

Harman IN and Finnigan JJ (2008) Scalar concentration profiles in the canopy and roughness sublayer. Boundary-Layer Meteorol. 129:323-351.

Head MR and Bandyopadhyay P (1981) New aspects of turbulent boundary layer structure. J Fluid Mech. 107:297-338.

Herzog S (1986) The large scale structure in the near-wall region of turbulent pipe flow. Ph.D. Thesis, Cornell University, 161 pp.

Holmes P, Lumley JL and Berkooz G (1996) Turbulence, coherent structures, dynamical systems, and symmetry. Cambridge University Press, New York, 420 pp.

Horst TW and Weil JC (1992) Footprint estimation for scalar flux measurements in the atmospheric surface layer. Boundary-Layer Meteorol. 59:279-296.

Hsieh CI and Katul G (2009) The Lagrangian stochastic model for estimating footprint and water vapor fluxes over inhomogeneous surfaces. Int J Biometeorol. 53:87-100.

Hsieh CI, Katul GG, Schieldge J, Sigmon J and Knoerr KR (1996) Estimation of momentum and heat fluxes using dissipation and flux-variance methods in the unstable surface layer. Water Resour Res. 32:2453-2462.

Hsieh CI, Lai MC, Hsia YJ and Chang TJ (2008) Estimation of sensible heat, water vapor, and CO2 fluxes using the flux-variance method. Int J Biometeorol. 52:521-533.

Huang J, Cassiani M and Albertson JD (2009a) Analysis of coherent structures within the atmospheric boundary layer. Boundary-Layer Meteorol. 131:147-171.

Huang J, Cassiani M and Albertson JD (2009b) The effects of vegetation density on coherent turbulent structures within the canopy sublayer: a large-eddy simulation study. Boundary-Layer Meteorol. 133:253-275.

Huang J, Cassiani M and Albertson JD (2010) Coherent turbulent structures across a vegetation discontinuity. Boundary-Layer Meteorol. In review.

Irvine MR, Gardiner BA and Hill MK (1997) The evolution of turbulence across a forest edge. Boundary-Layer Meteorol. 84:467-496.

Jochum MAO, de Bruin HAR, Holtslag AAM and Belmonte AC (2006) Area-averaged surface fluxes in a semiarid region with partly irrigated land: Lessons learned from EFEDA. J Appl Meteorol Clim. 45:856-874.

Katul G, Goltz SM, Hsieh CI, Cheng Y, Mowry F and Sigmon J (1995) Estimation of surface heat and momentum fluxes using the flux variance method above uniform and nonuniform terrain. Boundary-Layer Meteorol. 74:237-260.

Katul G, Hsieh CI, Kuhn G, Ellsworth D and Nie DL (1997a) Turbulent eddy motion at the forest-atmosphere interface. J Geophys Res. 102:13409-13421.

Katul G, Hsieh CI, Oren R, Ellsworth D and Phillips N (1996a) Latent and sensible heat flux predictions from a uniform pine forest using surface renewal and flux variance methods. Boundary-Layer Meteorol. 80:249-282.

Katul G, Kuhn G, Schieldge J and Hsieh CI (1997b) The ejection-sweep character of scalar fluxes in the unstable surface layer. Boundary-Layer Meteorol. 83:1-26.

Katul G, Oren R, Ellsworth D, Hsieh CI, Phillips N and Lewin K (1997c) A Lagrangian dispersion model for predicting CO2 sources, sinks, and fluxes in a uniform loblolly pine (Pinus taeda L) stand. J Geophys Res-Atmos. 102:9309-9321.

Katul G, Poggi D, Cava D and Finnigan J (2006a) The relative importance of ejections and sweeps to momentum transfer in the atmospheric boundary layer. Boundary-Layer Meteorol. 120:367-375.

Katul GG and Albertson JD (1998) An investigation of higher-order closure models for a forested canopy. Boundary-Layer Meteorol. 89:47-74.

Katul GG, Albertson JD, Hsieh CI, Conklin PS, Sigmon JT, Parlange MB and Knoerr KR (1996b) The ''inactive'' eddy motion and the large-scale turbulent pressure fluctuations in the dynamic sublayer. J Atmos Sci. 53:2512-2524.

Katul GG, Cava D, Launiainen S and Vesala T (2009) An analytical model for the two-scalar covariance budget inside a uniform dense canopy. Boundary-Layer Meteorol. 131:173-192.

Katul GG and Chang WH (1999) Principal length scales in second-order closure models for canopy turbulence. J Appl Meteorol. 38:1631-1643.

Katul GG, Finnigan JJ, Poggi D, Leuning R and Belcher SE (2006b) The influence of hilly terrain on canopy-atmosphere carbon dioxide exchange. Boundary-Layer Meteorol. 118:189-216.

Katul GG, Geron CD, Hsieh CI, Vidakovic B and Guenther AB (1998) Active turbulence and scalar transport near the forest-atmosphere interface. J Appl Meteorol. 37:1533-1546.

Katul GG, Sempreviva AM and Cava D (2008) The temperature-humidity covariance in the marine surface layer: A one-dimensional analytical model. Boundary-Layer Meteorol. 126:263-278.

Khanna S and Brasseur JG (1997) Analysis of Monin-Obukhov similarity from large-eddy simulation. J Fluid Mech. 345:251-286.

Kim J, Moin P and Moser R (1987) Turbulence statistics in fully developed channel flow at low Reynolds number. J Fluid Mech. 177:133-166.

Kline SJ, Reynolds WC, Schraub FA and Runstadl PW (1967) The structure of turbulent boundary layers. J Fluid Mech. 30:741-773.

Koeltzsch K (2000) The height dependence of the turbulent Schmidt number within the boundary layer. Atmos Environ. 34:1147-1151.

Kosovic B (1997) Subgrid-scale modelling for the large-eddy simulation of high-Reynolds-number boundary layers. J Fluid Mech. 336:151-182.

Lamaud E and Irvine M (2006) Temperature-humidity dissimilarity and heat-to-water-vapour transport efficiency above and within a pine forest canopy: The role of the Bowen ratio. Boundary-Layer Meteorol. 120:87-109.

Lappen CL and Randall DA (2001a) Toward a unified parameterization of the boundary layer and moist convection. Part I: A new type of mass-flux model. J Atmos Sci. 58:2021-2036.

Lappen CL and Randall DA (2001b) Toward a unified parameterization of the boundary layer and moist convection. Part II: Lateral mass exchanges and subplume-scale fluxes. J Atmos Sci. 58:2037-2051.

Lappen CL and Randall DA (2001c) Toward a unified parameterization of the boundary layer and moist convection. Part III: Simulations of clear and cloudy convection. J Atmos Sci. 58:2052-2072.

Lappen CL and Randall DA (2005) Using idealized coherent structures to parameterize momentum fluxes in a PBL mass-flux model. J Atmos Sci. 62:2829-2846.

Laurance WF (2004) Forest-climate interactions in fragmented tropical landscapes. Phil Trans Roy Soc London. 359:345-352.

Leclerc MY and Thurtell GW (1990) Footprint Prediction of Scalar Fluxes Using a Markovian Analysis. Boundary-Layer Meteorol. 52:247-258.

Lin CL, McWilliams JC, Moeng CH and Sullivan PP (1996) Coherent structures and dynamics in a neutrally stratified planetary boundary layer flow. Phys Fluids. 8:2626-2639.

Lu SS and Willmart WW (1973) Measurements of structure of Reynolds stress in a turbulent boundary layer. J Fluid Mech. 60:481-511.

Lumley JL (1967) The structure of inhomogeneous turbulent flows. In: Yagolm AM and Tatarsky VI (eds). Atmospheric Turbulence and Radio Wave Propagation, Moscow1967, / Nauka, City, pp. 166-178.

Lumley JL (1970) Stochastic tools in turbulence. Academic Press, New York, 194 pp.

Lumley JL (1981) Coherent structures in turbulence. In: Meyer RE (ed.), Transition and Turbulence. Academic, New York.

Mason PJ and Thomson DJ (1992) Stochastic backscatter in large-eddy simulations of boundary layers. J Fluid Mech. 242:51-78.

Massman WJ and Weil JC (1999) An analytical one-dimensional second-order closure model of turbulence statistics and the Lagrangian time scale within and above plant canopies of arbitrary structure. Boundary-Layer Meteorol. 91:81-107.

Meijninger WML, Beyrich F, Luedi A, Kohsiek W and De Bruin HAR (2006) Scintillometer-based turbulent fluxes of sensible and latent heat over a

heterogeneous land surface - A contribution to LITFASS-2003. Boundary-Layer Meteorol. 121:89-110.

Michels BI and Jochum AM (1995) Heat and moisture flux profiles in a region with inhomogeneous surface evaporation. J Hydrol. 166:383-407.

Moeng CH (1984) A large-eddy simulation model for the study of planetary boundary layer turbulence. J Atmos Sci. 41:2052-2062.

Moeng CH, Dudhia J, Klemp J and Sullivan P (2007) Examining two-way grid nesting for large eddy simulation of the PBL using the WRF model. Mon Weather Rev. 135:2295-2311.

Moin P and Moser RD (1989) Characteristic-eddy decomposition of turbulence in a channel. J Fluid Mech. 200:471-509.

Novak MD, Warland JS, Orchansky AL, Ketler R and Green S (2000) Wind tunnel and field measurements of turbulent flow in forests. Part I: Uniformly thinned stands. Boundary-Layer Meteorol. 95:457-495.

Oke TR (1987) Boundary layer climates. Methuen, London, 435 pp.

Ookouchi Y, Segal M, Kessler RC and Pielke RA (1984) Evaluation of soil moisture effects on the generation and modification of mesoscale circulations. Mon Weather Rev. 112:2281-2292.

Piomelli U and Balaras E (2002) Wall-layer models for large-eddy simulations. Annu Rev Fluid Mech. 34:349-374.

Poggi D, Katul G and Albertson J (2006) Scalar dispersion within a model canopy: Measurements and three-dimensional Lagrangian models. Adv Water Resour. 29:326-335.

Poggi D, Katul GG and Albertson JD (2004a) Momentum transfer and turbulent kinetic energy budgets within a dense model canopy. Boundary-Layer Meteorol. 111:589-614.

Poggi D, Porporato A, Ridolfi L, Albertson JD and Katul GG (2004b) The effect of vegetation density on canopy sub-layer turbulence. Boundary-Layer Meteorol. 111:565-587.

Porte-Agel F, Meneveau C and Parlange MB (2000) A scale-dependent dynamic model for large-eddy simulation: application to a neutral atmospheric boundary layer. J Fluid Mech. 415:261-284.

Raupach MR (1981) Conditional statistics of Reynolds stress in rough-wall and smooth-wall turbulent boundary layers. J Fluid Mech. 108:363-382.

Raupach MR (1988) Canopy transport processes. In: Steffen WL and Denmead OT (eds.), Flow and transport in the natural environment. Springer-Verlag, New York.

Raupach MR (1989a) Applying lagrangian fluid mechanics to infer scalar source distributions from concentration profiles in plant canopies. Agr Forest Meteorol. 47:85-108.

Raupach MR (1989b) A practical lagrangian method for relating scalar concentrations to source distributions in vegetation canopies. Q J Roy Meteor Soc. 115:609-632.

Raupach MR, Finnigan JJ and Brunet Y (1989) Coherent eddies in vegetation canopies. Proc. Fourth Australasian Conf. on Heat and Mass Transfer, Christchurch, New Zealand, 9-12 May 1989, City.

Raupach MR, Finnigan JJ and Brunet Y (1996) Coherent eddies and turbulence in vegetation canopies: The mixing-layer analogy. Boundary-Layer Meteorol. 78:351-382.

Raupach MR and Thom AS (1981) Turbulence in and above plant canopies. Annu Rev Fluid Mech. 13:97-129.

Robinson SK (1991) Coherent motions in the turbulent boundary layer. Annu Rev Fluid Mech. 23:601-639.

Rogers MM and Moser RD (1994) Direct simulation of a self-similar turbulent mixing layer. Phys Fluids. 6:903-923.

Sadani LK and Kulkarni JR (2001) A study of coherent structures in the atmospheric surface layer over short and tall grass. Boundary-Layer Meteorol. 99:317-334.

Sagaut P, Deck S and Terracol M (2006) Multiscale and multiresolution approaches in turbulence. Imperial College Press, London, 340 pp.

Scanlon TM and Albertson JD (2001) Turbulent transport of carbon dioxide and water vapor within a vegetation canopy during unstable conditions: Identification of episodes using wavelet analysis. J Geophys Res. 106:7251-7262.

Scanlon TM and Kustas WP (2010) Partitioning carbon dioxide and water vapor fluxes using correlation analysis. Agric For Meteorol. 150:89-99.

Scanlon TM and Sahu P (2008) On the correlation structure of water vapor and carbon dioxide in the atmospheric surface layer: A basis for flux partitioning. Water Resour Res. 44:W10418.

Shaw RH, Brunet Y, Finnigan JJ and Raupach MR (1995) A wind tunnel study of air flow in waving wheat: two-point velocity statistics. Boundary-Layer Meteorol. 76:349-376.

Shaw RH, Tavangar J and Ward DP (1983) Structure of the Reynolds stress in a canopy layer. J Clim Appl Meteorol. 22:1922-1931.

Sirovich L (1987a) Turbulence and the dynamics of coherent structures, Part 1: Coherent Structures. Q Appl Math. 45:561-571.

Sirovich L (1987b) Turbulence and the dynamics of coherent structures, Part 2: Symmetries and transformations. Q Appl Math. 45:573-582.

Sirovich L (1987c) Turbulence and the dynamics of coherent structures, Part 3: Dynamics and scaling. Q Appl Math. 45:583-590.

Smith TR, Moehlis J and Holmes P (2005) Low-dimensional modelling of turbulence using the proper orthogonal decomposition: A tutorial. Nonlinear Dynamics. 41:275-307.

Stoll R and Porte-Agel F (2006) Effect of roughness on surface boundary conditions for large-eddy simulation. Boundary-Layer Meteorol. 118:169-187.

Stull RB (1988) An introduction to boundary layer meteorology. Kluwer Academic Publishers, Dordrecht/Boston/London, 666 pp.

Sullivan PP, McWilliams JC and Moeng CH (1996) A grid nesting method for large-eddy simulation of planetary boundary-layer flows. Boundary-Layer Meteorol. 80:167-202.

Thomas C and Foken T (2007) Flux contribution of coherent structures and its implications for the exchange of energy and matter in a tall spruce canopy. Boundary-Layer Meteorol. 123:317-337.

Thomas C, Martin JG, Goeckede M, Siqueira MB, Foken T, Law BE, Loescher HW and Katul G (2008) Estimating daytime subcanopy respiration from conditional sampling methods applied to mufti-scalar high frequency turbulence time series. Agric For Meteorol. 148:1210-1229.

Townsend AA (1956) The structure of turbulent shear flow. Cambridge Univ Press, 315 pp.

Vesala T, Kljun N, Rannik U, Rinne J, Sogachev A, Markkanen T, Sabelfeld K, Foken T and Leclerc MY (2008) Flux and concentration footprint modelling: State of the art. Environmental Pollution. 152:653-666.

Wallace JM, Brodkey RS and Eckelman.H (1972) Wall region in turbulent shear flow. J Fluid Mech. 54:39-48.

Walter BA and Overland JE (1984) Observations of Longitudinal Rolls in a near Neutral Atmosphere. Mont Wea Rev. 112:200-208.

Williams CA, Scanlon TM and Albertson JD (2007) Influence of surface heterogeneity on scalar dissimilarity in the roughness sublayer. Boundary-Layer Meteorol. 122:149-165.

Willmart WW and Lu SS (1972) Structure of the Reynolds stress near the wall. J Fluid Mech. 55:65-92.

Wilson DK (1996) Empirical orthogonal function analysis of the weakly convective atmospheric boundary layer. Part I: Eddy structures. J Atmos Sci. 53:801-823.

Wilson JD (1989) Turbulent transport within the plant canopy. Estimation of Areal Evapotranspiration, Intl Assoc Hydrol Sci Public1989, vol 177, City, pp. 43-80.

Wilson NR and Shaw RH (1977) Higher-order closure model for canopy flow. J Appl Meteorol. 16:1197-1205.

Yang B, Raupach MR, Shaw RH, Tha K, Paw U and Morse AP (2006) Large-eddy simulation of turbulent flow across a forest edge. Part I: Flow statistics. Boundary-Layer Meteorol. 120:377-412.

Biography

Jing Huang attended USTC (University of Science and Technology of China) and graduated in 2001 with a B.E. in Mechanical Engineering and a dual B.S. in Computer Science. Upon finishing his undergraduate studies, he worked as a software engineer and research assistant at Institute of Computing Technology of Chinese Academy of Sciences for three years. Jing began his Ph.D. study with Professor John Albertson in the Department of Civil and Environmental Engineering at Duke University in the Spring of 2005.